

Institut für Kern- und Teilchenphysik
Fakultät Mathematik und Naturwissenschaften
Technische Universität Dresden

Simulations of Dielectron Detection Capabilities of HADES at SIS100

Diplomarbeit
zur Erlangung des akademischen Grades
Diplom-Physiker

vorgelegt von
Benjamin Banner
geboren am 06. Dezember 1980 in Schwerin

Dresden 2007

Eingereicht am 5. September 2006

1. Gutachter: Prof. Dr. E. Grosse
2. Gutachter: Prof. Dr. B. Kämpfer

Zusammenfassung

Die für das FAIR-Projekt an der GSI Darmstadt geplante neue Beschleunigeranlage SIS100/300 wird Schwerionenstrahlen mit Strahlenergien zwischen 8 AGeV und 25 AGeV und mehr verfügbar machen. Diese Arbeit untersucht, inwiefern in Kohlenstoff–Kohlenstoff-Kollisionen bei diesen Energien mit dem HADES-Detektor, der erfolgreich in Experimenten am SIS18 mit elementare Sonden und schweren Ionen eingesetzt wurde, Dielektronen gemessen werden können. Dazu wurde ein auf dem relativistischen Transportmodell UrQMDv1.3p1 basierender Ereignisgenerator implementiert. Vorhersagen des UrQMD-Modells werden geprüft und verfügbaren experimentelle Ergebnissen gegenübergestellt. Unsere Ergebnisse für Dielektronen werden mit auf m_t -Scaling und Transportmodellen basierenden Simulation verglichen. Es zeigt sich, dass Photon-Konversion $\gamma \rightarrow e^+e^-$ in der $\rho - \omega$ -Massenregion ein wichtige Quelle von Untergrundpaaren ist. Unsere Simulationen, die eine Beschreibung des kombinatorischen Untergrundes mit Paaren gleicher Ladung einschließen, zeigen, dass nach einer Woche Strahlzeit eine Bestimmung der Ausbeute an echten Paaren aus Zerfällen in der $\rho - \omega$ -Massenregion möglich ist.

Abstract

In the FAIR project considerable updates of accelerator facilities at the GSI Darmstadt are projected. The available beam energies of the new SIS100 and SIS300 accelerators will be in the range of 8 AGeV to 25 AGeV and above. Experiments with both elementary probes and heavy-ions at beam energies ≤ 3.5 AGeV have been performed with the HADES detector at SIS18. This thesis examines the dielectron detection capabilities of HADES at the new facilities, focusing on carbon–carbon collisions at kinetic beam energies $T = 8 \dots 25$ AGeV. An event generator based on the relativistic transport code UrQMDv1.3p1 has been implemented. Predictions of the UrQMD model are examined and compared with the available experimental database. The results for our dilepton cocktail are compared with cocktails based on m_t scaling or a transport code. In the $\rho - \omega$ mass region, photon conversion $\gamma \rightarrow e^+e^-$ is found to be an important source of combinatorial background pairs. Nevertheless, this stage of the simulations, including a description of the combinatorial background with like-sign pairs, points to the possibility of a determination of the yield of true pairs from particle decays in the $\rho - \omega$ mass region after one week of beam time.

Contents

1	Introduction: Experiments with Heavy Ions	9
1.1	Describing heavy-ion collisions	10
1.1.1	Thermodynamic models	10
1.1.2	Microscopic-dynamical models	11
1.2	Experiments	12
1.3	HADES at SIS100	14
1.4	Outline of this thesis	16
2	The HADES experiment	17
2.1	The HADES setup	17
2.1.1	Lepton identification: The RICH detector	17
2.1.2	The spectrometer	18
2.1.3	The META detector	19
2.1.4	The Start and Veto detectors	20
2.2	The experimental trigger	20
3	Simulation	21
3.1	An event input for a detector simulation	21
3.2	The UrQMD event generator	25
3.2.1	Cross sections	26
3.2.2	Transverse mass spectra	30
3.2.3	Particle yields: Comparison with other cocktails	33
3.2.4	Geometrical acceptances	37
3.3	Additional decays with Pluto	40
3.4	Limited detector resolution and multiple scattering	41
4	Results of the simulation	45
4.1	Rapidity distributions of single electrons and positrons	45
4.2	Results for pairs	47
4.2.1	Quality cuts	48
4.2.2	Cocktail composition	49
4.2.3	Rapidity distributions	51
4.2.4	Combinatorial background and like-sign method	53
4.2.5	Invariant mass spectra	53
5	Summary	63

Appendix A Analysis with HADES	64
A.1 Reconstruction of hits in subdetectors	64
A.2 Combining subdetector information	66
A.3 Reconstructing pair variables	66
Appendix B UrQMD: Phase space distributions of particles	68
Appendix C Technical aspects of the Pluto event generator	81
Appendix D Proton–Proton collisions with Pluto	82
Appendix E Abbreviations	86
Bibliography	87

List of Figures

1.1	Sketch of the CBM experiment	14
2.1	The HADES detector	18
3.1	Calculation flow card for cocktail generation	24
3.2	Total, inelastic and elastic cross section	27
3.3	1π exclusive cross sections	28
3.4	Inclusive π cross sections	28
3.5	multi- π exclusive cross sections	29
3.6	Exclusive η cross sections	29
3.7	Exclusive ω , ρ^0 and K meson cross sections	30
3.8	ρ^0 cross sections	31
3.9	Inclusive meson cross sections	31
3.10	Transverse mass spectra for various mesons	32
3.11	Transverse mass spectra	33
	(a) Transverse mass spectra for pions	33
	(b) Transverse mass spectra for kaons	33
3.12	Hadron multiplicities at $T = 8 \text{ AGeV}$	35
3.13	Hadron multiplicities at $T = 25 \text{ AGeV}$	37
3.14	Phase space distributions of π^0 mesons	38
3.15	Phase space distributions of ρ^0 mesons	39
3.16	Phase space distributions of ϕ mesons	40
3.17	Smearred momenta of e^+ and e^-	42
4.1	Phase space distributions of single e^\pm from π^0 meson decays	46
4.2	Single e^\pm from ρ^0 meson decays	47
4.3	Single e^\pm from ϕ meson decays	48
4.4	Opening angle distributions	49
4.5	Preliminary invariant mass spectra	51
4.6	Rapidity distributions of dielectrons	52
4.7	Combinatorial background and like-sign method	54
4.8	Invariant mass spectra	57
4.9	Invariant mass spectra of different cocktails	59
4.10	Background composition	60
4.11	Signal-to-background ratio	61
B.1	Phase space distributions in CC collisions at $T = 2 \text{ AGeV}$	69
B.2	Phase space distributions in CC collisions at $T = 8 \text{ AGeV}$	72

B.3	Phase space distributions in CC collisions at $T = 15$ AGeV	75
B.4	Phase space distributions in CC collisions at $T = 25$ AGeV	78
D.1	Cross sections for pp collisions	84
D.2	ρ^0 production cross section in pp collisions	85
D.3	Invariant dilepton mass spectrum	85

List of Tables

1.1	Heavy-ion experiments with leptons	15
3.1	Decay branching ratios for UrQMD post-processing	22
3.2	Hadron multiplicities for CC collisions	34
3.3	Hadron multiplicities for AuAu collisions	36
3.4	Geometrical acceptance for different particle species	39
4.1	Acceptance for dielectron pairs	50
4.2	Charged particle multiplicities	60
D.1	Primary channels $pp \rightarrow X$	82
D.2	Decay channels and branching ratios of unstable particles	82

1 Introduction: Experiments with Heavy Ions

The non-abelian gauge theory of the strong interaction, QCD¹, has been very successful in describing strong interactions at high energy scales (e.g. at energies $\sqrt{s} \gg \Lambda_{QCD}$ and correspondingly large momentum transfers, where Λ_{QCD} is the characteristic QCD scale parameter in the order of a few 100 MeV). It is formulated as the coupling of elementary, strongly interacting particles, the *quarks*, to the respective gauge fields, the *gluons*. Since the coupling strength of the strong interaction α_s drops with rising momentum transfer, leading to *asymptotic freedom*, in the high-energy regime a perturbative treatment is possible. On the other hand, the strong rise of α_s at lower energies up to $\mathcal{O}(\alpha_s) \approx 1$ makes the same perturbation technique inapplicable. Here, the theory of strong interactions is built up from at first glance totally different quantities based on the hadronic degrees of freedom. The compositeness of hadrons as strongly interacting particles made of quarks and gluons is encoded, e.g., in form-factors and structure functions.

Moreover, quarks do not provide appropriate objects for studying the properties of strong interactions at low energies, since they cannot be observed as isolated particles. The more they become separated, their coupling becomes stronger and stronger, finally causing the production of quark–anti-quark pairs, that screen the field of the quarks being separated and leading to bound hadronic states. The simplest particles built up from quarks, the *mesons*, that are composed from a quark and an anti-quark, nevertheless, have properties well known from many experiments [1].

The lightest quarks u (*up*) and d (*down*) have current-masses² of about 10 MeV at a scale of $\mu \approx 2$ GeV, while the lightest mesons belonging to the π meson isospin triplet (π^+ : $u\bar{d}$, π^- : $d\bar{u}$, π^0 : $(u\bar{u} - d\bar{d})/\sqrt{2}$), have an averaged mass of about 137 MeV in the vacuum [1]. The understanding of these two different scales on a fundamental level presents a key challenge to a deeper understanding of the strong interaction from the high-energy limit to the low-energy (vacuum) regime.

In central heavy-ion collisions at intermediate energies, i.e. SIS³18 energies, nuclear densities of up to $3\rho_0$ can be reached, where $\rho_0 = 0.16 \text{ fm}^{-3}$ is the baryon density of nuclear matter at ground state. The constituent quarks of a hadron are no longer left to couple to each other exclusively, but can also couple to other particles of the environment. One expects changes of hadron properties, in particular of vector mesons. These changes are in turn related to the high-density environment. Leptons, in particular electrons from electromagnetic or weak decays of short-lived hadrons, provide a convenient way to probe

¹Quantum-Chromo-Dynamics

²We use units where the speed of light is $c \equiv 1$.

³SchwerIonenSynchrotron

hadron properties in the high-density region. They do not suffer from strong interactions and leave the high-density reaction zone nearly undisturbed, thus providing an insight in hadron properties away from ground-state.

1.1 Describing heavy-ion collisions

Before being able to describe the possible changes of hadron properties in heavy-ion collision, as a prerequisite one needs an understanding of how particles are produced there. This includes an understanding of the final multiplicities of the specific hadron species and their phase space distributions. Since in a heavy-ion collision many particles are involved, different approaches exist, with different levels of complexity.

1.1.1 Thermodynamic models

Early, even before QCD was introduced, it was found that many properties of particles from high-energy reactions can be described by statistical concepts from thermodynamics [2]. As in classical thermodynamics, one is not troubled with understanding the subtle interactions among all particles involved, but merely describes an ensemble. One may choose a grand-canonical potential to account for particle production. The governing parameters of the system are then an appropriate common temperature T and chemical potentials μ_i for each particle. For hadron samples with small numbers of constituents one has to employ canonical or micro-canonical descriptions.

Fireball models

Being the key to a statistical thermodynamic description of hadronic interactions, *fireballs* are defined as states of excited hadronic matter. This may include resonances of baryons and mesons as well as again other fireballs. “*We describe by thermodynamics fire-balls which consist of fire-balls, which consist of fire-balls, which . . .*” [2].

All particles emitted from the fireball follow Boltzmann distributions⁴ as one may find e.g. from measured transverse mass spectra. With the beam oriented along the z -axis, the transverse mass of a particle with rest mass m is

$$m_t = \sqrt{p_t^2 + m^2} = \sqrt{p_x^2 + p_y^2 + m^2}, \quad (1.1)$$

where $p_t = \sqrt{p_x^2 + p_y^2}$ is the transverse momentum. m_t is not affected by Lorentz boost effects – these act on kinematic variables parallel to the beam axis. Experimentally, the m_t spectrum is found to follow a Boltzmann-like distribution, which may be written as

$$\log \left(\frac{1}{m_t^2} \frac{dN}{dm_t} \right) = am_t + b, \quad (1.2)$$

with parameters a and b to be adjusted to data. The slope parameter a appears as an “inverse temperature” and so may be used to experimentally define a temperature parameter at all.

⁴To be more specific, mesons follow Bose-Einstein statistics and fermions Fermi-Dirac statistics. For low occupation numbers, both statistics merge in the Boltzmann statistics.

Data from intermediate energy heavy-ion collisions also suggest the temperature extracted like this to be similar even for different particle species, whence the same underlying thermodynamics is suggested [3, 4].

Although this approach has proven to be fairly successful, small deviations from this behavior are known. For instance, the two prominent channels for pion production in a heavy-ion collision are the direct production in the primary collision and the decays, mostly of Δ resonances into pions. A fit of the m_t spectrum of pions shows that these two temperatures indeed differ as one would anticipate from the two mechanisms involved [5].

Nevertheless fireball models can be used to make statements about the centrality of the collision [6] or to calculate particle multiplicities [7].

m_t scaling

The description of particle production in a grand-canonical potential has few input parameters, particularly the above-mentioned temperature T and the chemical potentials μ_i for each particle species. The chemical potential would correspond, to some extent, to the particle's mass $\mu_i \sim m_i$ in a simple approach; the temperature is extracted from the particle abundance using eq. (1.2). The m_t scaling hypothesis (cf. e.g. refs. [8, 9]) suggested in high-energy physics assumes that the particle abundance at a given transverse mass m_t may be described by a distribution being universal for various hadron species. With the m_t scaling hypothesis one gets a guidance for the transverse phase space distributions and multiplicities of particles for which no experimental information is at disposal. By integrating over all momenta p_t obtains the average multiplicity of a specific particle of given mass, once one particle distribution is known experimentally as normalization.

1.1.2 Microscopic-dynamical models

The thermodynamic models described above make predictions without an explicit knowledge of the essential interaction among the particles, as they rely on certain equilibrium assumptions. However, when developing fundamental models of strong interactions, one would also like to make predictions for certain experimental cases, which may then be tested.

The propagation of every single particle involved in the heavy-ion interaction process may thus be implemented in a *transport code*. Interactions of particles are emulated with model cross sections or fits to available experimental data with Monte-Carlo techniques mimicking a part of quantum effects. Transport codes should be based on quantum kinetics. While such a fundamental framework may be generically formulated, e.g. as a coupled set of Kadanoff-Baym equations [10, 11], its numerical realization faces a series of problems. It is therefore conceivable that different *transport codes* may follow rather divergent approaches to the same problem because of the manifold aspects to consider. The same holds for model predictions, which often depend strongly on the underlying model assumptions.

Even so, we will try to summarize some of the quantities to take into account:

- While beam-target cross sections may be known from experiments for elementary hadron interactions, often only very sparse data for intermediate particles' interactions (*secondary interactions*) is available. Sometimes detailed balance may be used to conclude on cross sections. Models are needed to fill the gaps. E.g. string-fragmentation models are used to model multi-particle production at higher energies.

- *Cascade models* implement the excitation, propagation and decays of excited particle states. Decay branching ratios and interaction cross sections of excited states are often sparsely known and models are needed, which are adjusted to “vacuum data”, i.e. elementary interactions neglecting the influence of the ambient medium in heavy-ion collisions.
- The propagation of particles may be implemented in a mean-field potential of the environment or individual particle’s potentials or a mixture of both, and the results may obscure straight expectations deduced from differential cross section data. The coupling to the surrounding matter may introduce changes e.g. to the particles’ spectral functions most visible in changed production cross rates which are believed to stem from the change of the minimal energy required for a certain reaction. Attempts to explain the enhanced production of dileptons in the mass region $200 \text{ MeV} < m < 600 \text{ MeV}$ in nucleus–nucleus collision seen by the DLS experiment [12] follow this method.

Due to the observed differences (see e.g. ref.[13]) between elementary (in vacuum) and heavy-ion reaction at finite nuclear density, comparing elementary with heavy-ion reaction results remains crucial for the development of a successful description.

Using *transport codes* allows to make predictions on a possibly more fundamental basis than fireball models. However, since both try to describe the same physical event they should yield comparable results. Moreover, microscopic transport calculations may be used to study the thermodynamic properties of a collision, whereas fireball models have to make assumptions on these properties; e.g. thermal equilibration (same temperature, not necessarily same energy density) can be tested for proton-nucleus collisions, see e.g. [14], as well as rapidity distributions from thermal models [15]. Furthermore the time evolution can be studied with transport models as well as the influence of the available degrees of freedom [16].

The gap between fireball models and transport models is bridged by hydrodynamic models. These assume local thermal equilibrium in either the subcomponents of the medium or the medium as a whole and evolve them according to local energy-momentum and current conservation. Often, hydrodynamical models are applied for the description of a part of the time evolution only, while transport codes are aimed to be applicable for the complete course of a heavy-ion collision.

1.2 Experiments

Experiments with heavy ions are almost naturally concerned with a large hadronic background. Most hadrons, if produced in the dense interaction zone, suffer from strong interactions on their way to the detector, leading to a major information loss. This poses a grave obstacle for the study of the internal properties of the high density zone, e.g. via the analysis of the hadronic decay products of vector mesons from a heavy-ion collision.

A possible solution is the use of penetrating probes that do not take part in strong interactions at all, e.g. leptons. If these leptons stem from decays of short lived mesons that decay inside of the fireball, they carry essentially undisturbed information about the early stages of the interaction zone to the detector. Measuring e.g. the invariant mass spectra of

electron–positron pairs (dielectrons, more general dileptons), one gains a valuable glimpse on predicted changes of the vector meson spectral functions.

Here experimentalists are faced with several challenges:

High multiplicities: Depending on the actual detector geometry, there may be hundreds of particles flying into the geometrical acceptance, each possibly producing detector interactions to be reconstructed.

For a heavy-ion collision, already the input channel contains a plenitude of particles, e.g. for a calcium-calcium collision $40 + 40$ nucleons. Depending on the bombarding energy this already high number will easily go up, e.g. for a gold-gold collision at around 10 AGeV kinetic bombarding energy $197 + 197 + 600$ secondaries.

High background: Leptonic decays of heavier mesons are rare processes on the order of 10^{-4} or below (e.g. the branching ratio for the decay $\rho^0 \rightarrow e^+e^-$ is $(4.67 \pm 0.09) \times 10^{-5}$ [1]). The problem is not only in identifying the true leptons from myriad of hits of a high-multiplicity background, but also in the many ways these background processes may create leptons, namely δ -electrons from in-target or in-detector interactions and Dalitz decays of π mesons $\pi \rightarrow \gamma e^+e^-$ with a branching ratio of $1.198 \pm 0.032\%$. Other important dielectron sources are Δ and η Dalitz decays.

Acceptance: Currently, heavy-ion experiments at intermediate energies operate with a fixed target because of the available accelerator facilities. Since there is always a high probability of no beam–target interaction, a hole in forward direction is in virtually all experiments unavoidable to limit detector damage. With increasing beam energy, the kinematics imposed by a fixed target will limit the accessible region to a smaller and smaller forward cone, that is, due to the hole in forward direction, only partially covered by detectors.

The CBM experiment at FAIR

To study properties of hadronic matter at high nuclear densities, major updates of the accelerator facilities at the GSI⁵ Darmstadt are planned [17]. The projected synchrotrons SIS100/SIS200 at the new FAIR⁶ facility are designed to reach high beam intensities of up to 10^9 U^{92+} ions per second at a beam energy of 22.3 AGeV [18]. Actually, SIS200 is substituted by SIS300 with higher available beam energy.

The CBM⁷ experiment was proposed to investigate possible in-medium effects and the hadronic equation of state accessible in this energy range. One possible setup for the CBM experiment is sketched in fig. 1.1. In the setup shown, the existing HADES⁸ detector is to be placed in front of the CBM setup. The target is positioned at the entrance of the HADES detector. In this way a good geometrical coverage is reached: particles emitted from the target at large polar angles are measured with the HADES detector, while particles emitted at small forward angles are measured with the CBM setup.

In the following we present estimates of dilepton yields from pp, CC and AuAu yields, especially of lepton pairs emitted inside the HADES geometrical acceptance for energies

⁵Gesellschaft für SchwerIonenforschung

⁶FAcility for Ion Research

⁷Compressed Baryonic Matter

⁸High Acceptance Di-Electron Spectrometer

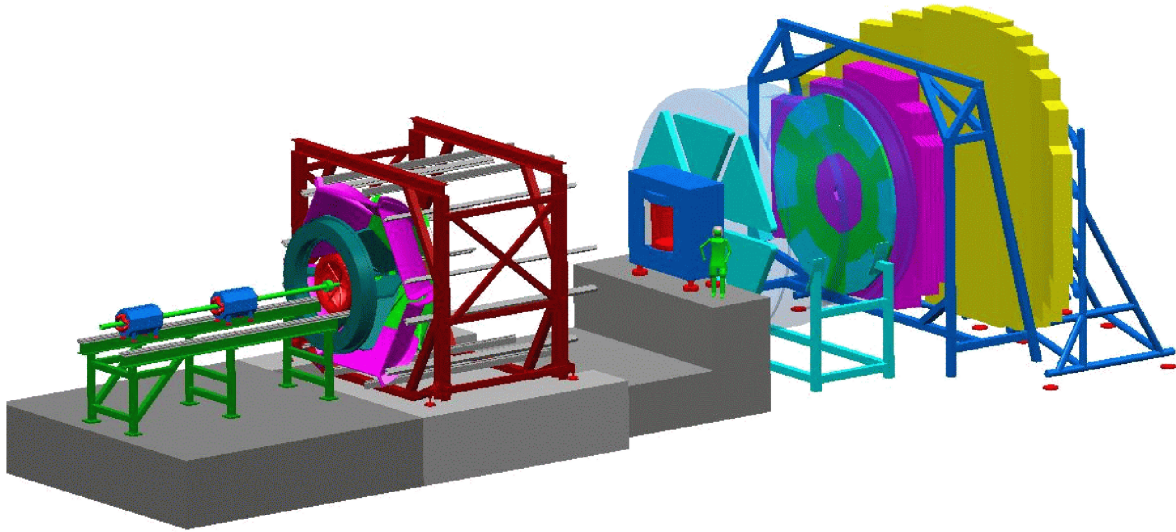


Figure 1.1: Sketch of the CBM setup (right) with the HADES detector (left) [19]. The beam enters from the left. The HADES detector is explained in section 2.1; for the CBM setup see [19].

between 2 AGeV and 25 AGeV. We will also address the amount of background to expect from photon conversion inside the HADES detector and from combinatorial pairs.

1.3 HADES at SIS100

An interesting option for FAIR is to operate HADES at SIS100 [18], either in conjunction with CBM or independently. Since the HADES detector has been optimized for fixed-target heavy-ion experiments at beam energies up to $T = 2$ AGeV, it is not clear by itself if the HADES setup is suitable for measurements in the energy range of SIS100. Furthermore, as the CBM collaboration is still discussing whether to outfit the CBM detector with dedicated dielectron or dimuon sensitive components, studies of the capabilities of the HADES detector at higher beam energies may show if HADES may also operate at lower SIS300 energies and CBM may, in such a case, specialize on the dimuon option. Simulations by the R ez group seem to indicate, that HADES may successfully operate at SIS100 energies of $T \leq 8$ AGeV; here we also extend the energy scan to higher beam energies up to $T = 25$ AGeV.

Owing to their small interaction probability with the environment, electromagnetic probes (dileptons and photons) may supply information on early and high-density states of hadronic matter in heavy-ion collisions. The emission rates for photons and dileptons are [20]

$$q_0 \frac{dN_\gamma}{d^4x d^3q} = -\frac{\alpha_{\text{em}}}{\pi^2} f^B(q_0; T) \text{Im}\Pi_{\text{em}}^T(q_0 = q; \mu_B, T), \quad (1.3)$$

$$\frac{dN_{e^+e^-}}{d^4x d^4q} = -\frac{\alpha_{\text{em}}}{M^2 \pi^3} f^B(q_0; T) \text{Im}\Pi_{\text{em}}(M, q; \mu_B, T), \quad (1.4)$$

where local equilibrium is assumed. Here, q denotes the dilepton four-momentum; in case of photons the energy q_0 equals the magnitude of the three-momentum $|\vec{q}|$. μ_B stands

beam	energy [GeV]	reaction	experiment	probe	
Bevalac	1, 2	C(a) + C(a)	DLS	e^+e^-	
SIS	1 - 2	C + C	HADES	e^+e^-	
SPS	40	Pb + Au	CERES	e^+e^-	
		In + In	NA60	$\mu^+\mu^-$	
	158	Pb + Au	CERES	e^+e^-	
		Pb + U	NA50	$\mu^+\mu^-$	
		Pb + Pb	WA98	γ	
		200	S + Au	CERES	e^+e^-
			S + U	NA38	$\mu^+\mu^-$
			S + W	HELIOS-3	$\mu^+\mu^-$
	RHIC	130 +130	S + Au	WA80	γ
			Au + Au	PHENIX	e^\pm, e^+e^-
200 +200		d, Au + Au	PHENIX	$e^\pm, e^+e^-, \mu^+\mu^-$	
130 +130		Au + Au	STAR	γ	
200 +200	d, Au + Au	STAR	e^\pm		

Table 1.1: Heavy-ion experiments with leptons and photons [26]

for the baryon chemical potential and α_{em} is the electromagnetic fine structure constant. The essential quantity is the retarded photon self-energy described by Π_{em} . Within the Vector-Meson Dominance model the coupling of the virtual photon to strongly interacting matter is mainly via vector mesons, that have the same quantum number as the photon, 1^- . Thus, virtual photons may probe vector mesons directly. Of particular interest is the electromagnetic decay of vector mesons in dense and hot matter. Various models predict partially sizable modifications of the vector mesons (cf. ref. [21] for a review, ref. [22] for the ω meson). These changes may be related to fundamental symmetries of strong interactions, like the chiral symmetry breaking and its restoration [21], to the changes of QCD condensates [23, 24, 25], or in a pure hadronic picture to peculiarities of interactions among hadrons.

Given such a strong motivation, the HADES detector as a second generation device was constructed and put into operation in the energy range of $T = 1 - 2$ AGeV at SIS18 – the first generation experiments were by the DLS⁹ collaboration [12] with partially puzzling results. Going up in beam energy, the next heavy-ion experiments with leptons were performed by CERES at a beam energy $T = 40$ AGeV at CERN¹⁰. Further experiments are surveyed in tab. 1.1.

Evidently there is a gap in the inspected beam energies. Experiments at relativistic beam energies were performed to search for deconfinement effects. Here the hadronic medium is dominated by mesons, while at intermediate energies baryons (nucleons) are dominating. The transition between baryon-dominance and meson-dominance falls just in the energy regime of SIS100/300. Systematics of the beam energy dependence [27] of thermal freeze-out conditions ascertain that experiments at SIS100/300 will operate in a range of maximum baryon densities. The window opened into this region of the phase diagram is the main motivation of the CBM experiment. In this context it is worth mentioning that the experiments

⁹DiLepton Spectrometer¹⁰Conseil Européen pour la Recherche Nucléaire

at AGS¹¹ as well as experiments taking data during the low energy runs at CERN did not measure electromagnetic probes, so HADES and/or CBM have the capability to fill the gap in the electromagnetic excitation function. The very low energy run at RHIC¹² presently under discussion ($\sqrt{s_{NN}} = 6 \dots 12$ AGeV) is unlikely to be able to collect sufficient statistics for sensible electromagnetic signal measurements.

1.4 Outline of this thesis

In this thesis simulations for heavy-ion collisions at typical beam energies of SIS100 up to SIS300 energies are presented. Generic tools for event generation are implemented with publicly available software, which are also applicable for further simulations to accompany future experimental data analysis or to prepare experiments.

This thesis is structured as follows:

- Chapter 2 gives an outline of the HADES setup.
- Chapter 3 introduces the implementation of the event generator with the transport code UrQMD¹³ and the Pluto event generator. Predictions of the UrQMD model for particle production cross sections and phase space distributions are presented. The phase space distributions of particles produced in heavy-ion collisions are displayed.
- Chapter 4 presents results for (di-)leptons obtained from our simulations.
- The summary is in chapter 5.
- Chapter 5 summarizes this thesis.

¹¹Alternating Gradient Synchrotron

¹²Relativistic Heavy Ion Collider

¹³Ultra-Relativistic Quantum Molecular Dynamics

2 The HADES experiment

2.1 The HADES setup

The HADES setup was explicitly designed and built for the study of dileptonic (e^+e^-) decays of vector mesons in heavy-ion collisions as well as in elementary reactions [28, 29, 30, 31]. Of course, experiments with light projectiles (deuterons, protons, pions) are also feasible. HADES is a fixed-target installation optimized for SIS18 energies ($T \leq 2$ AGeV). In central heavy-ion collisions one expects the formation of zones of high nuclear density, which hold potential for the study of both the nuclear equation of state and the influence of the medium on hadronic properties.

Leptonic decays of ρ , ω and ϕ mesons are rare processes with branching ratios on the order of 10^{-5} , thus several key requirements for the spectrometer have to be met:

- good and fast lepton identification for a fast selection of candidates of lepton events on-line and thus reducing the amount of data to store and analyze off-line.
- robustness in the high-multiplicity environment of heavy-ion collisions.
- high geometrical acceptance to reconstruct dilepton pairs and possibly exclusive events.
- high mass resolution in the $\rho - \omega$ mass region for testing theoretical predictions of in-medium modifications of spectral functions of hadrons.

The HADES detector was designed with full azimuthal coverage in ϕ . The polar acceptance in the laboratory system ranges from θ angles of 18° to 85° leading to a geometrical acceptance for pairs of roughly 50% in both the ω mass region and the π mass region [28, 32]. Reaction products emitted in the geometrical acceptance face the following detector components: the RICH¹ detector, two inner layers of MDCs², the toroidal magnetic field, two outer layers of MDCs and for angles larger than 45° the TOF³ detector or for smaller angles the low-granularity TOFino detector and the Pre-Shower detector. These components are briefly described in the following sections, since detailed simulations have to take the detector structure into account.

2.1.1 Lepton identification: The RICH detector

Because of the high multiplicity expected, HADES is equipped with a hadron blind RICH detector for lepton identification. On passage through the radiator gas high- β particles

¹Ring Imaging CHerenkov detector

²Multiwire Drift Chamber a.k.a. Mini Drift Chambers

³Time-Of-Flight

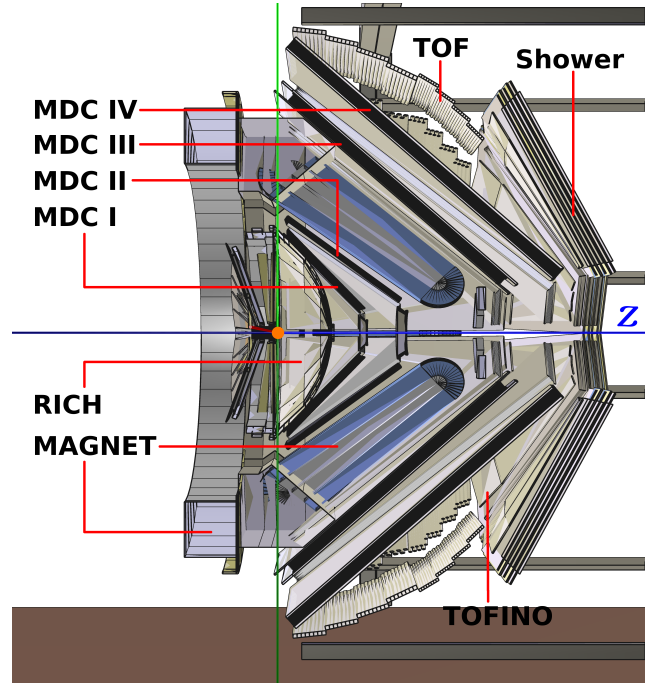


Figure 2.1: Cross section of the HADES detector. The beam axis runs along the z axis. The target is positioned inside of the RICH detector (orange dot). The picture was created from HGeant geometry files.

emit Cherenkov radiation.⁴ The emitted light cone is then reflected from a spherical mirror positioned in forward direction, to photocathodes placed behind the target. A fast, hardware implemented pattern recognition unit (RICH-IPU⁵) reconstructs rings from the detector hits providing a lepton trigger.

2.1.2 The spectrometer

The MDC detector

The HADES setup is equipped with 4 layers of MDCs, of which the third layer was constructed at the Forschungszentrum Rossendorf. Each layer is split into 6 trapezoidal sectors. The active area of the sectors range from 0.35 m^2 up to 3.2 m^2 . Each MDC module has 6 layers of parallel sense and field wires separated by cathode wire layers. The drift cells have sizes between $5 \times 5\text{ mm}^2$ for the innermost chambers up to $14 \times 10\text{ mm}^2$ for the outermost ones [33]. A traversing particle ionizes the chamber's filling gas along its path. The newly produced ions and electrons then drift to cathode and anode wires respectively. The electrons are strongly accelerated in the high field close to the anode wire, creating an avalanche of charged particles. The charge multiplication leads to a measurable signal. To achieve good spatial reconstruction of detector hits, the sense wire layers have different orientations leading to angles of $+40^\circ$, -20° , -0° , $+0^\circ$, $+20^\circ$, $+40^\circ$ for each layer (the trapezoid's parallel sides are at 0°).

The toroidal magnet

Between the second and third MDC layer a toroidal, non-focusing magnet consisting of 6 superconducting coils is placed. Each coil is cooled with liquid helium to an operational

⁴ $\beta = v/c$ is the normalized particle velocity.

⁵RICH Image Processing Unit

temperature of 4.6 K, yielding at the maximum current of 3665 A a magnetic field between 2.4 T near the coils and about 0.8 T in the center of the sector [34].

2.1.3 The META detector

The TOF, TOFino and Pre-Shower subdetectors are commonly referred to as the META⁶ detector. The META's subdetectors' aptitude in measuring the event's multiplicity is expressed in this logical grouping. Hits in every META detector can also be matched with reconstructed MDC tracks offering the possibility for qualitative selection of reconstructed tracks.

The TOF detector

To provide time-of-flight information the TOF detector has been placed behind the fourth MDC layer covering angles from 44° to 88°. The TOF detector has also sixfold symmetry in ϕ , each sector consisting of arrays of 8 modules of various lengths with θ . Each module is subdivided into rows of 8 scintillation rods with square diameter, each one being read out on both ends with fast photomultipliers and consequently allowing determination of the hit position along the module via time differences. TOF has a time resolution of about 150 ps and a spatial resolution along the rods axis of about 2 cm [35].

Owing to their small mass, electrons and positrons have much higher velocities than any other particles measured in the experiment. With the good time resolution in TOF one has thereupon another particle identification criterion at hand (along with the information obtained from RICH and the tracking in the MDCs). Similar to the MDCs, energy loss can be measured and used for particle identification.

The TOFino detector

A second, low granularity time-of-flight detector, TOFino, is placed behind MDCIV at polar angles from 18° to 44°. TOFino has 6 modules in ϕ . These modules are divided in 4 pads. The pads are read out on one side only; the position resolution is thus limited to the actual pad hit. The time resolution is 500 ps [35]. Due to pure kinematic reasons, in a high-energy collision most particles are emitted at forward angles and may necessarily produce hits in the TOFino region. For a carbon-carbon collision experiment at 2 AGeV about 20% of the reconstructed hits in TOFino belong to two or more physical tracks. TOF's awaited replacement with RPCs⁷ will show considerable improvements.

The Pre-Shower detector

For additional electron/positron identification in the forward direction, where most particles are fast and particle identification by time-of-flight becomes impractical, the Pre-Shower detector has been placed behind TOFino. Following the sixfold symmetry of the whole detector, it is divided in 6 modules, each consisting of 3 wire chambers separated by lead converters. A particle passing through the converter radiates high energy bremsstrahlung. The bremsstrahlung photons then predominantly convert to high-energetic electron-positron

⁶Multiplicity Electron Trigger Array

⁷Resistive Plate Chambers

pairs mostly, which may again radiate bremsstrahlung leading to an avalanche of charged particles. The wire chambers allow observation of the development of the avalanche and thereby measure the energy loss of the incident particle, the latter being connected to the particle's mass and charge.

2.1.4 The Start and Veto detectors

The Start and Veto counters are thin detectors optimized for the specific beam used and placed before and after the target. If both detectors are hit in an event, it is discarded and not further processed, since beam and target particles interacted at best weakly. The Start detector also provides a timing signal for the start of the event.

2.2 The experimental trigger

Since dileptons from vector meson decays are rare, it is crucial for the experiment to keep the amount of background events to store and to analyze off-line under control as early and as sufficiently as possible. Correspondingly, beam intensities of up to 10^8 particles per second are needed to collect enough statistics, a rate much too high to be handled with reasonable effort. Therefore, an efficient trigger is mandatory.

The first level trigger: A first selection of events is done based on the multiplicity measured in the META detector (TOF, TOFino and Pre-Shower).

Since the multiplicity of particles produced in a heavy-ion collision is correlated with the centrality of the collision, the first level trigger may thus preselect events of lower impact parameter in which higher nuclear densities are achieved. With the first level trigger a reduction of the data rate of a factor of up to 10 is reached [35].

The second level trigger: To pre-select lepton events fastly, hardware-based pattern recognition algorithms were implemented in the RICH selecting events with rings, in the TOF further limiting the selection to events with particles of large time-of-flight and in Pre-Shower triggering on events with electron signature.

Correlating the information of the subdetectors with respect to matching quality and angles between different selected electron candidates provides a reduction of the data rate by a factor of up to 10 [35]. Further restricting the selection on opposite-charge candidates with opening angles higher than 20° the second level's reduction rate may be as high as a factor of 100 [35].

3 Simulation

To give an estimate of the analysis potential of the HADES detector setup at beam energies between $T = 8$ AGeV and $T = 25$ AGeV at the planned SIS100/SIS300 accelerator facility of FAIR, a full cocktail of events for carbon–carbon collisions has been calculated. The following key questions are addressed:

Acceptance: The HADES setup covers polar angles from 15° to 85° . How does the limited angular coverage affect the acceptance of electron–positron pairs from particle decays?

Combinatorial background: We have to expect background electrons/positrons from photon conversion $\gamma \rightarrow e^+e^-$ and from leptonic decays of abundantly produced π^0 mesons: $\pi^0 \rightarrow \gamma e^+e^-$ (branching ratio 1.2×10^{-2}). Since both processes may take place in the target or in the RICH detector, we have no criterion to distinguish these leptons from decay remnants we are interested in. What are the properties of the combinatorial background, and do we have chances to remove it from our analysis?

3.1 An event input for a detector simulation

The first decision to be made is how to generate the physical events for the simulation. Apparently we have two choices: either generate a particle *cocktail* from fireball sources or use a publicly available transport code. We have to consider two possibly linked aspects:

- How much input from our side is needed to set up the model?
- How reliable are the results? Directly connected to this question is the number of input parameters needed for the specific model.

Since no *out-of-the-box* fireball cocktail generator is available, we could define a fireball cocktail ourselves. The HADES simulation software includes the Pluto event generator [36, 37]. Pluto may generate particles from thermal sources; so by superimposing such Boltzmann-distributed generators for different particle species weighted by their respective multiplicity we could generate a cocktail, as it was done before [38]. Nevertheless, we would have to supply multiplicities for every particle species and the radial expansion velocity of the fireball (which may as well be different for every particle species).

Cross sections for π and η production in pp collisions have been measured in the region of our interest, but data for many particle species is so scarce that we would have to rely on strong extrapolations or apply theoretical assumptions like m_t scaling (cf. page 11).

process	BR PDG	enhanced BR
$\Delta^+ \rightarrow pe^+e^-$	4.0×10^{-5}	1
$\omega \rightarrow e^+e^-$	7.14×10^{-5}	1
$\omega \rightarrow \pi^0 e^+e^-$	5.9×10^{-4}	1
$\rho^0 \rightarrow e^+e^-$	4.67×10^{-5}	1
$\phi \rightarrow e^+e^-$	2.98×10^{-4}	1
$\eta \rightarrow 2\gamma$	39.4%	unchanged
$\eta \rightarrow 3\pi^0$	32.5%	unchanged
$\eta \rightarrow \pi^+\pi^-\pi^0$	22.6%	unchanged
$\eta \rightarrow \pi^+\pi^-\gamma$	4.68%	unchanged
$\eta \rightarrow e^+e^-\gamma$	6.0×10^{-3}	unchanged
$\eta \rightarrow \mu^+\mu^-\gamma$	3.1×10^{-4}	unchanged
$\eta \rightarrow e^+e^-$	$< 7.7 \times 10^{-5}$	6.0×10^{-6}
$\eta \rightarrow \mu^+\mu^-$	5.8×10^{-6}	6.0×10^{-6}
$\eta \rightarrow$ all above	99.2%	100%
$\pi^0 \rightarrow 2\gamma$	98.8%	unchanged
$\pi^0 \rightarrow e^+e^-\gamma$	1.2%	unchanged
$\pi^0 \rightarrow$ all above	100%	100%

Table 3.1: Decay branching ratios for UrQMD post-processing. The PDG [1] values are listed without their errors. In the upper part of the table, enhanced decays to dielectrons are shown, in the lower part unchanged decays of background dielectron sources.

On the other hand, the widely used transport codes HSD¹ [39] and UrQMD [40, 41, 42] do not support leptonic decays in their publicly available versions.^{2,3} However, the Pluto event generator is capable of calculating decay kinematics for any given process. Even anisotropies may be included.

We will apply the following procedure (see also the schematic diagram in fig. 3.1):

1. We generate events with the microscopic transport code UrQMD (no leptons), recording the full event history. We do not change lifetimes of particles, but let everything decay into the implemented hadronic channels. We save the whole time evolution of the reaction (extended output to the UrQMD output file called `file16`).
2. We then implement the enhanced dileptonic decays of Δ^+ , ω , ρ^0 and ϕ into the UrQMD file. The decays we process are listed in tab. 3.1 with the respective measured and enhanced branching ratios. The decay branching ratios of these processes are of the same order:

- (a) Find instances where particles from UrQMD decayed hadronically, for which we would like the leptonic channels included. One particle is chosen randomly.⁴

¹Hadron String Dynamics

²At the time of writing, the current publicly available version of HSD is 2.0. Dileptons are included in version 2.5. The code is available from the HSD website <http://th.physik.uni-frankfurt.de/~brat/hsd.html>

³Whenever mentioning UrQMD we are implicitly referring to version 1.3p1 available from the UrQMD website <http://www.physik.uni-frankfurt.de/~urqmd/>.

⁴In the considered energy range the dilepton sources in tab. 3.1 are rare. So are their dileptonic decays. Multiple occurrences of the enhanced processes in the same event are unlikely.

This ensures a correct estimation of the lepton multiplicity in the event and the combinatorial background to expect. The following variables of the decaying particle are recorded: location \vec{r} , momentum \vec{p} , mass m and the particle species.

- (b) Calculate the properties of the leptonic decay products with Pluto. Pluto is initialized with the exact parameters delivered by UrQMD: \vec{r} , \vec{p} , m and particle species.
 - (c) The Pluto-generated decay products are then merged with the original UrQMD event. The weight of the event is altered, according to the process enhanced and the event's multiplicity of sources to enhance, see tab. 3.1. For proton-proton collisions the now obsolete decay products from UrQMD may be removed in order to not change the event's multiplicity too much (e.g. typically a $M = 4$ trigger is used; not removing the hadronic decay products would lead to $M \geq 6$).
3. In a next step the decays of π^0 and η are implemented. These particles are stable in UrQMD.⁵ We do not change the decay branching ratios, since these particles are neither extraordinarily rare, nor have small leptonic decay branching ratios. The dominant decay $\pi^0 \rightarrow 2\gamma$ is a prominent source of photons that may convert into e^+e^- pairs in the target/detector material.

We initialize Pluto as before, but now with the final state π^0 and η mesons, and append the decay products to the event. The decayed particles are removed from the event. We process all decays, since no particular one was enhanced. Furthermore, the weight of the event is not changed.

4. To take into account photon conversion $\gamma \rightarrow e^+e^-$ in the target and in the RICH detector, we process the final state photons with a macro written by Marcin Wisniowski [43], which does the following: The probability for conversion of a photon of given energy is known. Initialized with a photon of momentum \vec{p} the conversion code makes a decision whether conversion takes place with Monte-Carlo methods. If conversion occurs, the momenta of the e^+e^- pair can be read out. We process every final state photon once with the macro and, on occurrence, we append the conversion e^+e^- to the event.
5. Next we remove all particles but e^+ or e^- from the event to save disk space.
6. The output is saved to a file suitable for analysis and as possible input for a detector simulation with the Geant3 [44] based detector simulation software HGeant.

This method yields events with dileptonic decays strongly enhanced, thus we are able to study the properties of rare processes, while all properties of primary particles are calculated in a microscopic transport calculation. The strong enhancement leaves us with many rare events of a small weight, i.e. the relatively frequent dileptonic decay $\pi^0 \rightarrow \gamma e^+e^-$ is to be scaled down to a weight $\sim 10^{-5}$. To guarantee a realistic estimation of abundantly produced particles with relatively large leptonic branching ratios, we skip step 2 (enhancement) in the above scheme in a second run. This way the dileptonic decay channels from abundant particles do not suffer from an artificial suppression that would be imposed if we would force the enhancement of a rare decay in every event. We use the same UrQMD events there, since

⁵I.e., there is no decay channel for these particles in UrQMD.

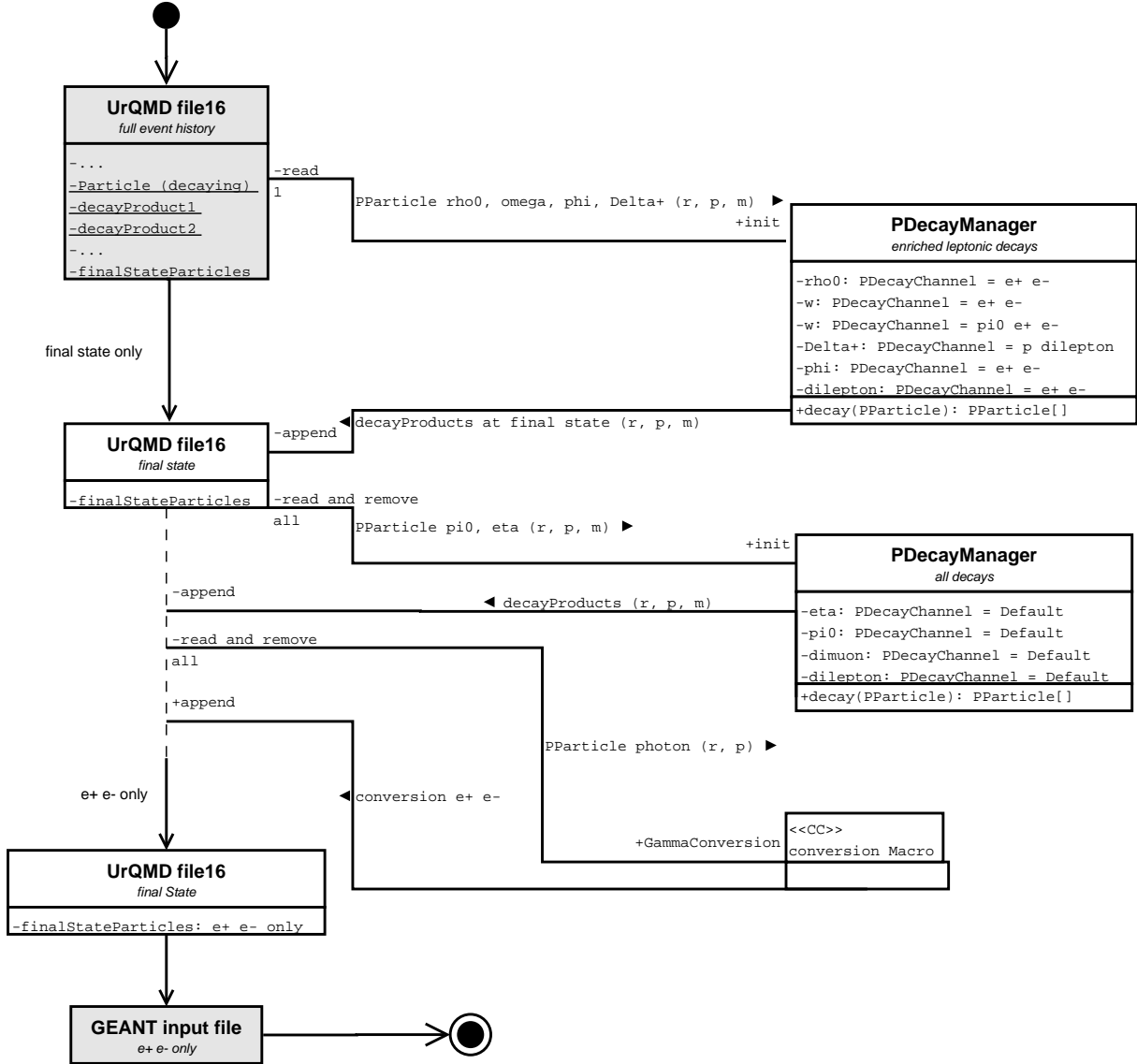


Figure 3.1: Calculation flow card for cocktail generation. Processing starts at the top and exits at the bottom. Information flow is shown with arrows pointing from origin to target. In the UrQMD file16 only one decay process is shown; omitted information is denoted with ellipses.

the decays and conversion are processed in an additional Pluto calculation. Both for the enhanced and unchanged cocktail we calculate the same number of events, i.e. we implant an enhanced decay in every second event.

The above mentioned procedure has been implemented in a C++ code. By virtue of this scheme we can avoid working out many error-prone input parameters by ourselves. We hand this task over to a widely used and well tested transport code. Moreover we provide an additional estimate of HADES's capabilities at higher energies from a different input than [38]. Furthermore, by using a microscopic transport code as our starting point, our dileptons are correlated to the hadronic background of the event. This may be useful for later studies of background rejection strategies, especially for proton–proton collisions.

3.2 The UrQMD event generator

Using UrQMD as the main part of the event generation, it is noteworthy to introduce its key features:

- UrQMD is a microscopic transport code providing a full hadronic simulation of the reaction dynamics based on elementary reactions.

Particles are propagated for an optional time and may undergo collisions with other particles or change their direction due to interaction with external fields.

With the coupling of particles to the fields of the environment in-medium effects can be explored.

- Strong interactions are simulated. The included interaction cross sections are tuned to reproduce experimental data or are motivated from theory (e.g. detailed balance).

UrQMD also includes surface terms of the interacting volume.

Electromagnetic fields are taken into account for particle propagation.

- Nucleons are modeled with Fermi motion.
- UrQMD is a *cascade-like* model: Apart from string excitation and string fragmentation a big part of the reaction dynamics is modeled via the excitation, propagation and decay of hadronic resonances.

The highly excited baryons have not been measured with high precision yet. In UrQMD the branching ratios for these cases are always inside the experimental limits [1], but tuned to measured production rates of secondary particles [40].

- UrQMD includes strange particles but no charmed particles.
- UrQMD does not include any leptons. Neither semi-leptonic decays nor leptonic particles are implemented.

Reference [45] summarizes predictions made with the UrQMD code. To get a feeling for UrQMD and to confront its results with the database, we additionally compare some predictions with available data on the following pages. Owing its concept UrQMD gives us much more information than we can get from existing experimental data. We thus have to

limit our comparison to few and simple processes. We choose the elementary proton–proton reactions as input channel and calculate 100 000 events for head-on collisions ($b = 0$ fm) for kinetic beam energies of 4, 6, . . . , 16 GeV.

3.2.1 Cross sections

We plot cross sections from experiments [46] together with the corresponding cross section determined from UrQMD simulations.

For the determination of inclusive cross section it is important to pay attention to the counting of particles in the UrQMD simulation, because even though the possibility of late absorption of particles is negligible for pp collisions, it becomes more important for heavy-ion reactions. Counting is different with respect to the lifetime of a particle. Particles with lifetimes longer than a few hundred fm/c are stable in UrQMD that aims at calculating dynamics in the hot and dense region up to times around 100 fm/c. Reference [40] gives an overview on the decays included in UrQMD.

Stable particles in the framework of UrQMD are counted at the end of the event calculation; this includes e.g. π , η and K mesons and Λ baryons.

Unstable particles are counted at the time UrQMD lets them decay into other particles. This does not include absorbed particles.

We determined exclusive cross sections in a different fashion. An example illustrates the procedure. Suppose we would like to determine the cross section for the exclusive reaction $pp \rightarrow pp\rho^0\pi^+\pi^-$. We would here set the ρ stable in UrQMD (i.e. it is not allowed to decay) and count reactions with the required final states $pp\rho^0\pi^+\pi^-$. We would then calculate the cross section with eq. (3.2) below. A problem may be that there is a non-vanishing probability for the ρ meson to be absorbed before the end of the calculation, e.g. via $\rho^0 p \rightarrow N^* \rightarrow p\pi^0$, letting the ρ meson disappear. This may occur at times much larger than the ρ meson lifetime. The ρ may also undergo elastic scattering with other particles and so change the reaction kinematics. However, in pp collisions the probability for secondary interactions (*final state interactions*) is supposed to be small, since the number of secondary particles is considerably smaller than in nucleus–nucleus collisions. They should not influence the obtained cross sections too much.

The cross section σ is then obtained from the average multiplicity

$$\langle M \rangle = N_{counted}/N_{events} \quad (3.1)$$

with

$$\sigma = \langle M \rangle \times \sigma_{tot} , \quad (3.2)$$

where for σ_{tot} we took the total cross section as provided by the UrQMD output `file16`.

We first compare the total, inelastic and elastic cross sections from UrQMD with data [46] in fig. 3.2. The total cross section is taken directly from the UrQMD output file; the elastic is from counting pp final states. The inelastic cross section is the difference $\sigma_{tot} - \sigma_{ela}$. Experimental data points for total and elastic cross sections are included in UrQMD; the calculations do indeed fit the experimental data. Compare also figures 3.1 and 3.2 in ref. [40].

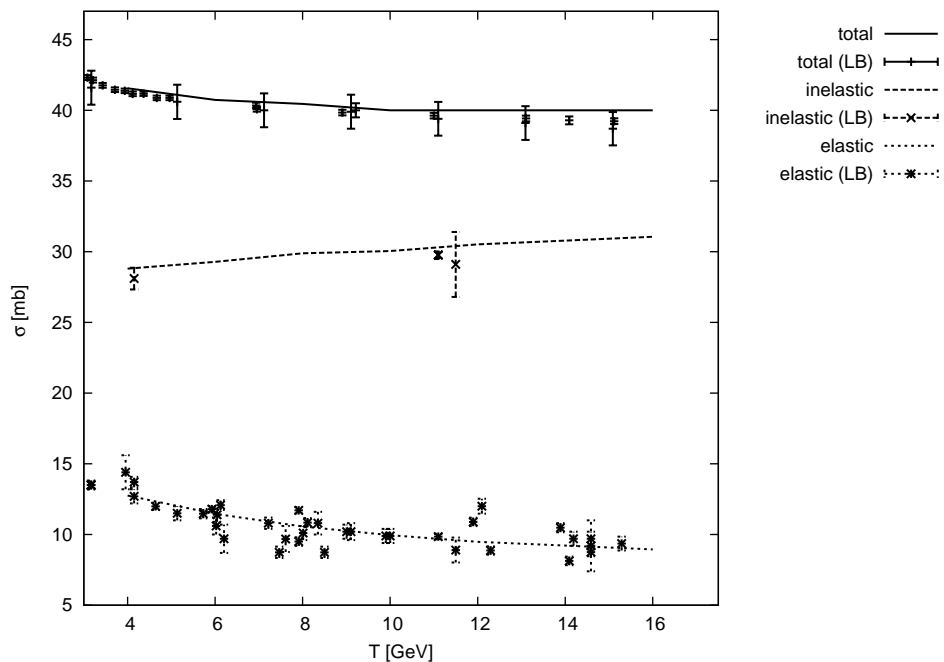


Figure 3.2: Total, inelastic and elastic cross section: Comparison of UrQMD predictions (curves) with measured data (symbols, LB) from the Landolt-Börnstein compilation [46].

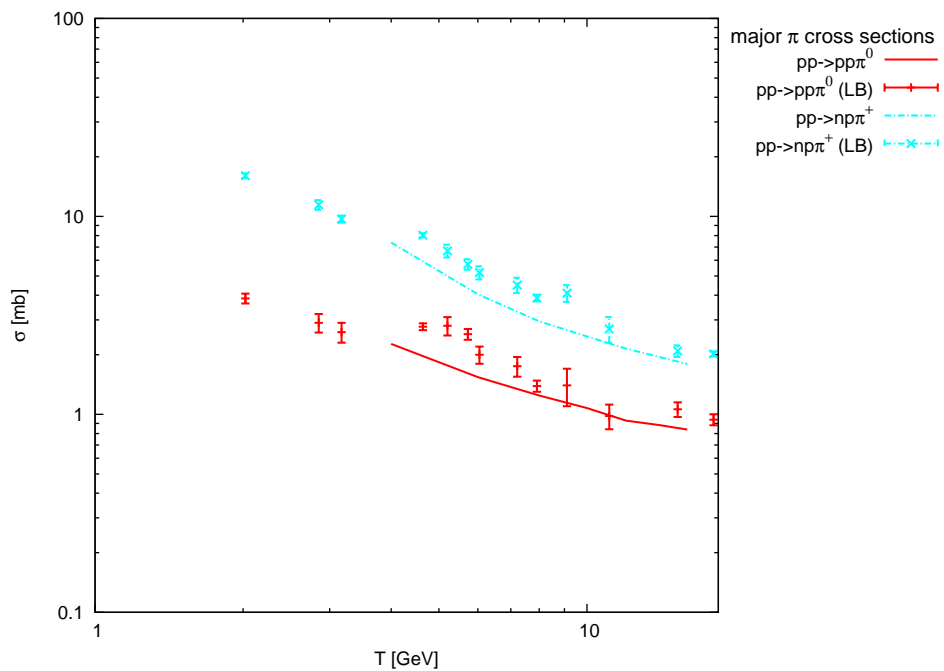


Figure 3.3: 1π exclusive cross sections. Notation as in fig. 3.2.

Next we compare different π production cross sections. We display three different plots: exclusive 1π production (fig. 3.3), inclusive 1π production (fig. 3.4) and exclusive 2π production (fig. 3.5). UrQMD does not include parametrisations for the exclusive π cross sections, but these are predictions of the model. One should note that this extensively measured processes provide sufficient data of sufficient quality to tune the model. We also display additional data for energies lower than 2 GeV and above 16 GeV; UrQMD reproduces the data in the range and follows the trend of the measured data. The same holds for the inclusive π

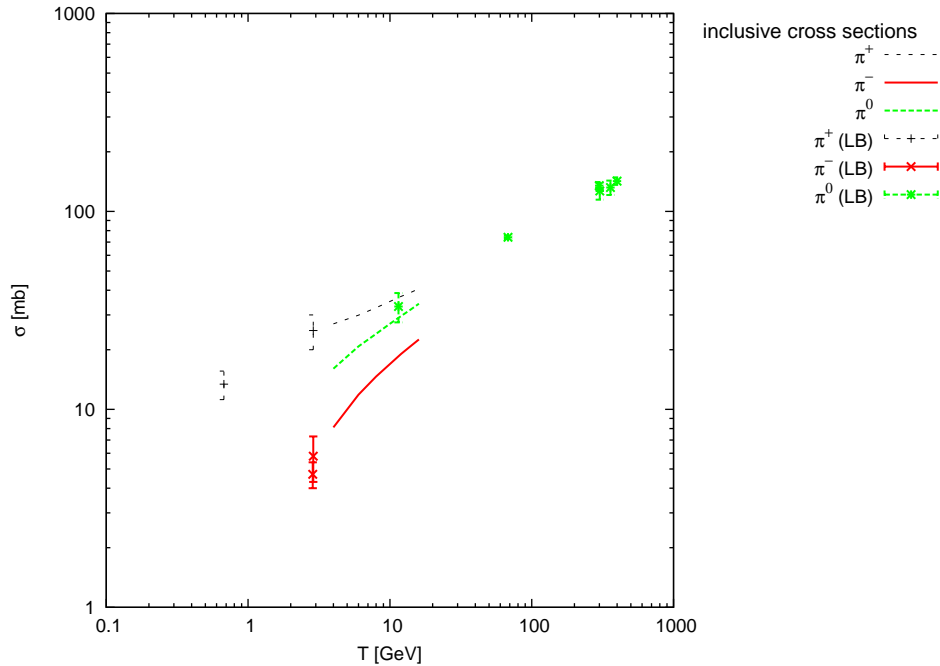


Figure 3.4: Inclusive π cross sections. Notation as in fig. 3.2.

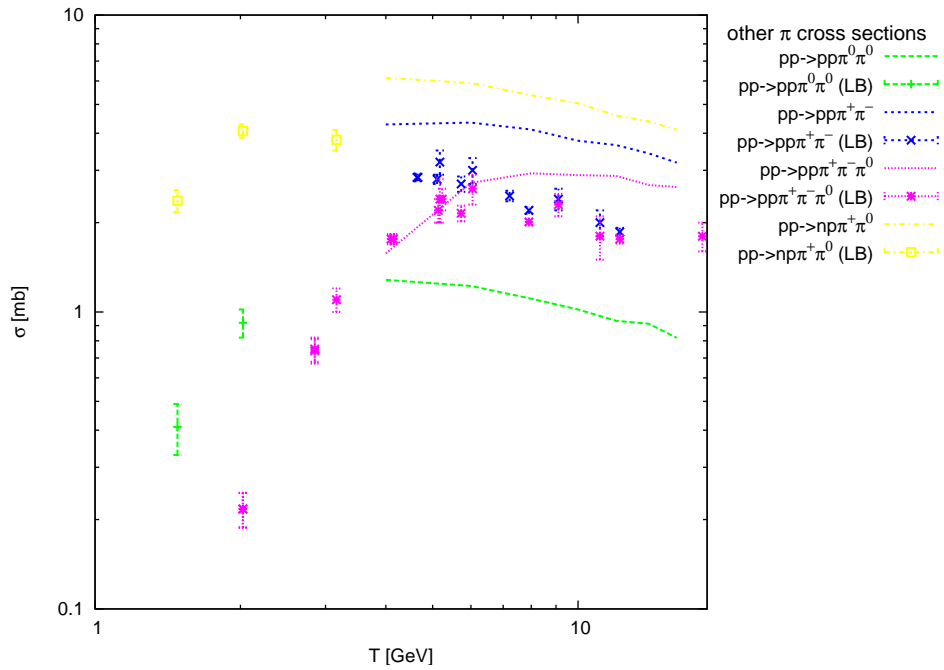
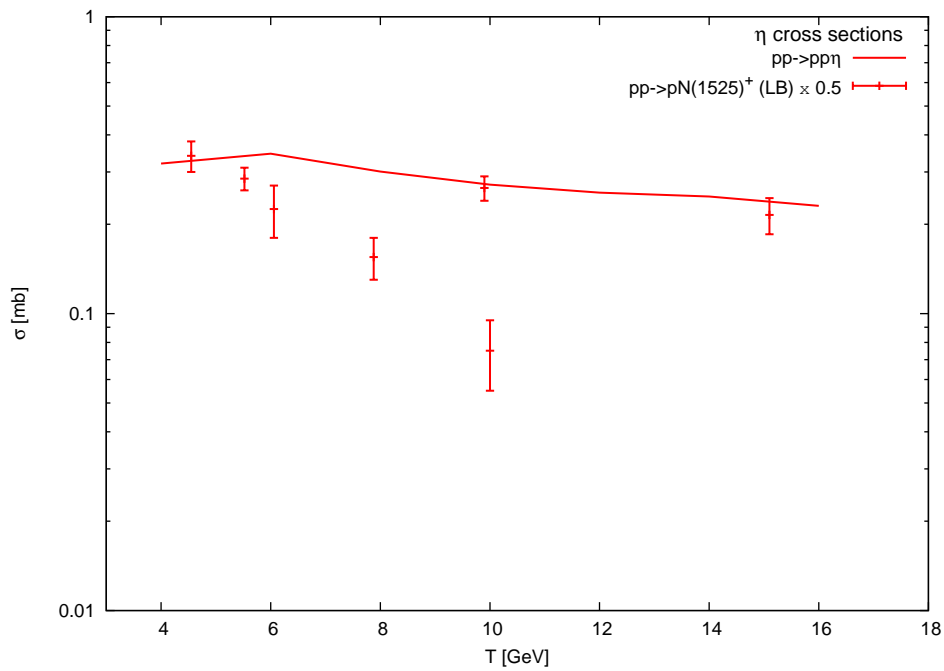
cross section. However, data in the considered region is sparse; again the UrQMD predictions and the available data are in good agreement.

Looking at the cross sections for multi- π production in fig. 3.5, data again is limited, but we are able to derive tendencies. The order of magnitude and the drop with rising beam energy are reasonably reproduced by simulation, but UrQMD seems to slightly overshoot the values found in experiment.⁶ Maybe our requirement for central collision favours string excitation too much, so that too many π mesons are produced. Nevertheless the simulated result is still reasonable.

We find the predicted η meson production cross section in good agreement with the data, cf. fig. 3.6. The data plotted is the scaled $pp \rightarrow pN(1525)^+$ cross section from [46]. [46] has no distinction between the $N(1520)^+$ and $N(1535)^+$ resonances listed in ref. [1], but summarizes both under $N(1525)^+$. Nevertheless, ref. [1] gives a branching ratio of 30 – 55% for $N(1535) \rightarrow N\eta$, thus scaling the tabulated cross section by a factor of 0.5 yields the plotted result. Since we scaled with the maximum possible branching ratio, UrQMD might overshoot the $pp \rightarrow pp\eta$ branching ratio by 60%.

Looking at the exclusive ω cross section (fig. 3.7) we observe an excellent fit of the

⁶Later (cf. page 34) we shall see that Δ production might be underestimated by UrQMD for pp systems, so the π overshoot should not be connected to Δ s.

Figure 3.5: multi- π exclusive cross sections. Notation as in fig. 3.2.Figure 3.6: Exclusive η cross sections. Notation as in fig. 3.2.

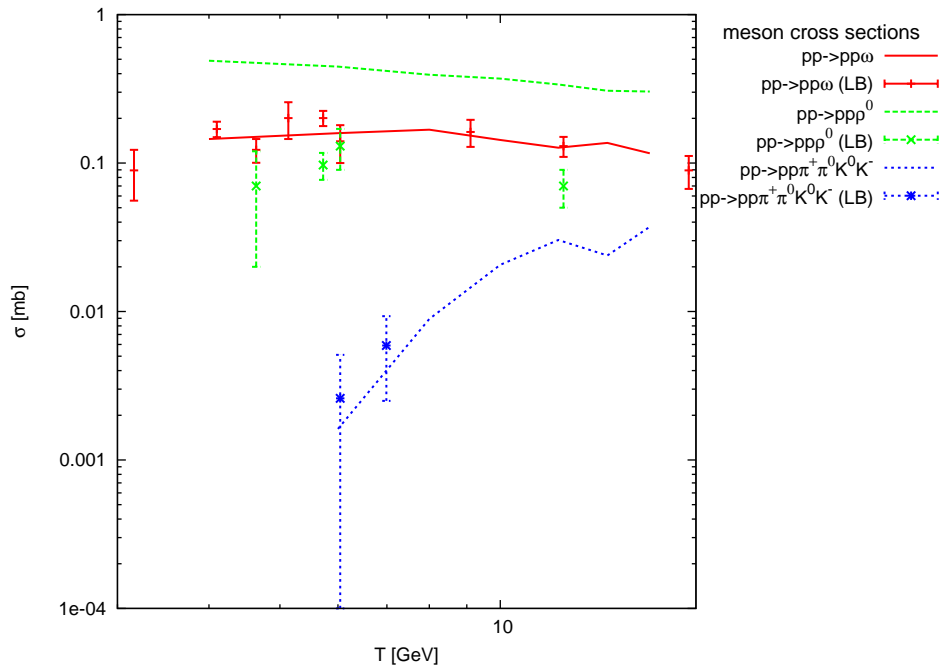


Figure 3.7: Exclusive ω , ρ^0 and K meson cross sections. Notation as in fig. 3.2.

simulation with the available data.

For exclusive ρ^0 production (fig. 3.7) UrQMD overshoots the experimental data. This needs to be taken into account when looking at multiplicity = 4 events (like $pp \rightarrow pp\rho^0 \rightarrow ppe^+e^-$). Looking at other exclusive ρ^0 channels we again find discrepancies, cf. fig. 3.8. However, the inclusive cross section is reproduced satisfyingly, see fig. 3.9.

For K production we plot a few data points for the exclusive channel $pp \rightarrow pp\pi^+\pi^0 K^0 K^-$ in fig. 3.7 and more points for inclusive production in fig. 3.9. The prediction is in good agreement with the measured data.

In fig. 3.9 we also plot the inclusive cross section for ϕ production, but unfortunately no measured data exists in the considered region.

A major source of pions in heavy-ion collisions are Δ baryon decays. Unfortunately there exists no measured data on the Δ baryon production cross section in proton-proton collisions in the region of interest.

Conclusion

UrQMD is able to reproduce the presented experimental cross sections in the right order of magnitude; only the calculated exclusive ρ^0 meson production cross section overshoots the measured cross section by a factor of four. Having this in mind, we will use UrQMD as event generator and proceed with an examination of m_t scaling behavior of UrQMD.

3.2.2 Transverse mass spectra

Next we present selected transverse mass spectra to compare properties predicted by fireball models (see section 1.1.1) with values from UrQMD. From fireball models we would anticipate similar particle abundances at a given transverse mass m_t for all particles from the collision.

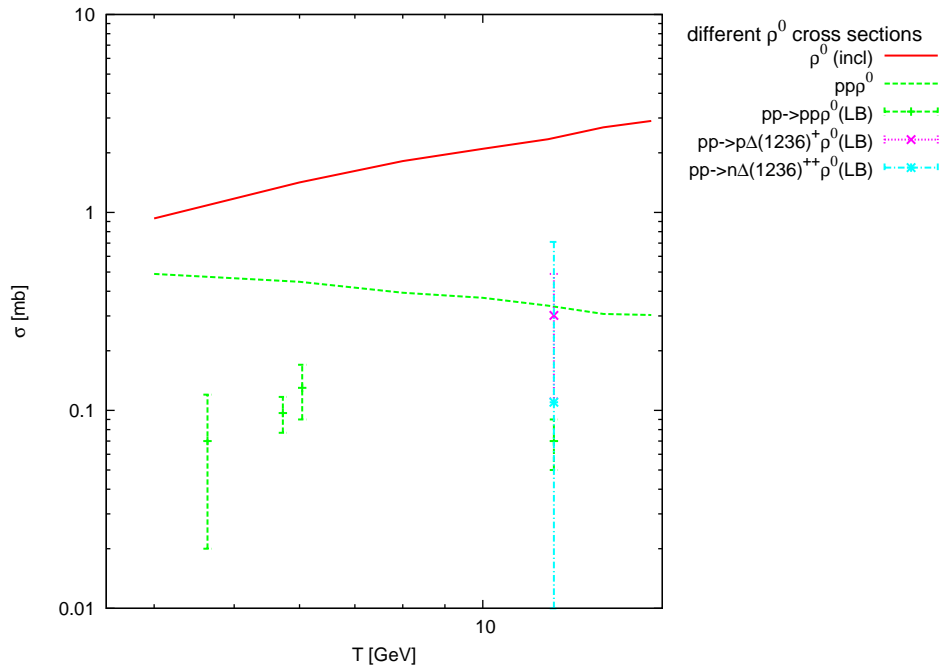


Figure 3.8: ρ^0 cross sections: UrQMD predictions and data [46]. The measured exclusive channels do not add up to the value predicted by UrQMD. Notation as in fig. 3.2.

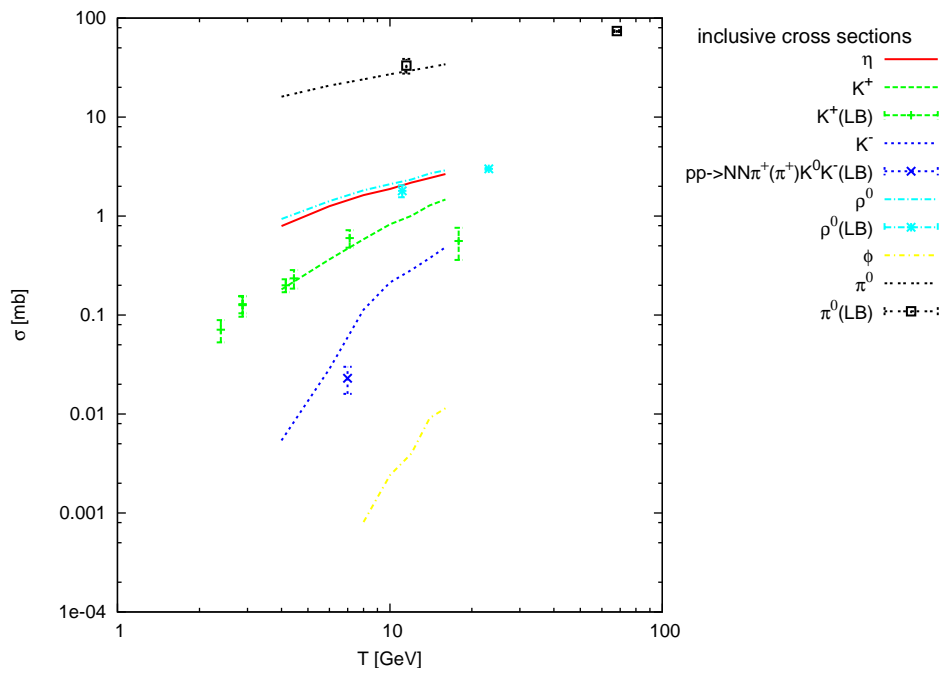


Figure 3.9: Inclusive meson cross sections: UrQMD predictions and data [46]. Notation as in fig. 3.2.

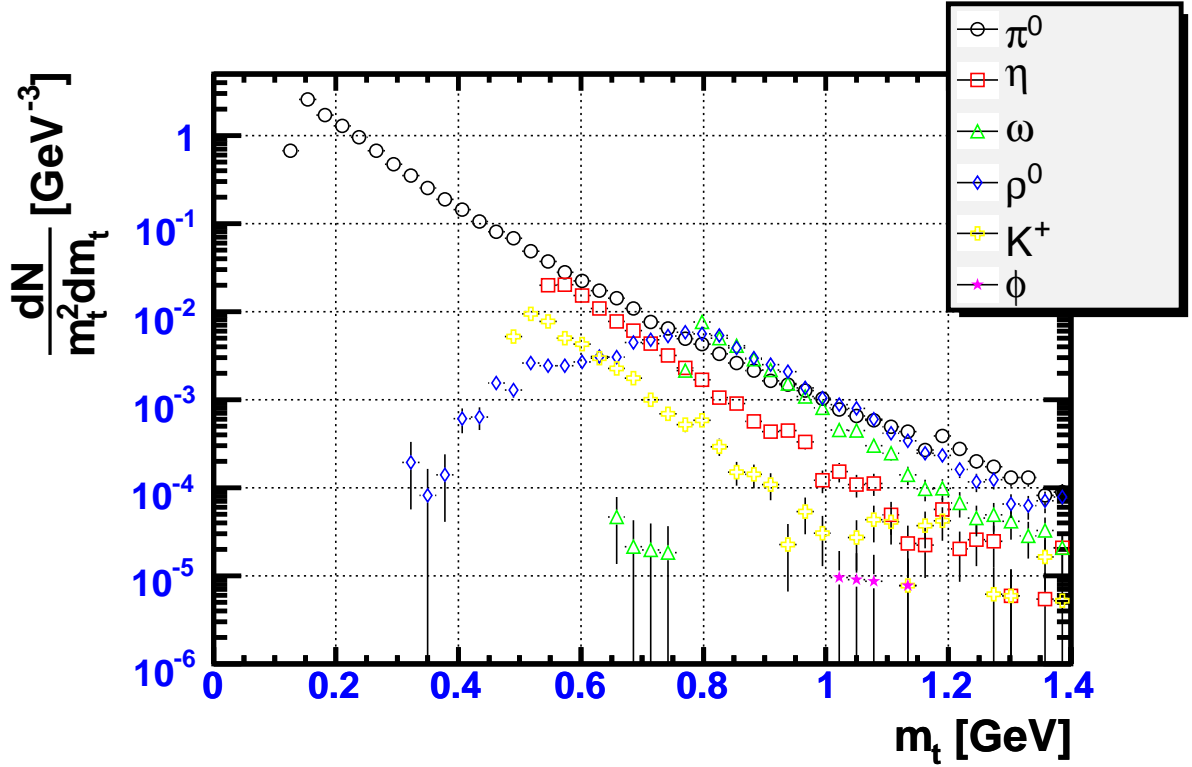


Figure 3.10: Transverse mass spectrum for various mesons produced in a pp collision at $T = 8$ GeV as predicted by UrQMD. The whole rapidity range is taken into account.

Moreover, if the different slope parameters of the transverse mass distributions agree, one could ascribe the system some equilibration features.⁷

We present results for proton–proton collisions at $T = 8$ GeV calculated from 100,000 events with an impact parameter $b = 0$ fm. Result for proton–neutron and neutron–neutron collisions are comparable. As for the calculations on page 26, properties of particles stable in UrQMD are taken from the end of the calculated event and of particles unstable in UrQMD from the instant of the decay. The yields for the different transverse mass bins are scaled by $1/m_t$ at the bin center [8].

Figure 3.10 shows the transverse mass spectra of different mesons. No cuts on rapidity are applied. For every particle we display the transverse mass as defined in eq. (1.1). We find similar slopes for η , ω , ρ^0 and K^+ mesons. The ϕ meson yield is lower by one order of magnitude than that of e.g. η mesons. The transverse mass distribution of π^0 mesons is not purely exponential and has a smaller slope parameter than that of other mesons, i.e. the relative number of π^0 mesons emitted with large transverse mass (i.e. large transverse momentum) is larger than for other mesons. The yields of η , ω and ρ^0 mesons at their respective pole mass is approximately the corresponding yield of π^0 mesons at the corresponding transverse mass. The yield for K^+ mesons at $m_t = m_{K^+}$ is about a factor 7–8 lower than the corresponding π^0 yield at the same transverse mass. However, an up-shift of the K^+ mass by an additional production threshold $m_\Lambda - m_N$, $m_t(K^+) = (p_t^2 + (m_K + m_\Lambda - m_N)^2)^{1/2}$ [39], would put the distribution of the K^+ on the order of magnitude of the η distribution.

⁷This effect may also just reflect the energy available for particle production [47].

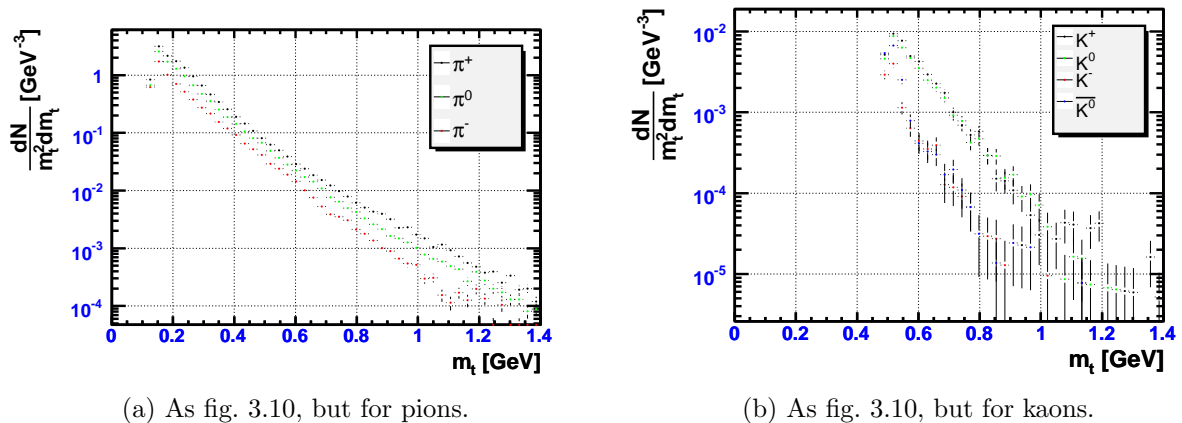


Figure 3.11: Transverse mass spectra.

Comparison of different charged pion transverse mass spectra in fig. 3.11a shows that regardless of the different charge the shapes are much alike, while the anticipated yields do not overlap. For all charges the feature of the two slope parameters corresponding to different production mechanisms for low and high m_t pions seems to be present. High m_t pions have a lower slope parameter and thus can be considered to be produced at a higher temperature.

In fig. 3.11b we show the transverse mass spectra for kaons. While the distributions overlap for K^+ and K^0 mesons, the anticipated yields of K^- and \bar{K}^0 mesons are lower by a factor of about 5. Still, away from $m_t = m_K$ the transverse mass distributions of all K mesons have approximately the same slope parameter. Shifting the mass of K^- and \bar{K}^0 mesons by a production threshold m_K due to associated production, $m_t(K^-, \bar{K}^0) = (p_t^2 + (2m_K)^2)^{1/2}$ [39] and for K^+ and K^0 as described above would put all kaon distributions on the same order of magnitude.

While in our simulation the yields of some particles at their respective pole mass show approximate m_t scaling, m_t scaling in general is violated due to the differing slopes of the m_t distributions. In contrast, the assumption of m_t scaling for all particles would lead to a much higher ϕ yield and possibly different acceptances for some particles due to a common slope of all transverse mass distributions, i.e. the particles would be emitted with different angular distributions. We do not find a m_t scaling behavior among the considered particle species for pp collisions at $T = 8$ GeV.

3.2.3 Particle yields: Comparison with other cocktails

At this point we are able to compare the particle multiplicities determined with UrQMD with other calculations. In the following, yields are the total yields in 4π ; no detector acceptance or efficiencies are taken into account.

The HADES group in Řež has calculated a cocktail for 39% most central carbon-carbon collisions at 8 AGeV [38]. The cocktail was modeled with multiple fireballs in Pluto [36]. The multiplicities of π^0 and η are from experimental data measured by the TAPS⁸ collaboration

⁸Two Arms Photon Spectrometer

[48], while for other sources m_t scaling was used. Note that a more recent version of the Rěz cocktail exists [49], but we refer to the results from ref. [38] for our comparisons since here conclusions are easier to draw.

Another calculation [50] of the anticipated dilepton yields at $T = 25$ AGeV has been prepared for the CBM experiment. For this calculation, the π^0 and η multiplicities are from an UrQMD calculation for gold–gold collisions, while the ρ^0 , ω and ϕ multiplicities are from HSDv2.4 calculations [51].

We compare these simulated data from both calculations with our UrQMD calculations, in which yields of dilepton sources have been determined from UrQMD calculations for both nucleon–nucleon and nucleus–nucleus (AuAu) systems. To examine possible isospin effects the elementary reactions have been calculated for isospin symmetric proton–proton and neutron–neutron and isospin asymmetric proton–neutron systems. All UrQMD calculations were done for central collisions only ($b = 0$ fm). In central collisions all nucleons may participate in the reaction; therefore, in central collisions particle yields will reach a maximum value. The yields were determined by the same method as described in section 3.2.1. The data presented was calculated from 10^5 UrQMD events for nucleon–nucleon systems and 10^3 UrQMD events for nucleus–nucleus systems.

Carbon–Carbon collisions at 8 AGeV

particle factor	Rěz [38]	UrQMD (this work)				
	CC	pp 8.56	pn 4.79	nn 8.47	CC, 40 $\frac{\text{fm}}{c}$	CC, 80 $\frac{\text{fm}}{c}$
π^0	7.05	0.82383 7.05	1.47093 7.05	0.83197 7.05	7.89	7.69
η	0.34	0.05613 0.48	0.11767 0.56	0.05485 0.47	0.53	0.47
ρ^0	0.36	0.04132 0.35	0.11149 0.53	0.04252 0.36	0.74	0.71
ω	1.49	0.02247 0.19	0.09418 0.45	0.02306 0.20	0.32	0.37
Δ^0	10.57	0.10700 0.92	0.18799 0.90	0.17662 1.50	3.02	2.93
ϕ	0.052	0.00001 0.00009	0.00067 0.003	0.00004 0.00034	0.002	0.003

Table 3.2: Hadron multiplicities for CC collisions at $T = 8$ AGeV of the Rěz group [38] are compared with UrQMD calculations at the same kinetic beam energy. The calculated yields in UrQMD NN collisions have been scaled by a quantity such, that the scaled π^0 yields overlap with the Rěz prediction respectively. For CC collisions in UrQMD, two different calculation times have been tested.

In tab. 3.2 and fig. 3.12 we compare the yields of dilepton sources of the Rěz group calculation [38] with different UrQMD predictions. In the table the extracted yield in nucleon–nucleon systems is shown with a scaled value to make nuclear effects visible. The individual scaling factors given in the table were chosen such that the π^0 yields overlap with the cocktail yield of the Rěz group.

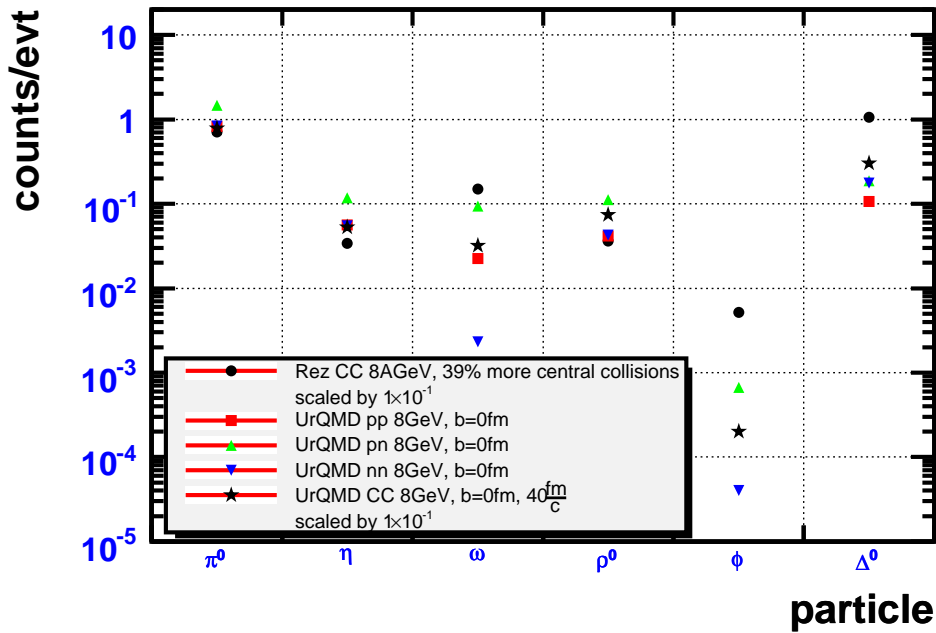


Figure 3.12: Hadron multiplicities at $T = 8$ AGeV, cf. tab. 3.2. The predicted yields by the Rěz group and from UrQMD (CC) have been scaled down by a factor of 10 to make common trends visible.

The determined η yield for the elementary input channels approximately scales to the order of the experimental value used by the Rěz group. Notably, the yield in the asymmetric system is larger than that in the symmetric. As expected for an isospin symmetric nucleus, the carbon–carbon yield is in the range of the mean of the scaled symmetric and asymmetric elementary yields. However, the UrQMD value is $\sim 60\%$ larger than the Rěz value. This might be due to our selection of central collisions only, or to an overestimation of the η multiplicity in UrQMD as mentioned on page 27 (cf. fig. 3.6).

The ρ^0 meson yield in nucleon–collisions in UrQMD roughly scales to the Rěz value, too. Again, the multiplicity is higher for the asymmetric elementary system. For carbon–carbon collision the yield is larger than the scaled elementary yields. This is a strong indication that ρ^0 production is realized as a soft secondary interaction in the UrQMD code.

The tendency for higher yields in asymmetric elementary input channels continues for ω mesons. However, in UrQMD the scaled values for nucleon–nucleon interactions are lower by a factor 3 to 7 than the corresponding Rěz yield. As for η production, the carbon–carbon value is approximately at the scaled mean value of symmetric and asymmetric reactions.

The scaled Δ^0 yields from UrQMD are lower by a factor of 10 with no indication of isospin dependencies. In UrQMD, Δ baryon production is primarily modeled via soft secondary interactions $N\pi \rightarrow \Delta$, so the necessary interaction rates will hardly be reached in elementary collisions. The value predicted for carbon–carbon collisions is a factor 3 larger than the scaled elementary, but still 3.5 times smaller than the value obtained from m_t scaling in the Rěz simulation.

The predicted values of ϕ meson yields from UrQMD are notably smaller than the m_t scaled values. The UrQMD prediction for carbon–carbon collisions is on the order of the

mean multiplicity for symmetric and asymmetric nucleon–nucleon collisions. Comparing the UrQMD value of carbon–carbon collisions with the scaled nucleon–nucleon values suggests that the scaling with respect to the π^0 yield may still hold; the striking discrepancy in the ϕ meson yield may be due to the violated m_t scaling in UrQMD – see also fig. 3.10 and the discussion on page 32.

To ensure the correct freeze-out of particle yields, we calculated the yields for the carbon–carbon system for two different time spans. A time of $80 \frac{\text{fm}}{c}$ was chosen as a reference system after freeze-out. Within the statistics used the yields are stable after $t = 40 \frac{\text{fm}}{c}$.

Figure 3.12 shows a graphical overview of the values discussed. Apparent differences between UrQMD and the m_t scaled cocktail can not be solved by simple scaling. The statistical errors of the determined yields are much smaller than the differences with the R ez cocktail.

Gold–Gold collisions at 25 AGeV

particle factor	CBM [50]	UrQMD (this work)				
	AuAu	pp 446.87	pn 407.08	nn 446.46	CC, $40 \frac{\text{fm}}{c}$ 28.04	AuAu, $40 \frac{\text{fm}}{c}$
π^0	365	0.81679 365	0.89663 365	0.81754 365	13.018 365	378.9
η	36	0.06911 30.9	0.07940 32.3	0.07109 31.7	1.045 29.3	34.4
ρ^0	23	0.10411 46.5	0.11421 46.5	0.10405 46.5	1.452 40.7	67.7
ω	38	0.08435 37.7	0.09243 37.6	0.08290 37.0	0.984 27.6	26.1
Δ^0					2.519 70.6	93.8
ϕ	1.28	0.00058 0.26	0.00075 0.31	0.00059 0.26	0.015 0.42	0.90

Table 3.3: Hadron multiplicities at $T = 25$ AGeV of the CBM collaboration [50] are compared with different UrQMD predictions at the same kinetic beam energy. For UrQMD NN and CC collisions the calculated yields have been scaled by a quantity such that the π^0 yields overlap with CBM prediction, respectively.

A set of analogous calculations has been performed for gold–gold collision at a kinetic beam energy of $T = 25$ AGeV. Again, we show UrQMD predictions of particle yields for nucleon–nucleon and nucleus–nucleus reactions in tab. 3.3 and fig. 3.13. The UrQMD yields in nucleon–nucleon and carbon–carbon collisions in the table have been scaled to the CBM cocktail’s π^0 yield; the data in the figure was now scaled down by a factor of 100 because of the higher multiplicities of the larger system.

While for nucleus–nucleus collisions the π^0 and η yields scale as before (cf. tabs. 3.3 and 3.2), the corresponding ρ^0 multiplicity from UrQMD now is a factor 2 larger than the value from the CBM calculations [50]. Again, the ρ^0 multiplicity in nucleus–nucleus interactions is substantially larger than that in elementary nucleon–nucleon interactions, hinting the importance of secondary interactions for ρ^0 production.

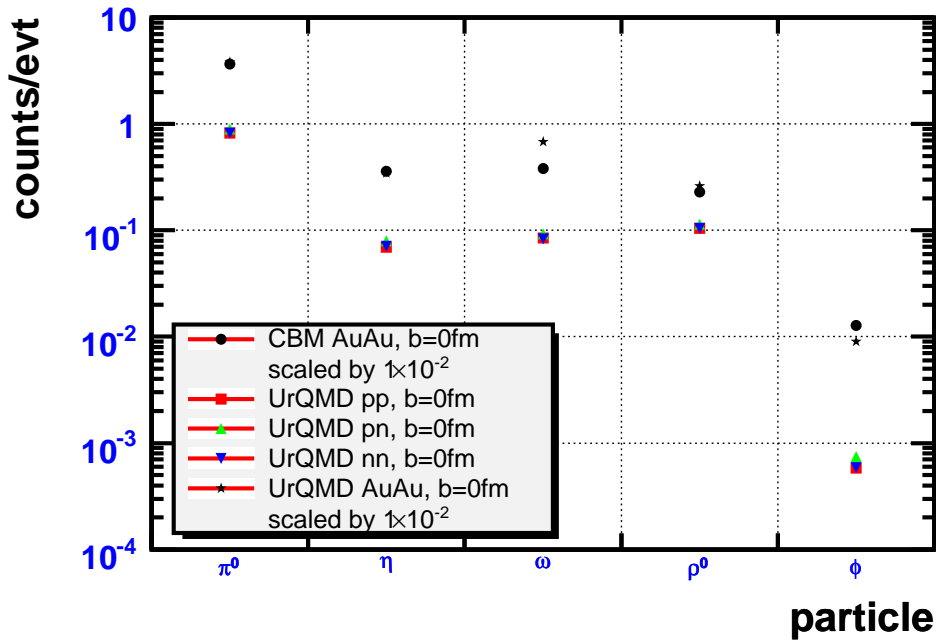


Figure 3.13: Hadron multiplicities at $T = 25$ AGeV, cf. tab. 3.3. The predicted yields of the CBM collaboration and UrQMD (AuAu) have been scaled down by a factor of 100 to make common trends visible.

The scaled nucleon–nucleon ω multiplicities correspond to the value obtained by ref. [50]. Surprisingly, the multiplicity in nucleus–nucleus collisions is smaller. If the production rate of the mesons per participating nucleon has been the same as in the nucleon–nucleon reactions, ω mesons must have been absorbed noticeably.

The multiplicities of ϕ mesons both in nucleon–nucleon as well as in CC/AA collisions in UrQMD are now roughly similar to multiplicities from ref.[50]. This may be expected, since we are now reasonably far above the production threshold energy for ϕ mesons. Again secondary interactions seem to be mainly responsible for the production.

3.2.4 Geometrical acceptances

Since the HADES setup has a hole in the forward direction at polar angle $\theta < 18^\circ$, one expects the absolute acceptance of the spectrometer to drop with rising beam energies. The accessible region is accordingly more and more limited to particles emitted in the backward hemisphere in the center of momentum system.

The crucial question is then if one is able to observe particles (or their decay products) from the mid-rapidity region. The rapidity y of a particle with energy E and longitudinal momentum p_z is defined as

$$y = \frac{1}{2} \ln \left(\frac{E + p_z}{E - p_z} \right) = \tanh^{-1} \left(\frac{p_z}{E} \right). \quad (3.3)$$

Since under a boost in the z -direction to a frame with velocity β , the rapidity gets $y \rightarrow y - \tanh^{-1} \beta$ [1], the rapidity is a convenient way to formulate relativistic problems. Consequently, mid-rapidity corresponds to the rapidity of the colliding system between projectile

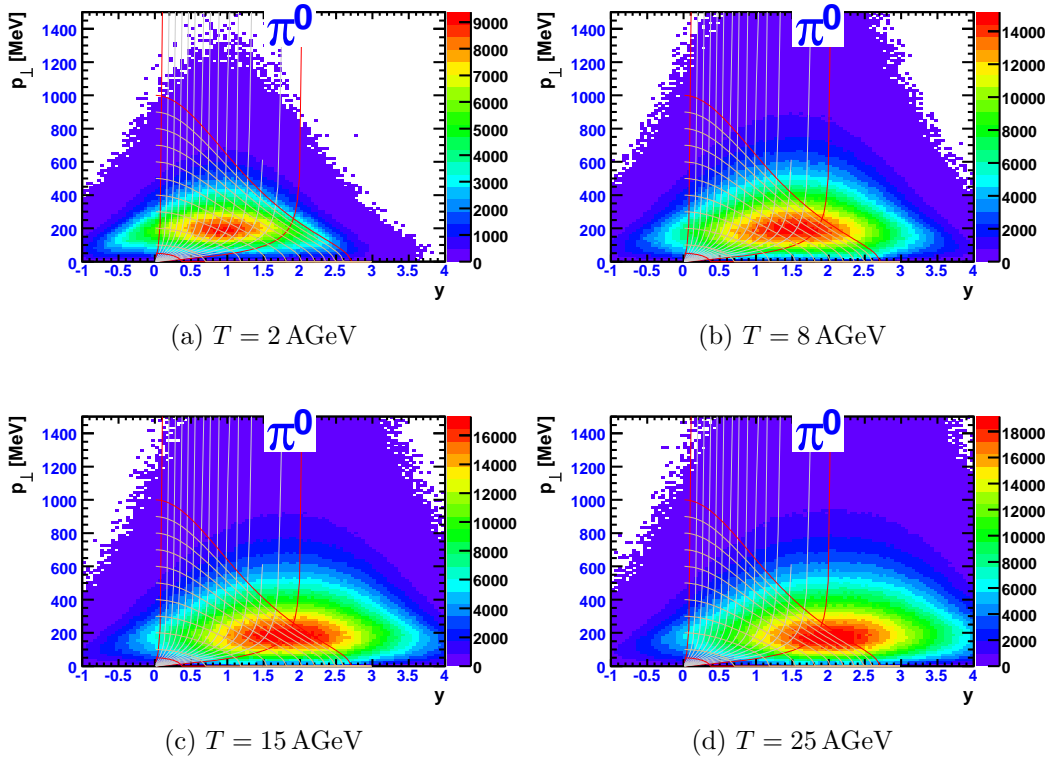


Figure 3.14: Phase space distributions of π^0 mesons for various beam energies in central CC collisions according to UrQMD calculations. On the z -axis $\frac{dN}{dp_{\perp}dy}$ is shown. The target rapidity is $y = 0$ and the projectile rapidities $y = 1.8, 2.9, 3.5, 4.0$ for the beam energies $T = 2, 8, 15, 25$ AGeV, respectively. The overlaid grid is described in the text.

and target rapidity; here highest nuclear densities are reached and nucleons are excited to hadronic resonances. Consequently, one expects secondary particles to be produced mainly at mid-rapidity. We show transverse momentum p_t versus laboratory system rapidities of particles as predicted by the UrQMD code for central carbon–carbon collisions. Later in section 4.1 we shall investigate rapidity distributions for the leptonic decay products and dielectrons in order to show how pair acceptances are affected by the limited detectors coverage. In case of Dalitz decays the undetected photon will always carry momentum of the mother particle that is not available for the pair.

All variables are the “true” values from the simulation – no “smearing” to account for a limited momentum resolution has been applied. We overlay the plots with a grid. Vertical lines correspond to constant angles from 85° (left) to 5° (right) with steps of 12° . Horizontal lines correspond to constant total momenta from 50 MeV (lower) to 1 GeV (upper) with steps of 95 MeV. Larger versions of these plots and more for other particle species can be found in figs. B.1, B.2, B.3 and B.4.

For π^0 mesons we find an almond-shaped p_t -vs.- y distributions (cf. fig. 3.14). Most of the particles are emitted from the mid-rapidity region; the ones for lower and higher rapidities are from decays in the projectile or target nucleus, respectively. For low beam momenta almost all particles (72%, cf. tab. 3.4) are emitted into the geometrical acceptance of the HADES setup, i.e. the mid-rapidity region is nearly fully covered. For higher beam momenta more and more particles are emitted at angles lower than 15° , thus being out

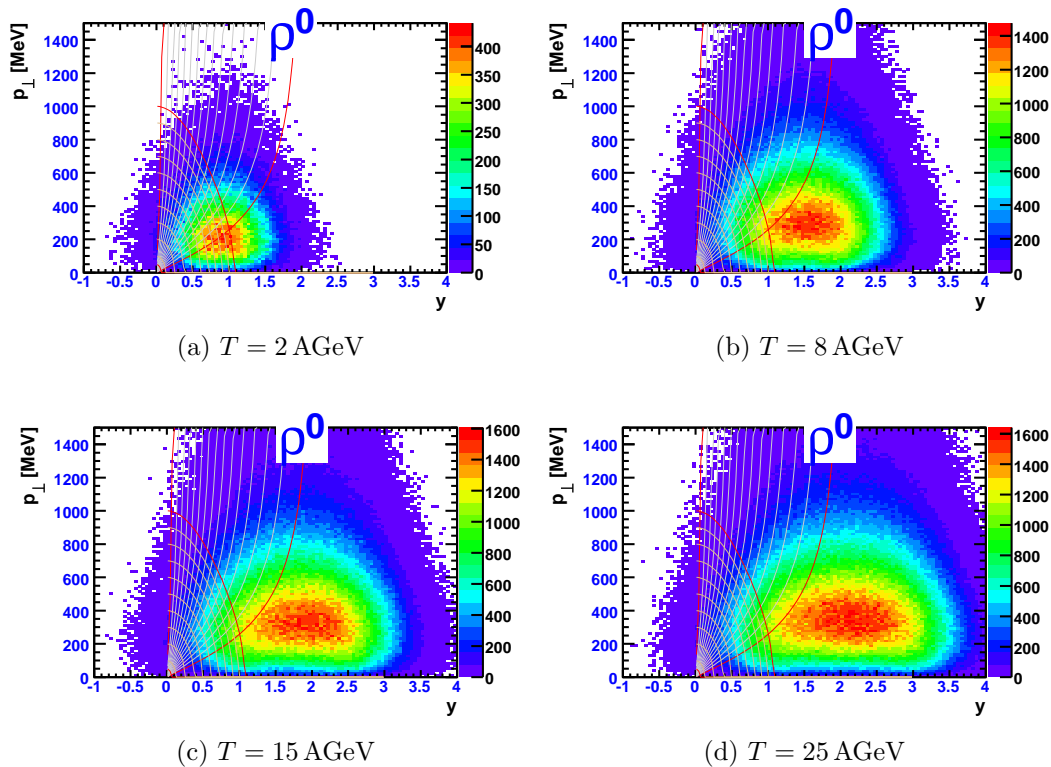


Figure 3.15: Phase space distributions of ρ^0 mesons. Notation as in fig. 3.14.

of the acceptance. The direct geometrical acceptance for π^0 mesons at a beam energy $T = 25$ AGeV is about 40%.

As secondary particles, ρ^0 mesons are mostly produced at mid-rapidity, but the rapidity distribution is narrower than for π^0 mesons (cf. fig. 3.15). While for a beam energy of $T = 2$ AGeV two third of all ρ^0 mesons are emitted into the geometrical acceptance of the spectrometer, this number quickly drops with increasing beam energies. For $T = 8$ AGeV the mid-rapidity region is still reached, but is only marginally accessible at higher momenta.

The production threshold of ϕ mesons in proton–proton collisions is $T \approx 2.6$ GeV. Nevertheless, UrQMD predicts their production in CC collision also at sub-threshold energies (cf. fig. 3.16a). We find that only a small part the of ϕ mesons phase space is directly

particle	T [GeV]	2	8	15	25
π^0		0.72	0.58	0.48	0.41
η		0.73	0.45	0.35	0.29
Δ^+		0.52	0.35	0.31	0.30
ω		0.65	0.37	0.30	0.24
ρ^0		0.64	0.40	0.31	0.26
ϕ		0.45 ± 0.16	0.31	0.21	0.17

Table 3.4: Geometrical acceptance for different particle species according to UrQMD. A particle is counted as accepted, if it is emitted from the target at polar angles $14^\circ < \theta < 85^\circ$. Statistical errors smaller than 1% are not shown.

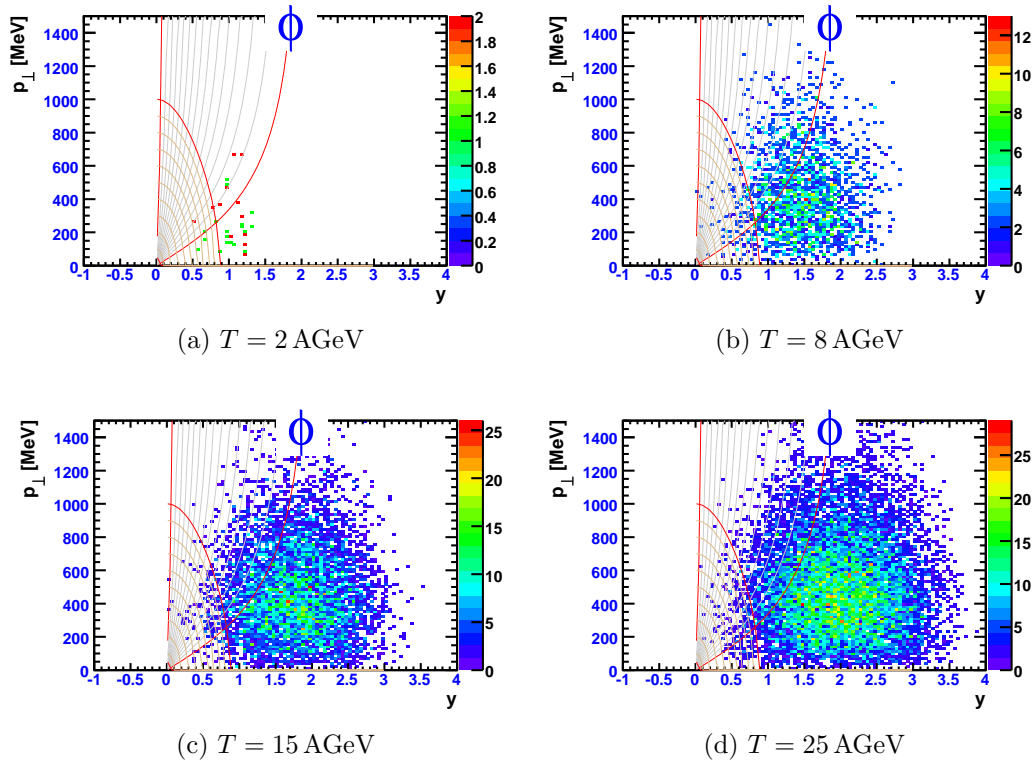


Figure 3.16: Phase space distributions of ϕ mesons. Notation as in fig. 3.14.

accessible with HADES. From fig. 3.16b we deduce that for beam energies $T > 8$ AGeV the mid-rapidity region is not directly accessible anymore.

Since HADES can not register charge-neutral particles, in a next step we have to analyze their decays, in particular direct decays into e^+e^- pairs.

3.3 Additional decays with Pluto

Because UrQMD does not calculate leptonic decays, we use the Pluto event generator [36, 37] to calculate the kinematic variables of decay products.

Pluto was designed to be fast and flexible. For hadronic decays, calculated spectral functions are used for sampling decay product variables. Dalitz decays are modeled with Vector-Meson Dominance. For unstable particles, Pluto calculates decay kinematics from mass-dependent Breit-Wigner resonance functions. Angular emission anisotropies of decay products can be set; however, we use only isotropic emission.

To enhance dileptonic decays, we scan the UrQMD output file for decays of the respective particles (UrQMD `processid -98`) and store the lines of these particles. After the event is read in, we choose from these one random particle and create a Pluto particle representation (a `PParticle` according to Pluto nomenclature) with the variables mass m , momentum \vec{p} , energy E and location \vec{r} in the laboratory system. We then use this `PParticle` to initialize a Pluto decay manager (`PDecayManager`). The first Pluto decay manager is set-up to process only the enhanced decays listed in tab. 3.1. We run one random decay set-up for this particle. The `PDecayManager` returns the momenta, energies, particle species and locations

of the decay products in the laboratory system. We add these particles to the event.

The decays of particles stable in UrQMD are calculated in with a second `PDecayManager`. Here, no particular decays are enhanced; the implemented decays are listed in tab. 3.1. Again, the decay products are appended to the event. The mother particle is removed.

Before proceeding to simulation results, we describe a schematic implementation of the detector resolution.

3.4 Limited detector resolution and multiple scattering

To account for limited detector resolution, we additionally “smear” the momentum and energy of all particles. The procedure we use is identical to the one used in the HAFT⁹ library [52]. Assuming Gaussian errors, a particle’s total momentum p_{tot} is smeared with a momentum dependent error. In the parametrization of the HADES momentum resolution by R. Schicker [53], the error of the particle’s reconstructed total momentum is

$$\frac{\sigma(p_{tot})}{p_{tot}} [\%] = 0.6 + 1.1 \cdot p_{tot} [\text{GeV}^{-1}]. \quad (3.4)$$

The errors of polar and azimuthal angle reconstruction [34] are

$$\sigma(\theta) = \sigma(\phi) = 0.18^\circ = 0.0031 \text{ rad}. \quad (3.5)$$

An additional error caused by multiple scattering [28] is

$$\sigma_{ms} = 13.6 \text{ MeV} \frac{\beta}{p_{tot}} \sqrt{\frac{x}{X_0}} \left(1 + 0.38 \log \left(\frac{x}{X_0} \right) \right), \quad (3.6)$$

with β and p_{tot} the velocity and total momentum of the particle respectively and a radiation thickness $x/X_0 = 0.02$. The additional logarithmic term and the value for x/X_0 are taken from the HAFT library. The total errors are then

$$\sigma_{ms}(\theta) = \sqrt{\sigma(\theta)^2 + \sigma_{ms}^2}, \quad \sigma_{ms}(\phi) = \sqrt{\sigma(\phi)^2 + \sigma_{ms}^2}. \quad (3.7)$$

Again assuming Gaussian errors, θ and ϕ angles are smeared with $\sigma_{ms}(\theta)$ and $\sigma_{ms}(\phi)$ respectively.

The total energy of the particle is then changed according to the smeared momentum and the particle’s mass.

The results of the smearing procedure are shown in figs. 3.17 and 3.17d. In fig. 3.17b we plot a fitted mean value of the relative difference of the original, true momentum and the smeared momentum. Apart from statistical fluctuations in high momentum bins the distribution is flat and essentially zero in a wide momentum range. The probability to measure a momentum higher than the real one is thus equal to that for measuring a lower one. This behavior corresponds to a symmetric distribution around the true momentum that we explicitly required with the Gaussian treatment of the error. For the standard deviation of the distribution of the relative momentum shift due to our smearing we obtain the linear momentum dependence of eq. (3.4). While in this approach, particles of small total momentum can in principle still be determined, fig. 3.17d shows how the particle

⁹Hades Acceptance Filter for Theorists

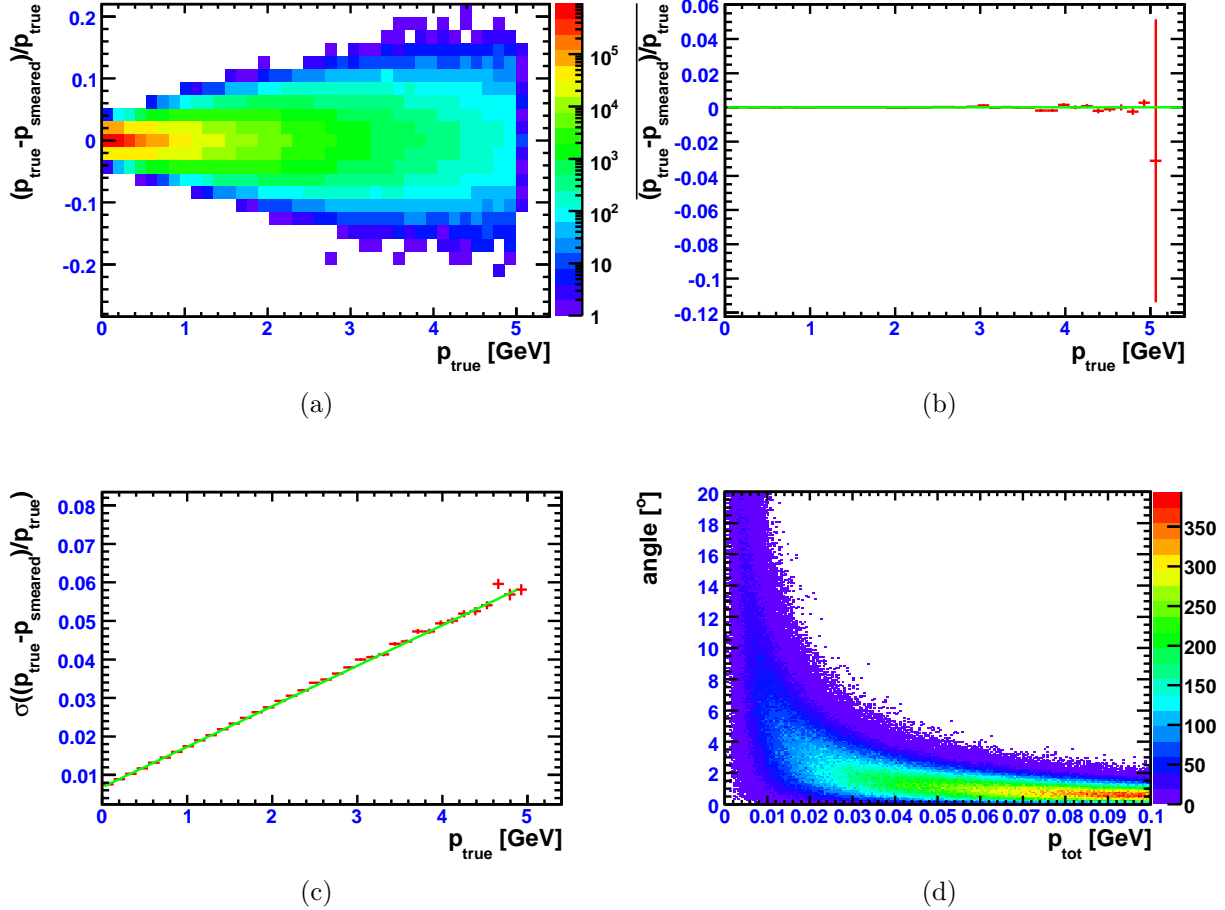


Figure 3.17: Smearing momenta of e^+ or e^- . Momenta $p_{\text{true}} > 5$ GeV are not shown due to limited statistics. (a) Distribution of momentum shift due to smearing for true momenta p_{true} . The momentum shift is normalized to the true momentum. Note the logarithmic z -axis. (b) Fitted mean value of the relative momentum shift due to limited detector resolution. The value zero is denoted by a green line. (c) Fitted standard deviation of the relative momentum shift. For a true momentum $p_{\text{true}} = 0$ GeV we can read off $\sigma = 0.6\%$ as anticipated from eq. (3.4). A first order polynomial fit to the data is shown. (d) Smearing angles of e^+ and e^- : Angle between true and recovered direction due to limited detector resolution and multiple scattering. For particle momenta smaller than 30 MeV the particle gets strongly scattered.

becomes subject to multiple scattering with dropping absolute momentum. For the desired extraction of invariant pair masses strong scattering of the particles will lead to fake results.

To make sure that variables calculated from (four)-momenta of particles are of high quality, particles with total momenta smaller than 50 MeV are rejected in the HADES analysis. Moreover, particles of very small momentum may bend in the magnetic field significantly, so that the tracking algorithms may not be able to successfully combine the detector hits of the particle to a track.¹⁰ Finally, particles of very small momenta may not even be able to leave the magnetic field, but “curl” between the MDC layers II and III. The influence of this cut on pair acceptances are shown in tab. 4.1. While pairs from π^0 Dalitz decays are reduced to about 50%, at maximum 30% of pairs from η and Δ^+ Dalitz decays are lost. The effect for pairs from ω Dalitz decays is even smaller. Electrons and positrons from the two-body decays of ω and ρ^0 mesons have such large momenta, that hardly any effect can be found. An e^+ or e^- from these sources may be rejected only if the determined momentum, here simulated with smearing, is far away from the true momentum (i.e. by a factor of 3 or more).

¹⁰The HADES analysis software scheme is sketched in Appendix A.

4 Results of the simulation

After examining UrQMD predictions of particle production cross sections for prominent dilepton sources and implementing dileptons in the UrQMD output of calculations for carbon-carbon collisions, we here present the results for a dilepton cocktail.

We show results for the single electrons and positrons first, followed by the results for pairs.

4.1 Rapidity distributions of single electrons and positrons

In section 3.2.4 we presented transverse momentum versus rapidity distributions for direct dilepton sources. The dilepton sources considered are π^0 , η , ω , ρ^0 and ϕ mesons and Δ^+ baryons. We also showed the angular acceptance for these particles and saw that most particles were emitted at low angles around forward direction. However, these particles are all unstable and the dilepton from their decays might be measured in the detector. The larger the mass of the decaying particle, the larger transverse momentum the light e^+ and e^- may acquire. Thus, they may very well be detected. We show distributions for single electrons and positrons from these dilepton sources (cf. figs. 4.1, 4.2, 4.3 below). We plot the true – i.e. unsmearred – variables from simulation and apply no cuts. Again we overlay the distributions with a p_{tot} - θ grid (cf. section 3.2.4).

For π^0 mesons displayed in fig. 4.1, both the rapidity and p_t distributions of the decay products are much broader than for the π^0 itself, as to be expected. For π^0 mesons, the p_t vs. y distribution peak around center-of-mass rapidity and $p_t = 200$ MeV (see fig. 3.14). In the three-body Dalitz decay $\pi^0 \rightarrow \gamma e^+ e^-$, the e^+ and e^- take only a small fraction of the meson's transverse momentum. Again we overlay the acceptance grid explained in section 3.2.4. Due to the vanishing electron/positron mass, electrons and positrons are emitted into the experiment's geometrical acceptance if they have transverse momenta larger than a few MeV, with no noticeable dependence on the lepton's rapidity, since for particles with momenta much larger than the particles mass m the rapidity y may be written as the pseudorapidity η (eq. (34.42) in ref. [1])

$$y \approx -\ln \tan(\theta/2) \equiv \eta \quad (4.1)$$

where θ is the polar angle of the direction of the particle's movement. However, leptons with rapidities $y > 2$ can not be measured as they are emitted at angles $\theta < 14^\circ$, as can be seen from the simulated phase space distributions.

For the phase space distribution of the decay products of the ρ^0 meson displayed in fig. 4.2, we again find a broadening of the rapidity distribution. Since here the decay

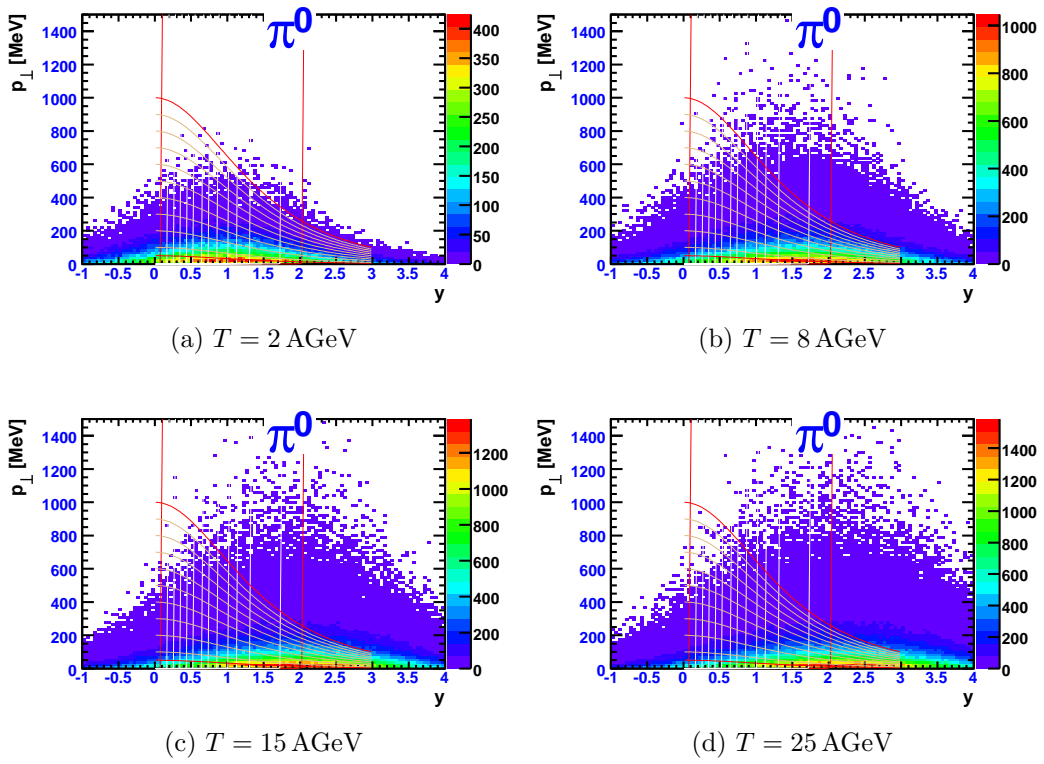


Figure 4.1: Phase space distributions of inclusive single electrons or positrons from $\pi^0 \rightarrow \gamma e^+ e^-$ decays in central CC collisions at various beam energies. The overlaid acceptance grid is explained in section 3.2.4.

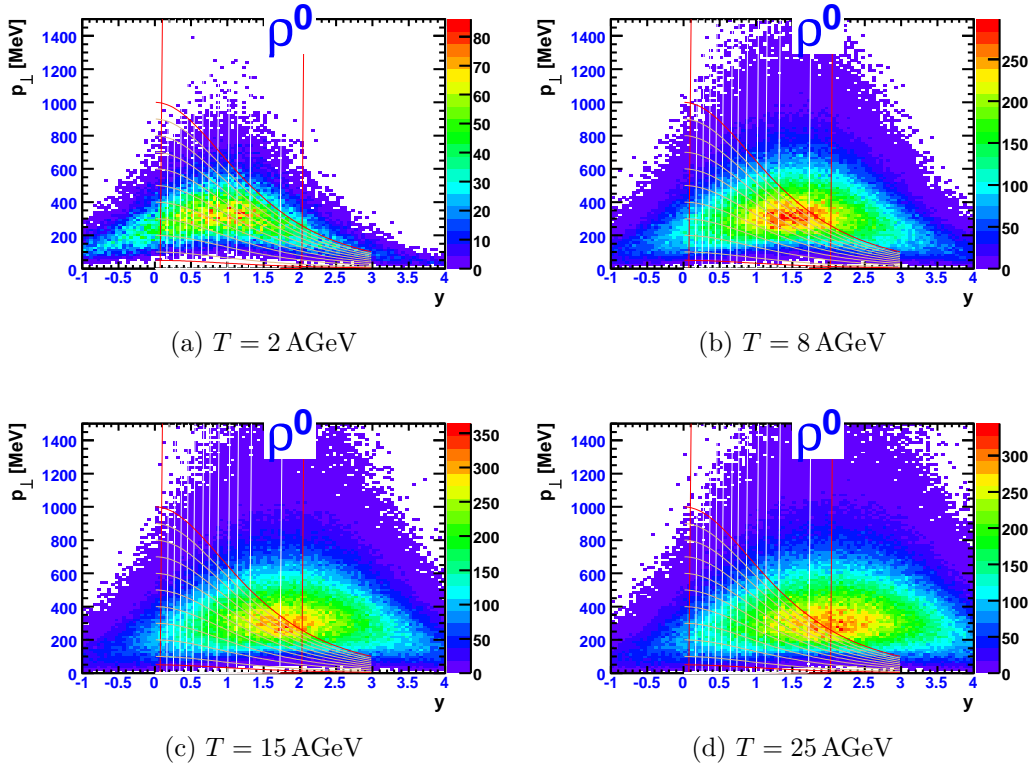


Figure 4.2: Inclusive single e^\pm from $\rho^0 \rightarrow e^+e^-$ decays. Notation as in fig. 4.1.

process is not a three-body decay as for π^0 mesons, but a two-body decay ($\rho^0 \rightarrow e^+e^-$), we find the genuine peak of the ρ^0 meson phase space distribution at mid-rapidity and $p_t \approx 300$ MeV in the lepton phase space distribution (cf. fig. 3.15). While inspection of the emission angles of the mother ρ^0 meson showed that only a tiny fraction would be emitted in the experiment's geometrical acceptance, the decay products pick up enough transverse momentum to be potentially detected. The experiment can also measure leptons from mid-rapidity. In principle, the same holds for leptons from the two-body decay of the ϕ meson $\phi \rightarrow e^+e^-$ (see fig. 4.3). However, the limited statistics of the calculated reactions allows a rough survey only. Again, the decay products take enough transverse momentum to be detected. While in fig. 3.16 we saw that only ϕ mesons with small rapidities were emitted directly into the HADES acceptance, the decay products make a wide rapidity range accessible. Investigation of the mid-rapidity region is practicable, while the highly populated peak-region of the phase space distribution is only cut to a small extent.

4.2 Results for pairs

In the following we present results for pairs of leptons. Unlike as in a real experiment, in simulation electrons and positrons literally carry a tag that indicates how they were produced. Combining pairs from the same mother particle poses no problem. Of course this information is not available in reality. Here, one carries out *all combinations* of electrons and positrons that pass the cuts. Fake pairs (wrong combinations) will contribute to the background – called combinatorial background –, while the true combinations constitute

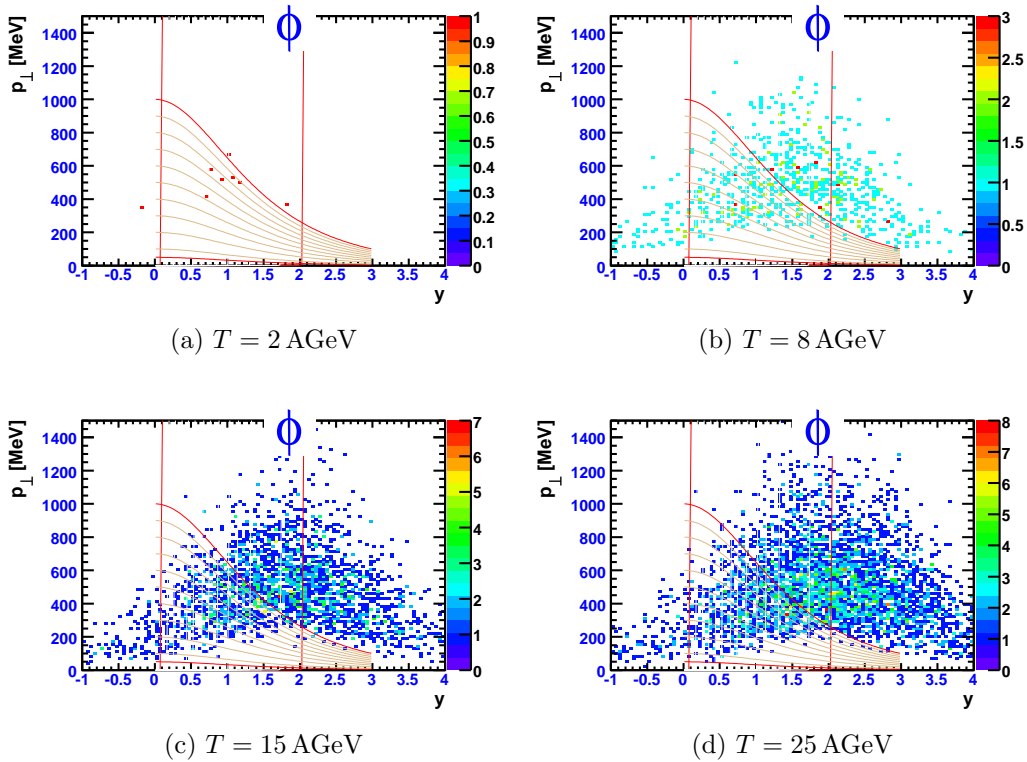


Figure 4.3: Inclusive single e^\pm from $\phi \rightarrow e^+e^-$ decays. Notation as in fig. 4.1.

the wanted signal. The decisive question is whether the signal is sufficiently distinct from the background for an analysis.

The amount of combinatorial background can be reduced by cuts that reduce contributions of electrons and positrons from background processes. These cuts act before the analysis. One of such cuts is examined in section 4.2.1. Another way to increase the signal-to-background ratio is to estimate the background contribution and then subtract it from the spectra. In section 4.2.4 the results of such a method are cross-checked with distributions known from simulation.

4.2.1 Quality cuts

For energies up to $T = 3.5$ AGeV it was demonstrated that electron–positron pairs from photon conversion in the target or the RICH detector have small opening angles [43]. Removing both the electron and positron of pairs with opening angles smaller than 9° from the analysis (not using them for any pairing) is the central mean of reducing the combinatorial background.

Using the same conversion code as in the above analysis of ref. [43], we show that an opening angle cut of 9° is also suitable for a higher energy of $T = 8$ AGeV.¹ In section 3.4 we showed how multiple scattering and a limited detector resolution influence the measured direction of a particle track. Accordingly, measured pair opening angles differ from the true angles. We expect this to be important for particles of very small momenta (cf. fig. 3.17d).

¹One can also show that this cut yields good results for even higher energies.

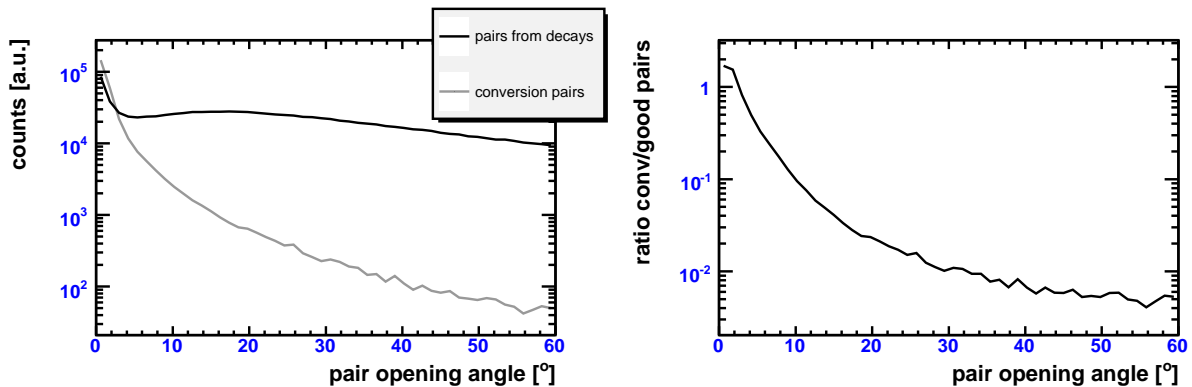


Figure 4.4: Left: Opening angle distributions for electron–positron pairs from particle decays (black) and photon conversion (grey) for small opening angles. The decays included are $\pi^0 \rightarrow \gamma e^+ e^-$, $\eta \rightarrow \gamma e^+ e^-$, $\Delta^+ \rightarrow p e^+ e^-$, $\omega \rightarrow \gamma e^+ e^-$, $\omega \rightarrow e^+ e^-$, $\rho^0 \rightarrow e^+ e^-$ and $\phi \rightarrow e^+ e^-$ (cf. tab. 3.1). The momenta of the individual particles have been smeared as described in section 3.4. Right: Ratio of the yields of conversion pairs and pairs from decays for a given smeared pair opening angle.

However, since in the HADES analysis particles with momenta smaller than 50 MeV are rejected, the reconstructed pair opening angles can be expected to be close to the true angles. For the calculation of the opening angle, we use the smeared momenta only. Only true pairs with both partners emitted inside the detector’s geometrical acceptance and individual momenta $p > 50$ MeV are taken into account. In fig. 4.4a we display the opening angle distributions for pairs from particle decays and from conversion. Notably, the opening angle distribution of conversion pairs peaks at small angles and drops quickly. For pairs from particle decays (cf. tab. 3.1) we also find a peak at small angles, but the distribution does not drop to zero. For angles $> 10^\circ$ the opening angle distribution stays constant in the considered range. In fig. 4.4b we display the ratio of the yield of conversion pairs and decay pairs for a given opening angle. For a pair opening angle of 9° we find a ratio of conversion pairs to decay pairs of about 1 : 10.

With applying an opening angle cut of 9° on the reconstructed pairs and rejecting all electrons and positrons of these pairs from the analysis, the amount of electrons and positrons from photon conversion can clearly be reduced. They do not contribute to the combinatorial background in our simulations. The reduction of true pairs in the $\rho - \omega$ mass region due to this cut is smaller than 5%, cf. tab. 4.1.

4.2.2 Cocktail composition

In section 3.1 we motivated why we would implant enhanced dileptonic decays in every second event only. The main concern at that point was to guarantee that particle multiplicities are reproduced correctly. We now examine how our enhancement procedure and the subsequent scaling with respect to the correct event weight affects the invariant mass spectrum of combinatorial background. The invariant mass m of a pair of particles is defined as

$$p^\mu p_\mu = (E_1 + E_2)^2 - \sum_{i=1}^3 (p_{i,1} + p_{i,2})^2 \equiv m^2, \quad (4.2)$$

T [GeV]	2			8			15			25		
	geo.	p	9°									
π^0	0.66	0.38	0.05	0.56	0.33	0.05	0.48	0.29	0.04	0.41	0.25	0.04
η	0.64	0.53	0.19	0.56	0.45	0.14	0.51	0.42	0.12	0.43	0.35	0.09
Δ^+	0.64	0.51	0.16	0.53	0.42	0.11	0.45	0.35	0.10	0.41	0.32	0.09
ω	0.54	0.54	0.54	0.40	0.40	0.40	0.31	0.31	0.30	0.26	0.26	0.25
ω_{Dalitz}	0.67	0.58	0.20	0.58	0.51	0.16	0.48	0.43	0.13	0.41	0.37	0.11
ρ^0	0.56	0.56	0.56	0.40	0.40	0.39	0.31	0.31	0.31	0.26	0.26	0.25
ϕ	0.75	0.75	0.75	0.43	0.43	0.42	0.32	0.32	0.31	0.26	0.26	0.25
CB	0.59	0.28	0.04	0.43	0.23	0.02	0.32	0.17	0.02	0.24	0.13	0.01

Table 4.1: Acceptance for dielectron from particle decays in central carbon–carbon collisions and the combinatorial background (CB) at different beam energies. We show the fraction of implanted pairs left after cutting on (1) both particles emitted inside the detector’s geometrical acceptance, (2) a cut on the minimal smeared momentum of the e^+ and e^- in the pair and (3) after exclusion of e^+ and e^- that were found in pairs with opening angles $\alpha < 9^\circ$. Angles are calculated for smeared momenta.

where E_1 and E_2 are the energies of the particles and $p_{i,1}$ and $p_{i,2}$ are the x , y and z components of the respective particle momenta.

In fig. 4.5 we present preliminary invariant mass spectra for the unchanged and the enhanced cocktail separately; the final spectrum has to be combined from both. In the enhanced cocktail we find the expected artificial suppression of dileptons from π^0 and η decays, while in the unchanged cocktail, where all events have the same weight, we obtain realistic multiplicities. In the enhanced cocktail we artificially require π^0 or η decays to occur together with dileptonic decays of the enhanced sources (Δ^+ , ω , ρ^0 , ϕ). These events are rare and thus carry small weights in our simulation. In the enhanced cocktail the role of electrons and positrons from π^0 and η decays is mainly that these leptons yield more possible pairing combinations which may contribute to the combinatorial background. We also find fluctuations in the invariant mass spectra of pairs from π^0 and η decays and the combinatorial background for the enhanced cocktail. These fluctuations occur, because events producing these leptons a priori have no fixed weight. Since the statistics in the respective channels might be different, one single process with a high weight can stick out of the smooth spectrum. All of the spikes in the π^0 , η and combinatorial background spectra in fig. 4.5b are due to singular events with weight 1. There, no enhanced decays were implanted, because none of the sources Δ^+ , ω , ρ^0 or ϕ was produced in the event.

For the combinatorial background we find a peculiar step in the invariant mass distribution at $m \approx 300$ MeV. This step again is an artifact of our enhancement procedure. While the high-mass part is the combinatorial background from events with enhanced dilepton decays (small weight), the low-mass part arises from events with no enhanced process implemented (e.g. an e^+ from a π^0 decay and an e^- from photon conversion; large weight). Comparison between the combinatorial background in the unchanged and the enhanced cocktail shows that for small invariant pair masses the combinatorial background is dominated by the frequent sources (π^0 and η decays, photon conversion). For invariant pair masses $m > 700$ MeV not enough unchanged events have been calculated to obtain a spectrum for the full invariant mass range. However, if we assume that the invariant mass

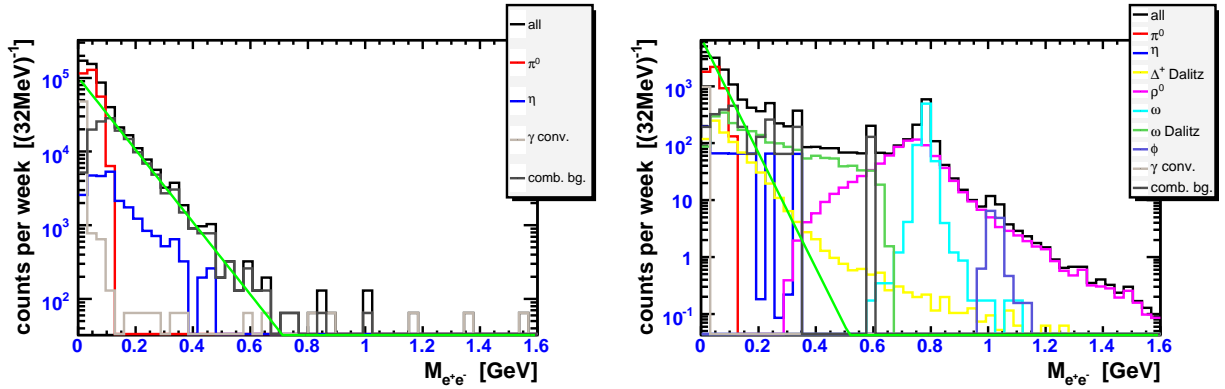


Figure 4.5: Preliminary invariant mass spectra of an unchanged (left) and enhanced cocktail (right) for central CC collisions at $T = 8$ AGeV. A cut on minimal momenta of e^+ and e^- $p > 50$ MeV is applied. Only e^+ and e^- inside the geometrical HADES acceptance and from pairs with opening angles $\alpha > 9^\circ$ are taken into account. The cuts are explained in sections 3.4 and 4.2.1, respectively. Momenta have been smeared. The π^0 , η and combinatorial background channels in the enhanced cocktail (right) are found to be artificially suppressed.

of pairs from the combinatorial background follows an exponential distribution for masses $m > 200$ MeV, we can extrapolate into the high-mass region. In the following we do not use enhanced events to estimate the combinatorial background anymore – the combinatorial background will be estimated from the unchanged events only.

4.2.3 Rapidity distributions

In fig. 4.6 we show rapidity distributions of dielectrons, where both leptons are from the same mother particle. An integration over the whole transverse momentum range of the pair is applied. We show both the spectrum for pairs in 4π and in HADES's geometrical acceptance after a cut on a minimal momentum $p > 50$ MeV and with a pair opening angle cut $\alpha > 9^\circ$ (cf. section 4.2.1). Each spectrum is shown for three invariant mass regions: below π mass $m < 150$ MeV, in the η mass region $150 \text{ MeV} < m < 550$ MeV and above $m > 550$ MeV, where the invariant mass of a pair is defined as in eq. (4.2) Accordingly, the rapidity of a pair is

$$y_{e^+e^-} = \frac{1}{2} \ln \left(\frac{(E_{e^+} + E_{e^-}) + (p_{z,e^+} + p_{z,e^-})}{(E_{e^+} + E_{e^-}) - (p_{z,e^+} + p_{z,e^-})} \right). \quad (4.3)$$

In 4π we obtain essentially Gaussian rapidity distributions centered around center-of-mass rapidity as expected. The widths of the rapidity distributions are smaller for smaller invariant pair mass. However, with growing beam energy, the distributions gradually become more similar.

In the experiment's geometrical acceptance and after the cuts the rapidity distributions of pairs with invariant masses $m < 150$ MeV can still be described by Gaussian distributions, but we find asymmetries. For pairs with higher invariant masses the rapidity distributions are deformed and not Gaussian any more. Notably is the shift of the centroid of the distributions to higher rapidities. For rapidities larger than the center-of-mass rapidity the width of the distributions is slightly larger than that for rapidities smaller than mid-rapidity.

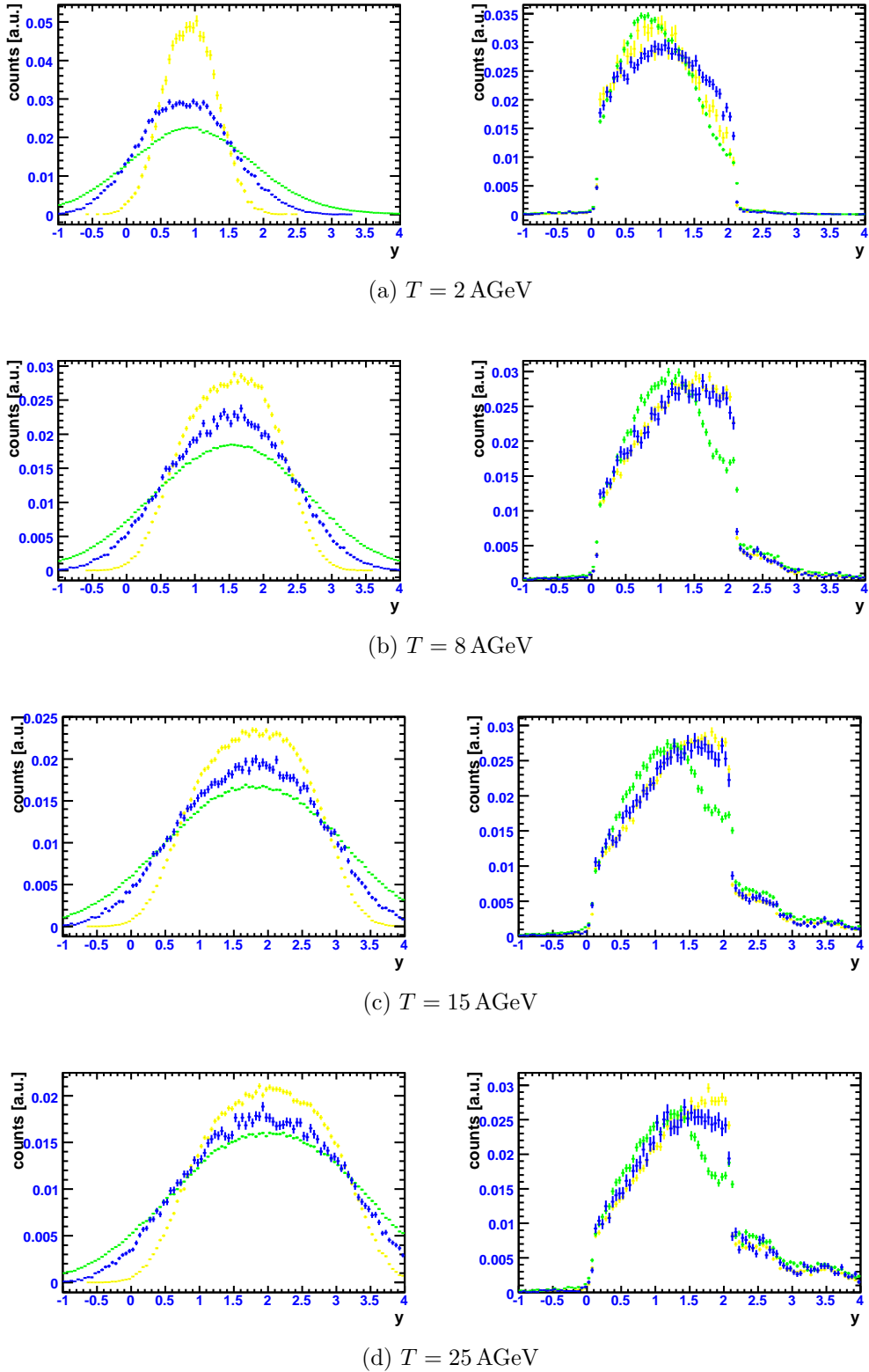


Figure 4.6: Rapidity distributions of dielectrons from particle decays from central CC collisions at various energies. Three invariant mass regions are shown: π mass region $m < 150 \text{ MeV}$ (green), η mass region $150 \text{ MeV} < m < 550 \text{ MeV}$ (yellow) and $m > 550 \text{ MeV}$ (blue). The whole transverse momentum region of the pair is taken into account. The distributions are normalized to unity. The left column is for 4π acceptance, while the right column is for pairs of e^+ and e^- in the geometrical acceptance of HADES with momenta $p > 50 \text{ MeV}$ and after and opening angle cut (see section 4.2.1).

For every beam energy the distributions are still centered around a common rapidity. At a beam energy $T = 2$ AGeV the mean of the distributions in acceptance and after cuts is the center-of-mass rapidity, while for higher energy the distributions in acceptance and after cuts are centered around a common rapidity $y = 1.5$, which is smaller than the respective center-of-mass rapidity.

4.2.4 Combinatorial background and like-sign method

In tab. 4.1 we showed how cuts on the minimal momentum of the e^+ and e^- and selection of pair opening angles $\alpha > 9^\circ$ can reduce the combinatorial background. For a further estimation of the combinatorial background the like-sign method can be used [28]. Here, one creates pairs of the same-charge sign leptons in the event, which have to pass the same cuts as the signal pairs. The combinatorial background can then be obtained from the geometric mean of the like-sign spectra

$$N_{CB} = 2\sqrt{N^{++}N^{--}}, \quad (4.4)$$

where N_{CB} is the yield from the combinatorial background in a certain invariant mass bin and N^{++} (N^{--}) is the number of counts from the positive (negative) charged pair of like-sign leptons in the same invariant mass bin. Usually, the calculated combinatorial background can then be subtracted from the measured spectra to obtain the “signal”.

In fig. 4.7 we show a comparison of the combinatorial background as obtained from the simulated cocktail and the like-sign method. As pointed out in section 4.2.2 not enough statistics is available for higher pair masses, so only invariant pair masses $m < 400$ MeV are shown. We find the both spectra in good agreement; the difference is 10 counts or lower at any energy. This comes as no surprise, since we assumed the same acceptance for electrons and positrons. The like-sign method is a good estimate of the combinatorial background for masses $m < 400$ MeV in our cocktail. More elaborated simulations which take into account acceptances for particles have to be undertaken to reach more realistic results.

For a HADES analysis of carbon–carbon collisions at a beam energy $T = 2$ AGeV event-mixing techniques were used to evaluate the combinatorial background for masses $m > 400$ MeV.

4.2.5 Invariant mass spectra

In fig. 4.8 we present invariant dilepton mass spectra for carbon–carbon collisions at different beam energies after one week of beamtime at the FAIR facility. The number of interactions has been calculated in the following way. The interaction rate is

$$\frac{dN}{dt} = \mathcal{L}\sigma, \quad (4.5)$$

where \mathcal{L} is the luminosity and σ the total cross section. The luminosity can be calculated from the average beam intensity $I = 1 \times 10^8 \text{ s}^{-1}$, the size of the beam spot $A = 3 \text{ mm}^2$ [18] and the number of target nuclei n in the cylinder of length l and base area A traversed by the beam

$$\mathcal{L} = I \frac{n}{A}. \quad (4.6)$$

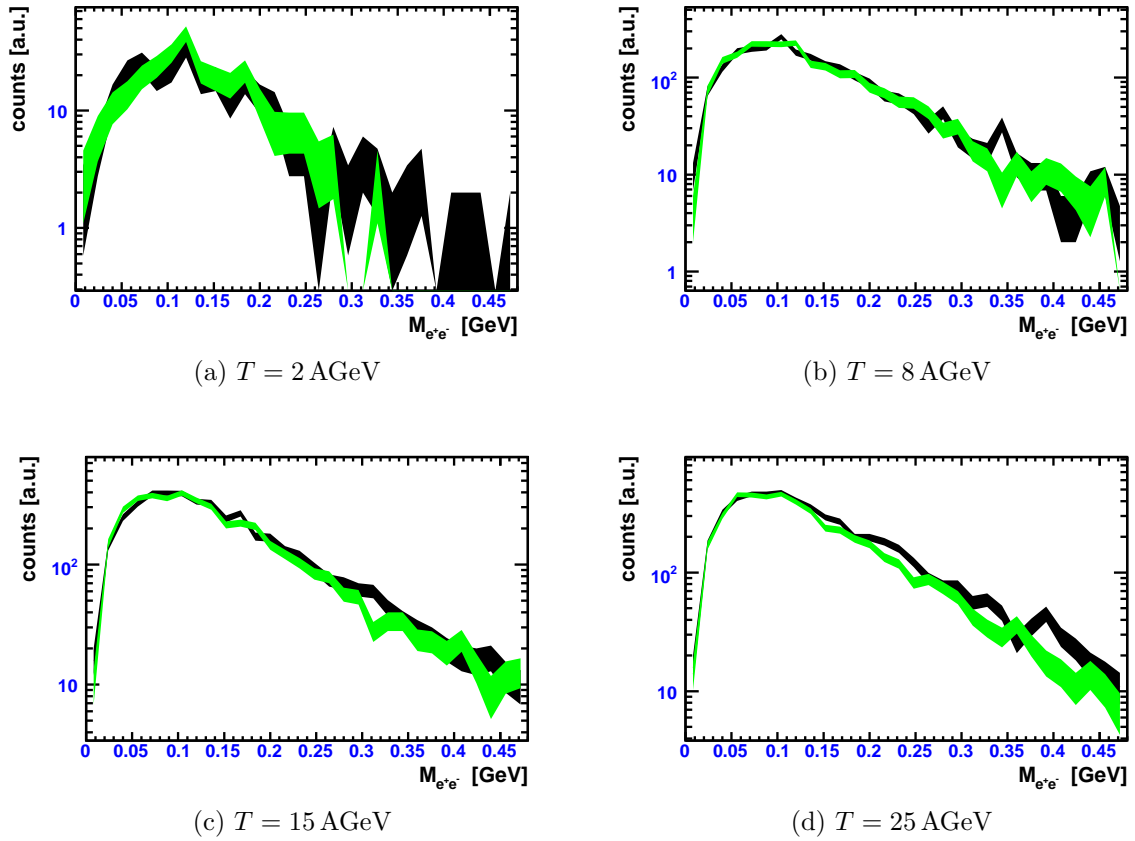


Figure 4.7: Comparison of the combinatorial background as obtained from the simulated cocktail (black) and calculated with the like-sign method (green) for invariant pair masses $m < 400$ MeV. Both the combinatorial background and the like-sign spectrum have been calculated from 1×10^6 not-enhanced UrQMD events. The width of the curves correspond to the respective errors.

We assume 20% of the beam intensity given in ref. [19] to account for the relaxed trigger conditions [54]. With the density of the graphite target $\rho_C = 2.265 \frac{\text{g}}{\text{cm}^3} = 12m_p n / A l$ the luminosity gets

$$\mathcal{L} = I l \frac{\rho_C}{12m_p}, \quad (4.7)$$

where $m_p = 1.672 \times 10^{-27}$ kg is the mass of the proton. The electron mass is not taken into account here. Integration of eq. (4.5) gives the number of interactions

$$N = I l \frac{\rho_C}{12m_p} \sigma \Delta t. \quad (4.8)$$

For the cross section σ we take the geometric cross section $\sigma = \pi b_{max}^2 = 948$ mb, where $b_{max} = r_0(A_1^{1/3} + A_2^{1/3})$ is a maximum impact parameter. In this context $A_1 = A_2 = 12$ is the atomic number of the target and beam particles. We take $r_0 = 1.2$ fm. For a target of length $l = 1$ mm, which corresponds to 1% interaction length we get a luminosity $\mathcal{L} = 1.13 \text{ s}^{-1} \text{ b}^{-1}$, yielding $N \approx 65 \times 10^6$ events after one week of beamtime.

The following cuts were applied. e^+ and e^- from the simulation were first checked if they had a minimal smeared momentum $p > 50$ MeV and if they were emitted inside the experiment's geometrical acceptance. In the subsequent pairing procedure, in a first loop all pairs were created and it was checked if they had an opening angle $\alpha > 9^\circ$ in the laboratory system. In a second loop, the final pairs were created. If in the first loop, a particle of the pair was found in any combination with opening angle $\alpha < 9^\circ$, this information was stored with the final pair and this pair is excluded from the following analysis.

For a beam energy $T = 2$ AGeV we find the signal in the $\rho - \omega$ mass region to be well above the combinatorial background (cf. fig. 4.8); with increasing beam energy the contribution from combinatorial background and conversion pairs gets more important. For a beam energy $T = 25$ AGeV the signal from $\omega \rightarrow e^+e^-$ decays is an order of magnitude stronger than the anticipated background signal. The signal-to-background ratio is shown in fig. 4.11. The signal from $\phi \rightarrow e^+e^-$ decays becomes notable for beam energies $T \geq 8$ AGeV. While most conversion pairs are produced with small invariant pair masses, with more beam energy available pairs with higher invariant pair masses will be observed. For beam energies $T > 8$ AGeV conversion pairs are a dominant source for pairs with invariant masses above the ω mass.

Combinatorial background pairs are composed mostly of electrons and positrons from photon conversion $\gamma \rightarrow e^+e^-$ and from π^0 Dalitz decays $\pi^0 \rightarrow e^+e^-\gamma$. The contribution of the different sources to the combinatorial background is shown in fig. 4.10.

In section 3.2.1 (figs. 3.7 and 3.8) we compared exclusive ω and ρ^0 production cross sections in proton-proton collisions calculated with UrQMD and experimental data. While the ω cross sections were in good agreement, we found a possible overestimation of the ρ^0 cross section in UrQMD in pp collisions of at maximum a factor 5. For the beam energies $T \geq 8$ AGeV the dominating signal source in the $\rho - \omega$ mass region is the decay $\omega \rightarrow e^+e^-$. While for a beam energy $T = 2$ AGeV the ρ^0 and ω signals are approximately of the same magnitude, for the higher energies the ω signal is more than a factor 2 higher than the ρ^0 signal, so the estimated signal-to-background ratio should not depend strongly on uncertainties of the ρ^0 cross section estimate.² Due to the applied scaling with respect to

²The invariant pair mass distribution from ρ^0 meson decays reflects the ρ^0 mass distribution in UrQMD; we find a remarkable change of its shape with increasing beam energies.

event weights the combinatorial background spectrum is fluctuating for large invariant pair masses. However, the exponential fit to the combinatorial background shows that with the assumed momentum reconstruction (cf. section 3.4) the signal from $\omega \rightarrow e^+e^-$ decays is above the background up to beam energies $T = 25$ AGeV.

Finally, we estimate that after one week of beamtime at a beam energy $T = 8$ AGeV at the ρ^0 pole mass about 20 combinatorial background pairs, about 300 pairs from the decay $\omega \rightarrow e^+e^-$ and about 60 pairs from the direct ρ^0 decay $\rho^0 \rightarrow e^+e^-$. For a beam energy of $T = 25$ AGeV the respective yields are 20 (combinatorial background), 400 ($\omega \rightarrow e^+e^-$) and 70 ($\rho^0 \rightarrow e^+e^-$). Since the combinatorial background can be estimated very accurately with the like-sign method, as demonstrated in section 4.2.4, at this state of the simulation and with the present, not explicitly optimized cuts, a measurement of good lepton pairs from the $\rho - \omega$ mass region looks feasible. Further simulations have to explore how the charged particle multiplicity displayed in tab. 4.2 leads to misidentifications of hadrons as leptons and how electron and positron track reconstruction efficiencies are affected. In our cocktail from UrQMD events the invariant pair mass spectrum from $\phi \rightarrow e^+e^-$ decays is allows lower than the ρ^0 spectrum at the respective masses. The expected dilepton yields from ϕ meson decays are on the order of 10. Due to the limited knowledge of the ρ^0 mass distribution in seems not feasible to disentangle ρ^0 and ϕ sources in the ϕ mass region and obtain the ϕ meson yield.

Comparing our invariant dilepton mass spectra with the spectra by the Rěz group in fig. 4.9, we essentially obtain the various particle multiplicities already discussed in section 3.2.3 (cf. tab. 3.2). As a consequence, in our cocktail retrieved from UrQMD events, the spectra from ω and ϕ meson decays do not stand out as in the Rěz cocktail (cf. fig. 4.9). As seen in fig. 3.10, m_t scaling in UrQMD is strongly violated for the ϕ meson; instead a much lower production cross section is predicted. The ratio of pairs from ω and Δ^+ Dalitz decays at small invariant pair masses reflects the different yields as obtained from m_t scaling and the UrQMD model, respectively.³ The flat tail of our Δ^+ invariant mass distribution is compatible with the corresponding Rěz distribution.

We also display the invariant mass spectrum obtained for the CBM experiment for AuAu collisions at $T = 25$ AGeV [51]. Since these calculations are performed for gold–gold collisions, a direct comparison is not possible. We again find the differences among the dilepton source multiplicities from UrQMD and of the CBM cocktail, namely for ϕ mesons (cf. tab. 3.3). We find differences in the ρ^0 mass distributions that are due to the different underlying transport codes. The flat ρ^0 mass distribution leads to a effective reduction of the pair yield from ρ^0 decays at its pole mass. The striking difference in the ϕ meson yields is due to the different transport codes used. As noted before, the ϕ meson yield predicted in UrQMD is lower than the yield expected from m_t scaling.

To summarize this comparison, our calculations draw a comparatively not too optimistic picture of dilepton measurements from particle decays in the $\rho - \omega$ mass region and above for kinetic beam energies of $T = 8$ AGeV to $T = 25$ AGeV. Depending on the model used (m_t scaling, different transport codes) for the estimation of the yields and phase space distributions of particles, results can differ substantially.

³We implant the decay $\Delta^+ \rightarrow pe^+e^-$, whereas in the Rěz cocktail the decay $\Delta^0 \rightarrow ne^+e^-$ is considered. However, UrQMD predicts practically the same yield for Δ^+ and Δ^0 baryons.

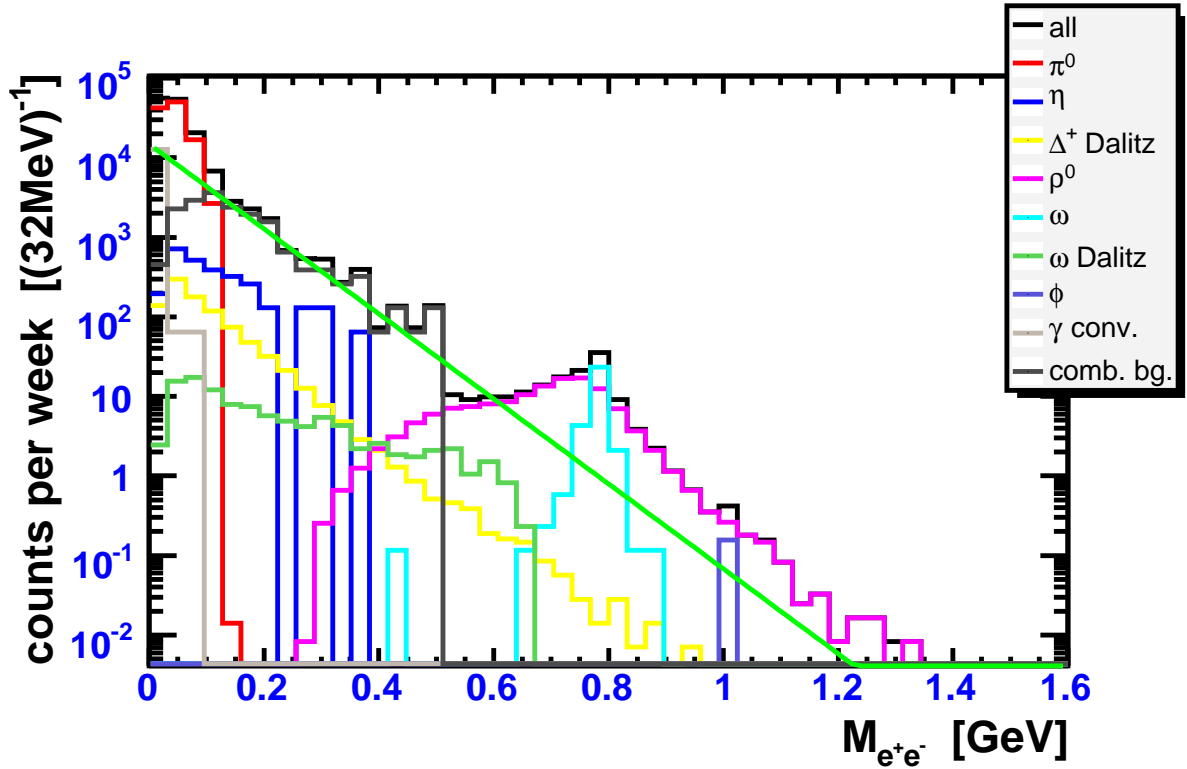
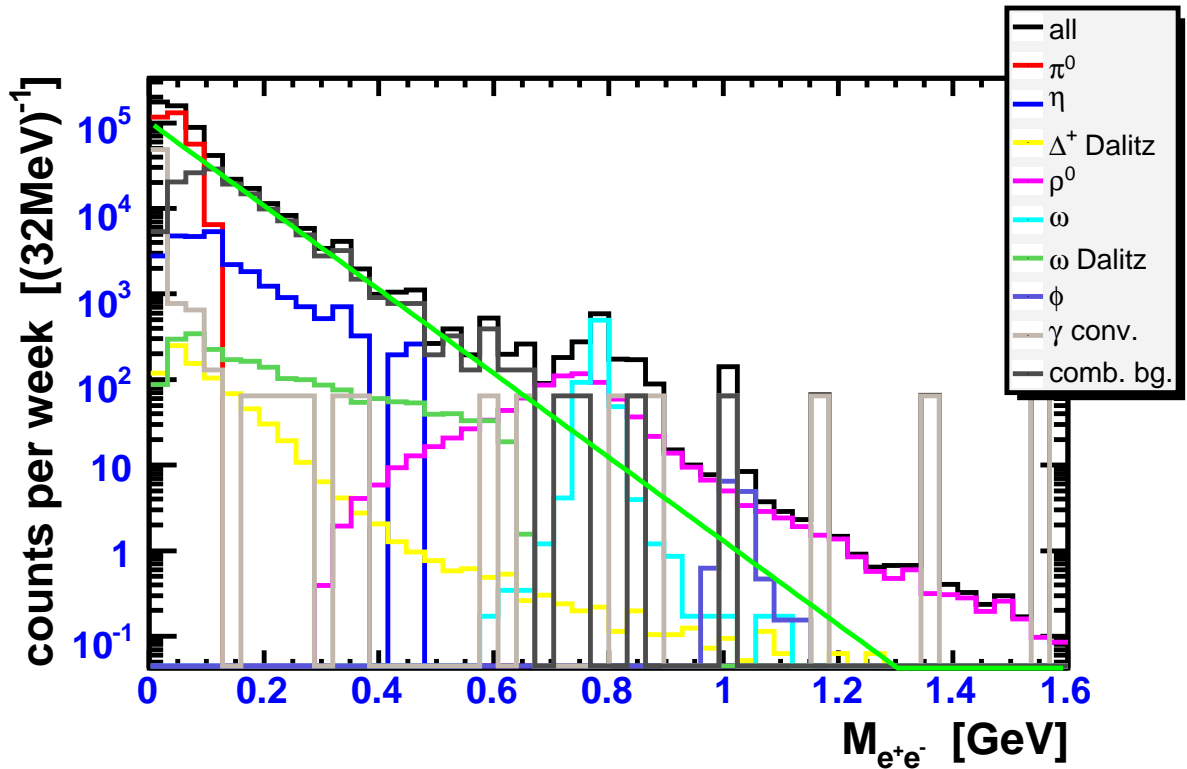
(a) $T = 2$ AGeV(b) $T = 8$ AGeV

Figure 4.8: Invariant mass spectra for central carbon–carbon collisions for different energies after one week of beamtime. Pairs are created from all e^+ and e^- emitted inside the HADES acceptance with momenta $p > 50$ MeV. Leptons from pairs with opening angles smaller than 9° are excluded. Momenta have been smeared (cf. section 3.4). An exponential fit to the combinatorial background is shown. For large invariant pair masses the simulated combinatorial background is strongly fluctuating due to the available statistics of the simulation.

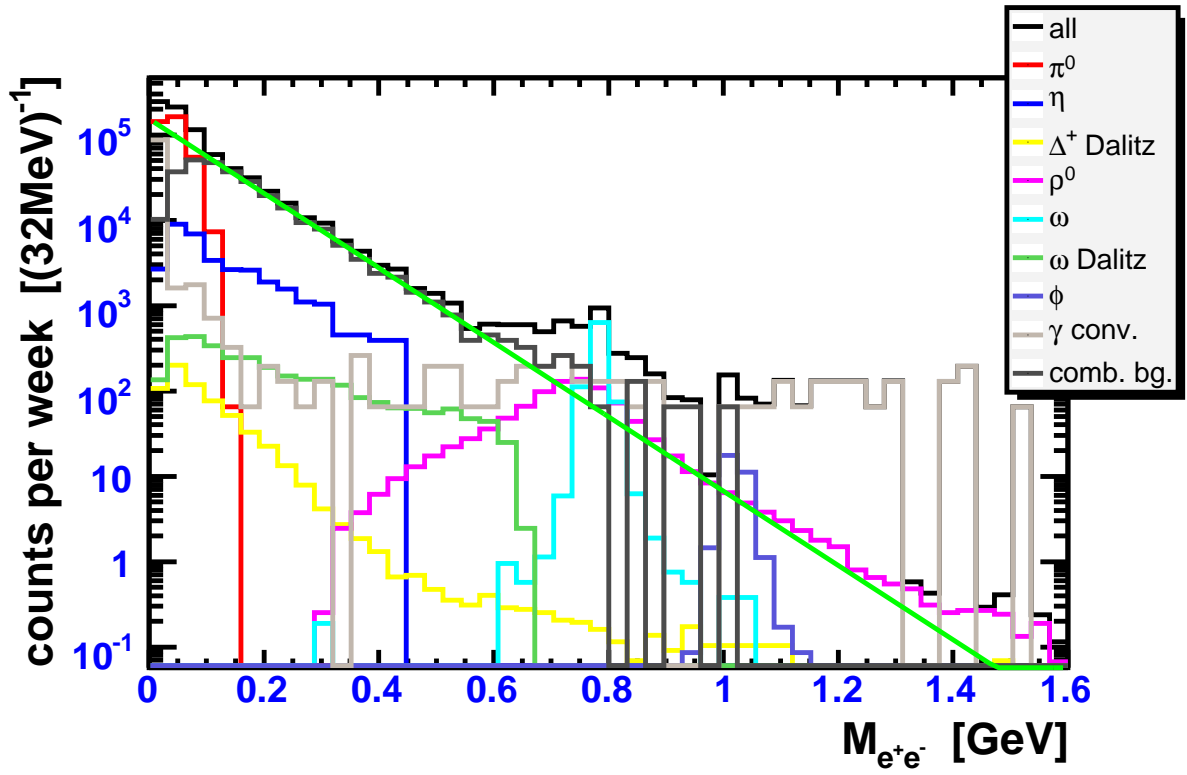
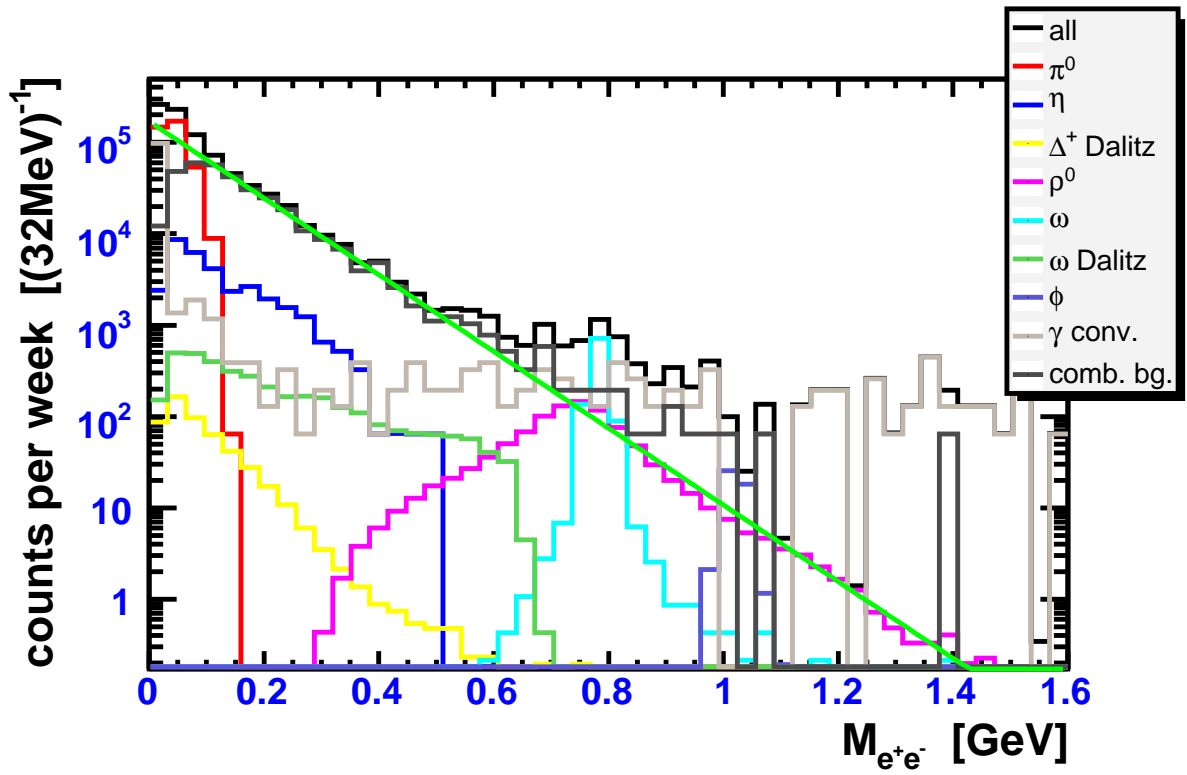
(c) $T = 15$ AGeV(d) $T = 25$ AGeV

Figure 4.8: Continued.

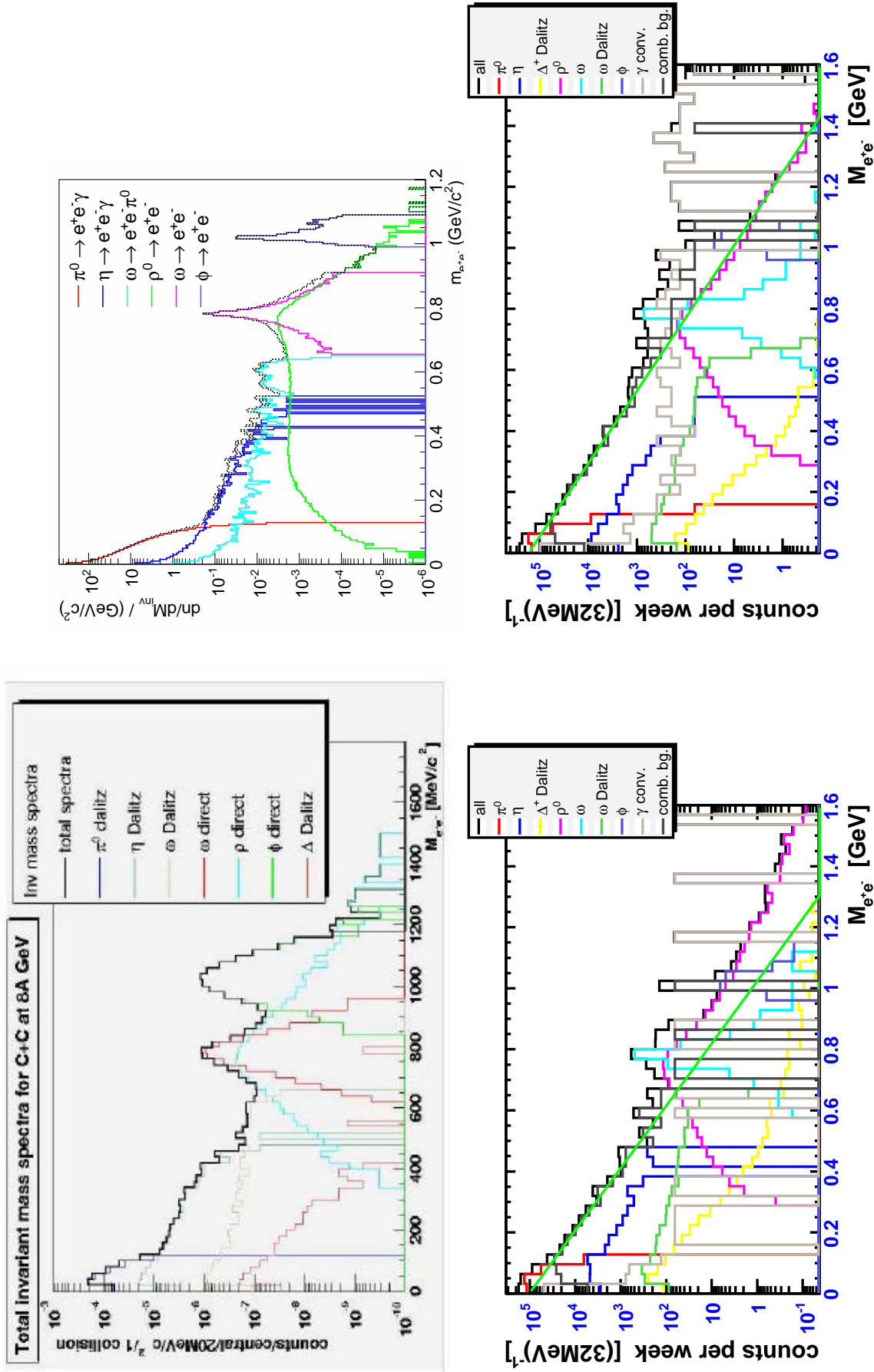


Figure 4.9: Invariant mass spectra for different cocktails. Left column: Invariant mass spectra for CC collisions at $T = 8$ AGeV by the R3z group [38] (top) and from our UrQMD cocktail (bottom), cf. fig. 4.8b. The R3z cocktail is explained in section 3.2.3; there no conversion is included. Right column: Invariant mass spectra for the CBM experiment [50] for AuAu collisions at $T = 25$ AGeV for the full phase space (top) and for our cocktail for CC collisions at the same beam energy with smearing (bottom). The composition of the CBM cocktail is explained in section 3.2.3. The figure of the UrQMD simulations also include the combinatorial background.

particle	multiplicity (all acc)							
	2 AGeV		8 AGeV		15 AGeV		25 AGeV	
p	11.991	5.739	11.752	4.157	11.587	3.775	11.538	3.637
π^+	1.995	1.230	6.828	2.713	9.520	2.916	11.927	2.898
π^-	1.996	1.223	6.827	2.716	9.500	2.891	11.940	2.900
K^-			0.074	0.016	0.217	0.033	0.416	0.043
K^+	0.010	0.006	0.328	0.099	0.615	0.137	0.917	0.164
total	15.998	8.200	25.969	9.729	31.691	9.781	37.058	9.679

Table 4.2: Charged particle multiplicities for central carbon–carbon collisions at different beam energies. For every energy we show the total yield (left) and the yield in the detector’s geometrical acceptance. Off-vertex decays are not included.

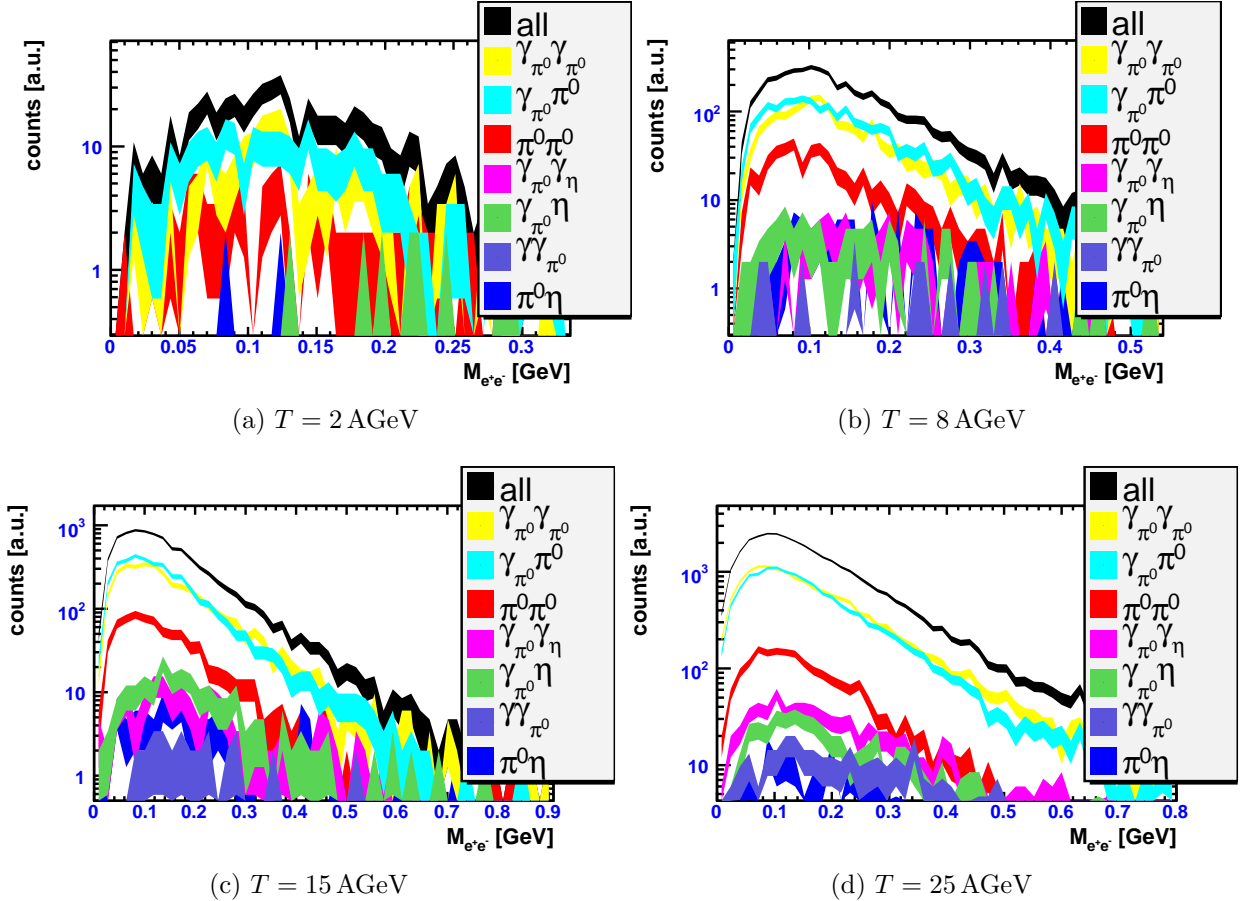


Figure 4.10: Background composition of dilepton cocktails at different energies after all cuts (cf. fig. 4.8). In the legend the mother particle of the e^\pm is shown. γ_{π^0} is from the decays $\pi^0 \rightarrow \gamma\gamma$ or $\pi^0 \rightarrow e^+e^-\gamma$, while γ_η is from $\eta \rightarrow \gamma\gamma$, $\eta \rightarrow \pi^+\pi^-\gamma$, $\eta \rightarrow e^+e^-\gamma$ or $\eta \rightarrow \mu^+\mu^-\gamma$. Other photons are from UrQMD decays, e.g. resonance decays. Fluctuations in the distributions are of statistical nature.

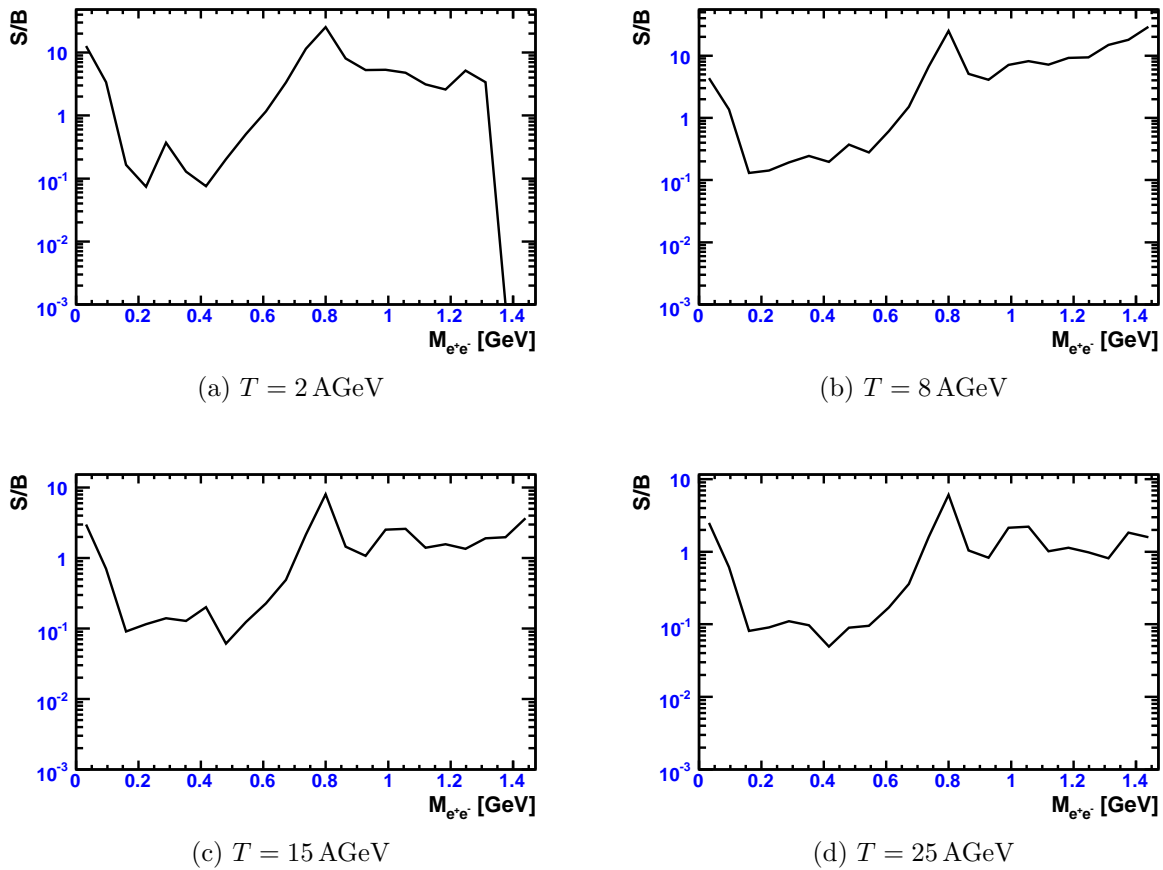


Figure 4.11: Signal-to-background ratio for the UrQMD cocktail in fig. 4.8. For calculating the ratio, the combinatorial and conversion background as obtained from the simulation were used for invariant pair masses $m < 400 \text{ MeV}$. Because of the insufficient statistics for larger masses the fit drawn in fig. 4.8 was used for $m > 400 \text{ MeV}$. The empty bin at $T = 2 \text{ AGeV}$ in fig. 4.11a is due to statistical fluctuations.

5 Summary

The goal of this thesis was to test and implement simulation software for experiments with HADES. The projected FAIR facilities at the GSI Darmstadt will provide the possibility of heavy-ion experiment at the planned two new accelerators SIS100 and SIS300. While the CBM detector is at the center of these future heavy-ion experiments, one may also investigate the potential of HADES in this new energy regime. The challenging questions are then if HADES can handle the high multiplicities and cover a reasonable part of the phase space of dielectron signals from light vector meson decays. An extension towards higher energies is desirable to fill the gap to dilepton experiments at 40 GeV and above. In this gap one expects maximum baryon densities accessible in heavy-ion experiments. In such a way in-medium modifications of light vector mesons determined by the baryon density can experimentally be probed.

The transport code UrQMDv1.3p1 has been chosen as the workhorse of the simulations and tested with the experimental database and other simulations. A generic interface for additional decays with Pluto on top of the UrQMD event has been implemented and used for the implantation of dielectron decay channels into UrQMD events. The considered dielectron sources are π^0 , η , Δ^+ , ω , ρ^0 and ϕ . A serious source of background is photon conversion $\gamma \rightarrow e^+e^-$. Important sources of photons are the decays of π^0 and η mesons, therefore these decays have been processed independently of other sources to allow for a correct event structure.

While the combinatorial background was found to be an important source of dielectrons, in our simulation distributions of like-sign pairs gave a good description of the combinatorial background. The yield of true pairs from $\omega \rightarrow e^+e^-$ decays was found to be above the combinatorial background in the respective invariant pair mass region. Furthermore, since the like-sign method allows “subtraction” of the combinatorial background from spectra and the yield of true pairs from $\rho^0 \rightarrow e^+e^-$ is larger than the fluctuations of the combinatorial background, at this state of the simulations a measurement of the pair yield from direct decays of ω and ρ^0 mesons looks feasible up to beam energies of $T = 25$ AGeV. The ϕ meson yield found was too low compared to the expected ρ^0 yield in the respective invariant mass region to allow reliable studies. The simulated dilepton spectra are for $T = 2, 8, 15$ and 25 AGeV carbon-carbon collisions. With increasing beam energy, the $\rho - \omega$ peak drops below the combinatorial background for beam energies above 8 AGeV when accounting for the geometrical detector acceptance and momentum resolution.

Our simulations represent a first step towards a full simulation. They extend previous work of the Řež group by independent and different implementations and bridge the gap towards energies beyond SIS100 to SIS300. Track separation in high-multiplicity events has not yet been examined. Further investigations have to consider the whole HADES setup (possibly with modified hardware setups); tracking of the particles through the magnetic field and the detector material should be taken into account. The performance of the current tracking algorithms in the high-multiplicity environment should be reviewed. After suitable analysis parameters have been created, tracking efficiency and particle identification capabilities can be tested.

Appendix A Analysis with HADES

For all investigations in this work we considered a detector with ideal reconstruction of particle tracks. All particles with a certain minimal momentum emitted inside the detector's geometrical acceptance were assumed to get reconstructed, while the real acceptance of the detector is made up by both geometrical acceptance and the reconstruction efficiency. The reconstruction efficiency depends on two factors: (1) the probability that a particle of certain species and momentum produces a measurable detector hit and (2) the probability that the analysis software correctly reconstructs a particle from the detector hits. While the detector response can be studied with, e.g. test beams, the efficiency of the software strongly depends on many parameters for fitting procedures and matching windows which preselect potential track candidates. To account for the specific environments of different collision system at different energies, these parameters are optimized for every run of the experiment. This way, the amount of fake tracks (tracks which correspond to no real particle) can be reduced, while maintaining a maximum reconstruction efficiency for particles.

A typical analysis of an experimental run of the HADES detector¹ involves 3 major stages:

1. For each subdetector its individual hits are combined to a set of hits stemming from the same physical particle. The MDC hits are combined to *track candidates* in several steps.
2. The subdetectors' information is matched with the *track candidates* that now propagate through the whole detector.
3. Quality cuts are applied to the *track candidates*. Decisions on the final physical quantities to assign are made leading to fully reconstructed *tracks* with all properties of a physical particle.

A.1 Reconstruction of hits in subdetectors

RICH: Hardware implemented pattern recognition algorithms reconstruct rings in the RICH and specify the center of the ring, which corresponds to the location where the track left the detector volume.

MDC: The reconstruction in the MDC composes a key part in tracking of the particle. It is again subdivided in 2 steps:

¹The HADES detector is explained in section 2.1.

1. Hits are identified in each module: For a hit to be successfully identified it should have produced a measurable signal above threshold for a number of layers in the module. The hits on the individual layer should, depending on the module's occupancy, not be located too far² from the track's other hits in the module. One may also project hits of two neighboring modules (the two before or the two after the magnet respectively) on a plane between two modules and look for a hit signal above threshold there to account for layer inefficiencies.
2. The corresponding, successfully identified hits in the two modules before and after the magnet are then separately combined to *track segments*. Ignoring the residual magnet field between the two modules the particle's path should at this point follow a straight line. Hits in the inner modules are combined, if they lie in a small opening angle cone coming from the target.

In analogy to geometrical optics, the constant momentum transfer of the toroidal magnetic field on the particle can be approximated by refraction on a plane (*kick plane*) which can be calculated from the geometry of the field.

The hit point of the inner *track segment* on the *kick plane* is then again used to combine hits lying in a small opening angle cone in the two other modules.

This way, inner and an outer *track segment* pairs are grouped to a *track candidate*.

Track segments are created from hits in one sector exclusively. Moreover, *track segments* are combined to *track candidates* from segments of the same sector. If a particle produces hits in two different sectors it will never be reconstructed to a *track candidate*.

From the hits in the 4 modules and the known kick from the magnetic field a first momentum hypothesis may be derived.

In addition, one may also fit a trajectory through the found hit points, taking into account the actual magnetic field. The errors of the hit reconstruction can be determined from both simulation and experiment [34]. This provides much better momentum resolution than the approach given above [55].

TOF and TOFino: If a TOF or TOFino rod is hit by at maximum one particle within the response time of the detector, it can deliver a measurement of the hit location. The position determination for TOFino is limited to the pad hit, but TOF also provides information where the rod was hit along its axis. Most importantly, the TOF and TOFino detectors provide a time information together with the hit. This can be the time difference between the start signal from Start detector (see below) or the time difference to the first hit (which should correspond to the fastest particle).

Pre-Shower: The evolution of the electromagnetic shower in the lead converters is connected to the particle's velocity by the Bethe-Bloch-equation [1]. The energy deposited in the shower per converter length can thus be used to determine the velocity by comparison with known distributions.

²The maximum distance is an analysis parameter, which is chosen depending on the colliding system.

Start and Veto: If used³, Start will provide a start signal for subsequent time measurements in TOF and TOFino, provided Veto was not hit. Start and Veto are built and configured for the actual run – heavy ion or elementary – with thresholds to trigger hits of the target and incident particles. If both detectors are hit in an event, it is a strong indication of events of little interaction – low centrality or even no interaction. These events can thus be rejected early from the subsequent on-line and off-line analysis chain.

A.2 Combining subdetector information

After hits in the subdetectors have been reconstructed in the first step, one has to combine the information given into tracks of physical particles.

The *track candidates* determined from MDC hits are combined with hits in the RICH, TOF, TOFino and Pre-Shower detectors. Apart from errors in the subdetector alignment about to each other [56] and reconstruction uncertainties, the width of the window required to match identified MDC *track candidates* with other detector hits is a measure for them to be caused by the same physical particle and thus belonging to the same track.

From the information of the subdetectors, hypotheses about the measured particle’s properties may be gained. The RICH provides means of lepton identification, the MDCs’ different tracking algorithms multiple possible momenta, the TOF and TOFino give a velocity measure and Pre-Shower energy and momentum assertions. The momentum reconstructed from MDC, which, with the direction of the bending of the track in the magnetic field, holds information on the measured particle’s charge, and the velocity from TOF/TOFino also make particle identification via the relativistic energy-momentum relation and the particle mass accessible.

The momentum, reconstructed from MDC, together with the bending of the track in the magnetic field provide information on the measured particle’s charge. In combination with the measured particle’s velocity, determined by the TOF/TOFino detectors, both measurements may be used for particle information via the relativistic energy-momentum relation. All this information is kept with the *track candidate*.

In the final step of the analysis, decisions are made on properties finally to be assigned to the identified *tracks*. For lepton identification this includes cuts on the number of fired RICH pads and the RICH pattern matrix [32]. To ensure high quality of the data reconstructed, one may also require a *track* to have been seen in a certain minimum number of detectors (e.g. RICH – MDC – META) or exclude tracks with hit reconstructed in low resolution detectors like TOFino. One will have to decide how to deal with *track candidates* which share the same hit with other *track candidates*. One may altogether drop these *track candidates* or pick one from the set (e.g. the one with the best momentum fit).

A.3 Reconstructing pair variables

After track reconstruction and particle identification, tracks may be combined to e^+e^- pairs. However the sample will contain a huge amount of conversion electrons, e.g. from the decay $\pi^0 \rightarrow \gamma\gamma$ and subsequent photon conversion. In simulation, it was shown [43] that

³The Start detector has not been used in all beamtimes.

the number of these conversion pairs can be substantially reduced by requiring the angle between both tracks in the laboratory system, the pair's *opening angle*, to be larger than 9° .

Regardless of the reduction of conversion electrons, in a heavy-ion collision a reconstructed event may contain more than two identified leptons leaving the possibility for multiple possible pairings. One needs to carry out all possible combinations, to create the spectrum and to subtract the amount of wrong combinations (not from the same parent particle) denoted as the *combinatorial background*. The *combinatorial background* may be extrapolated from experimental data by different methods, e.g. studying pairs from different events (*event mixing*), since two subsequent events are uncorrelated, or by the number of like-sign pairs [28] (cf. section 4.2.4).

Appendix B UrQMD: Phase space distributions of particles

Here we present distributions of transverse momentum p_t versus laboratory system rapidity y for various particles species from central carbon–carbon collisions at kinetic beam energies of $T = 2, 8, 15$ and 25 AGeV. The figures are introduced in section 3.2.4.

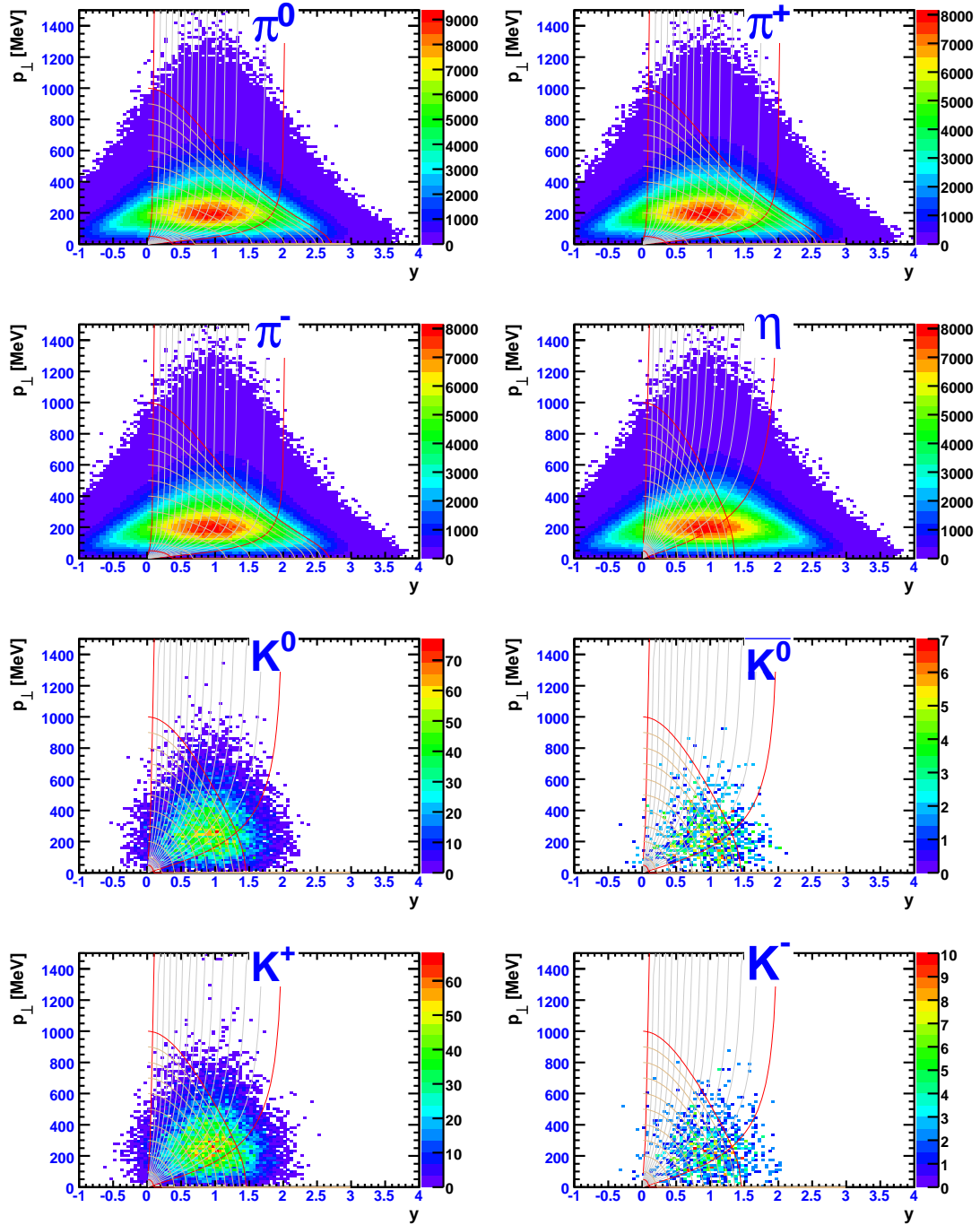


Figure B.1: Phase space distributions of various hadrons in CC collisions at $T = 2$ AGeV.

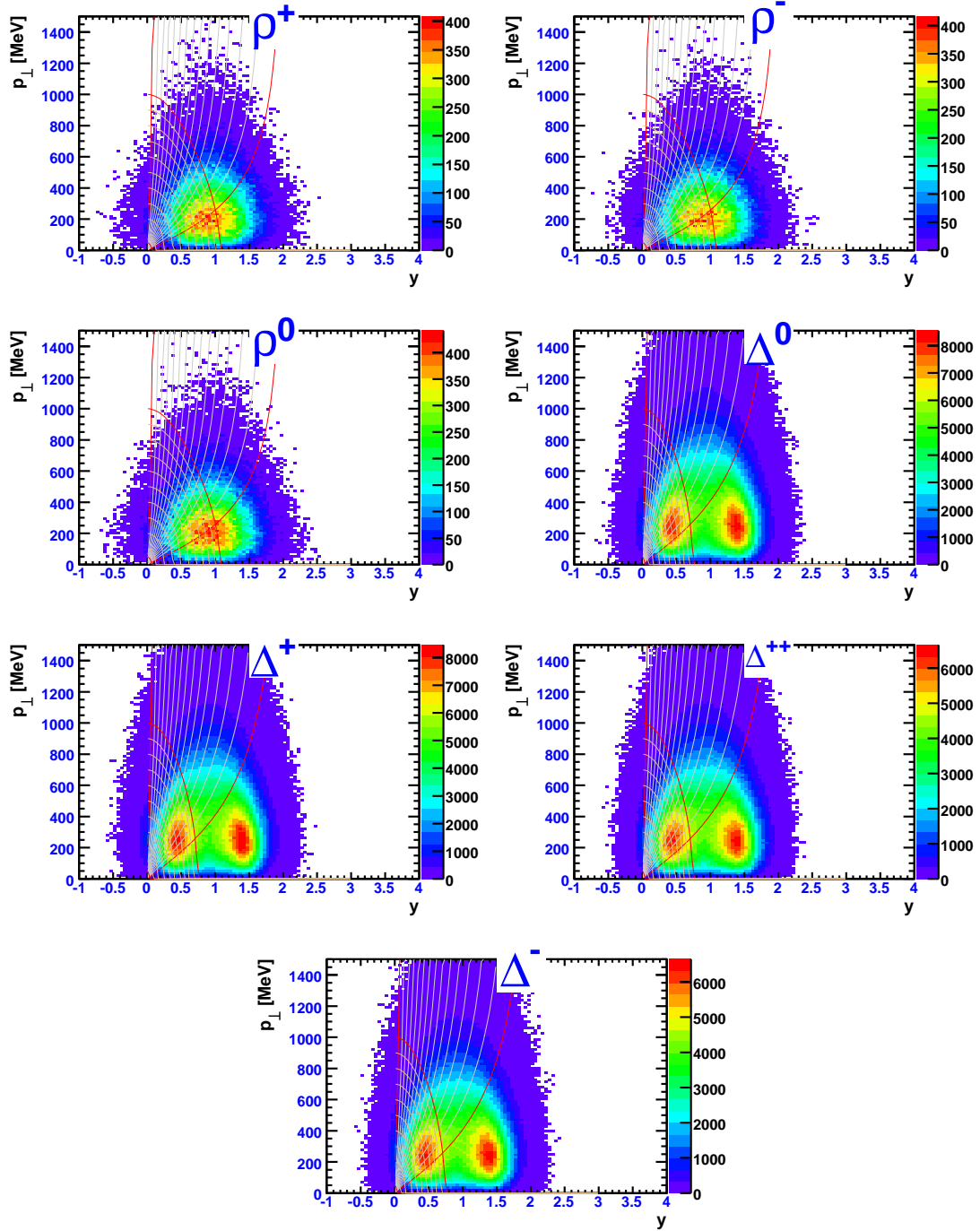


Figure B.1: Continued.

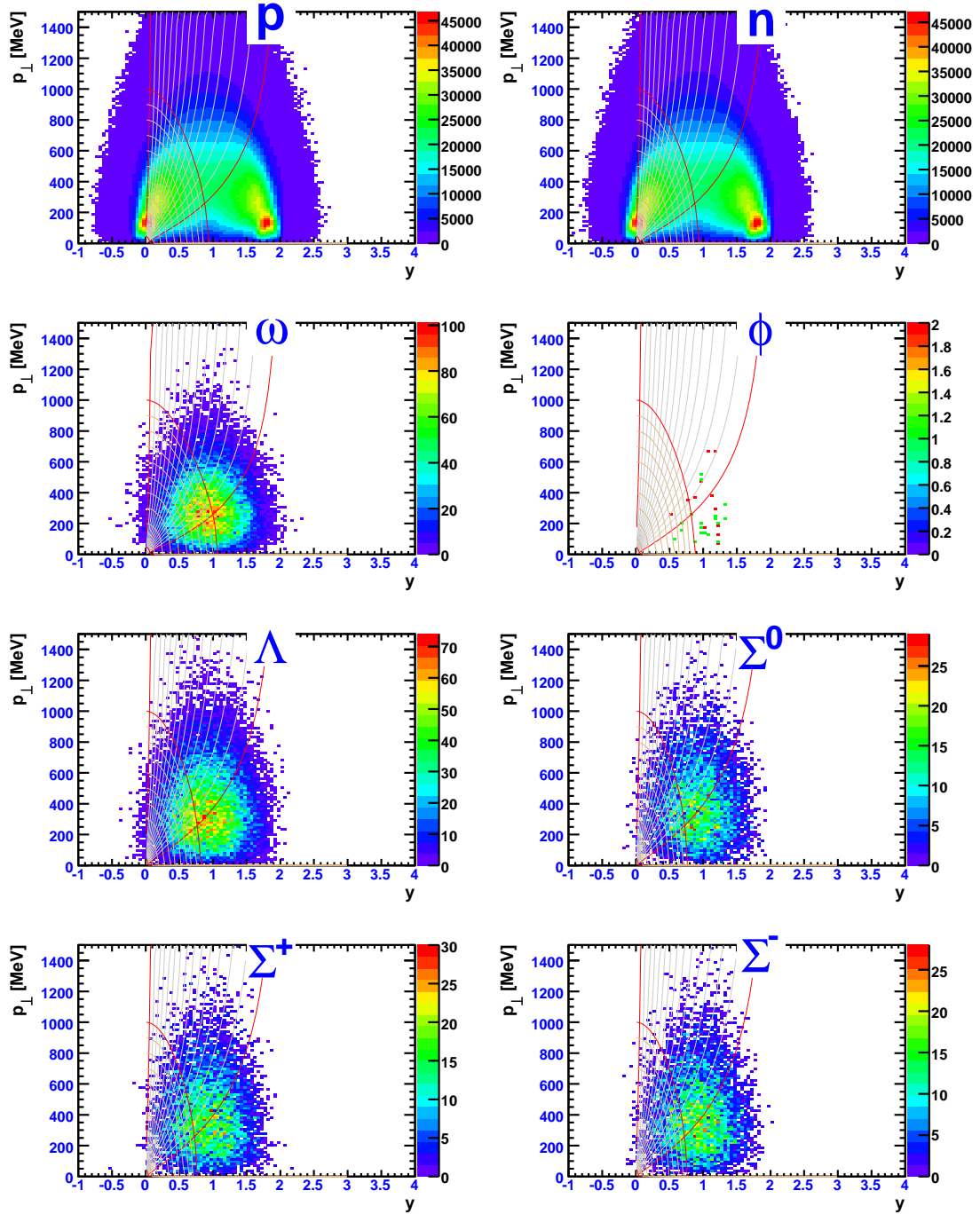


Figure B.1: Continued.

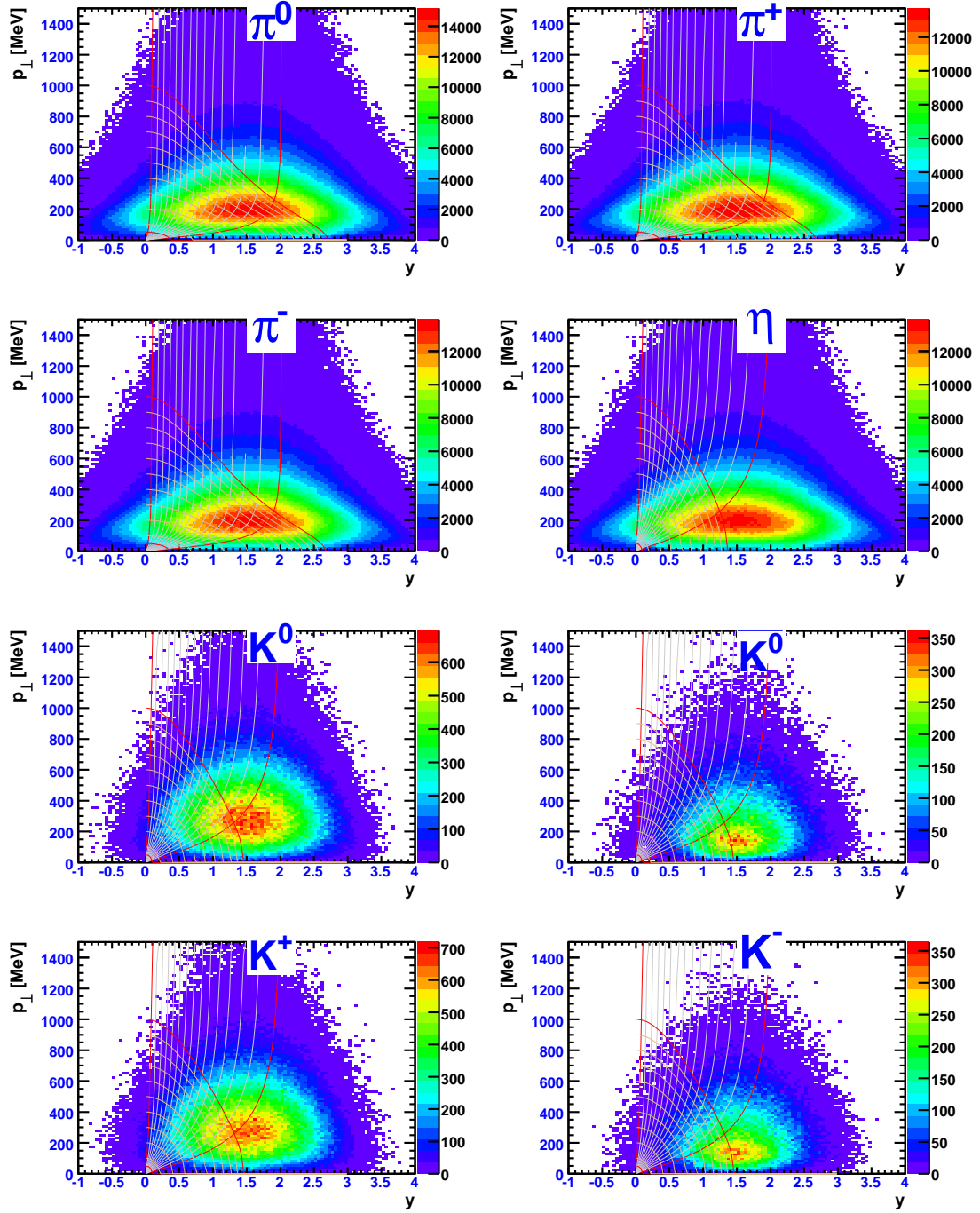


Figure B.2: Phase space distributions of various hadrons in CC collisions at $T = 8$ AGeV.

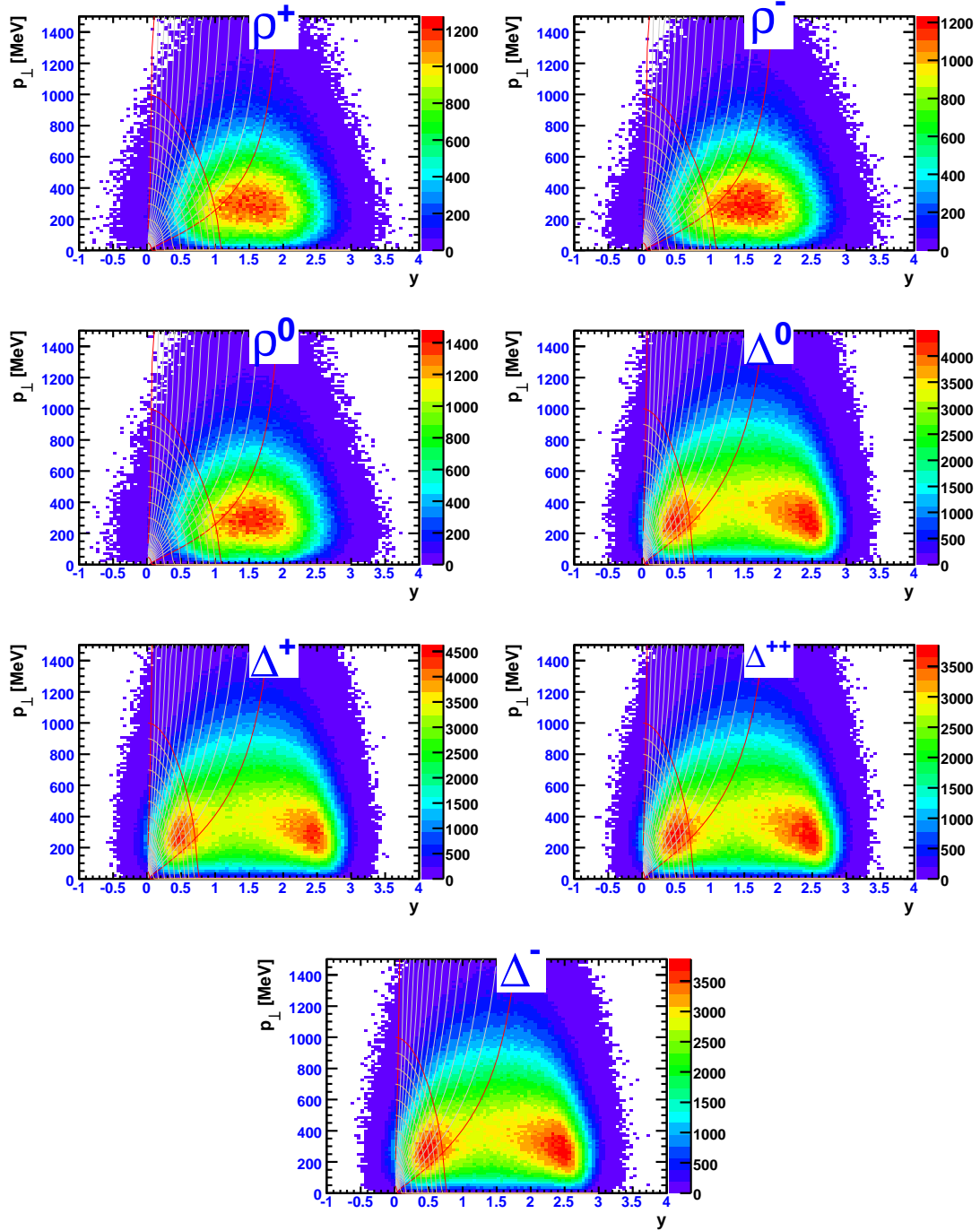


Figure B.2: Continued.

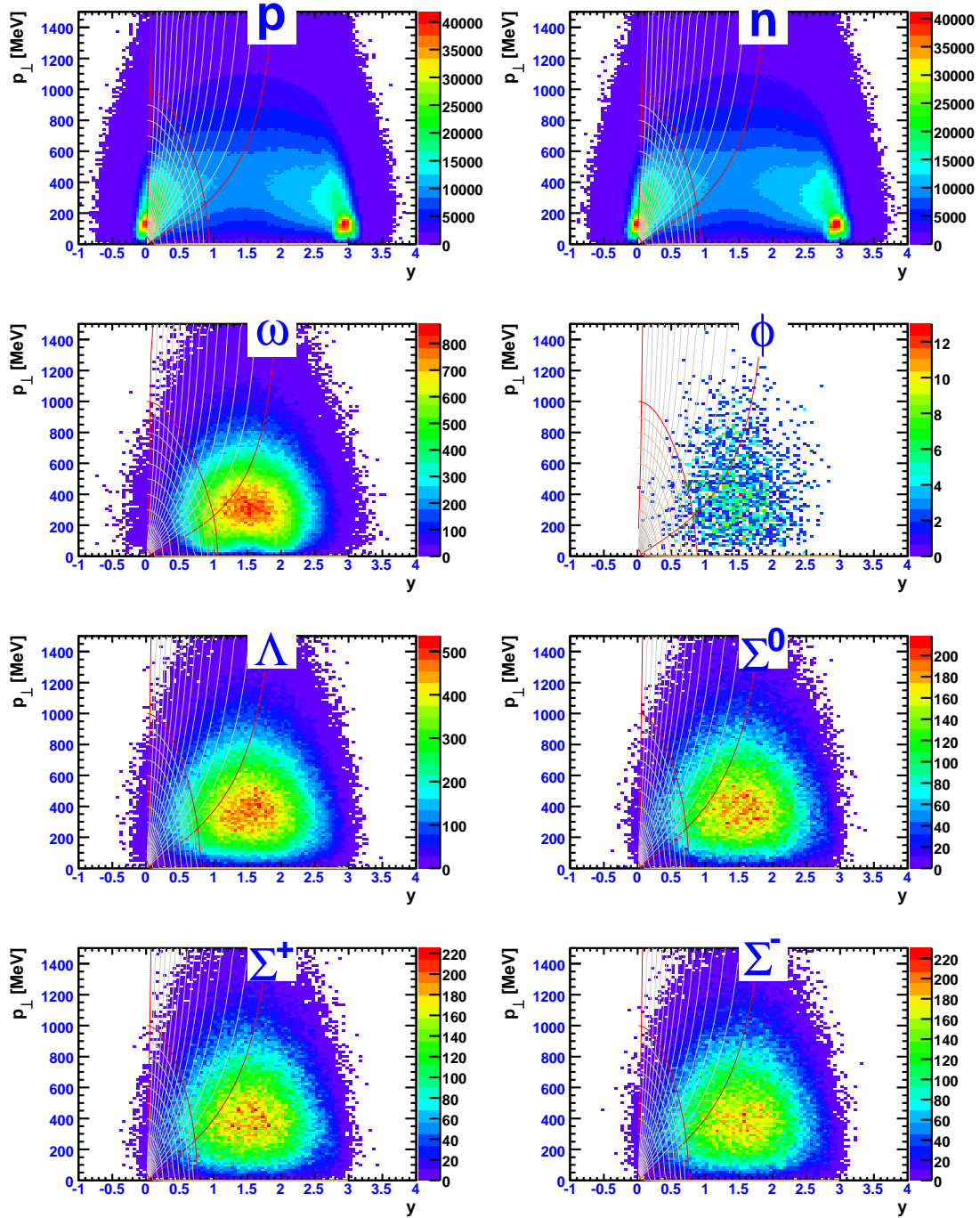


Figure B.2: Continued.

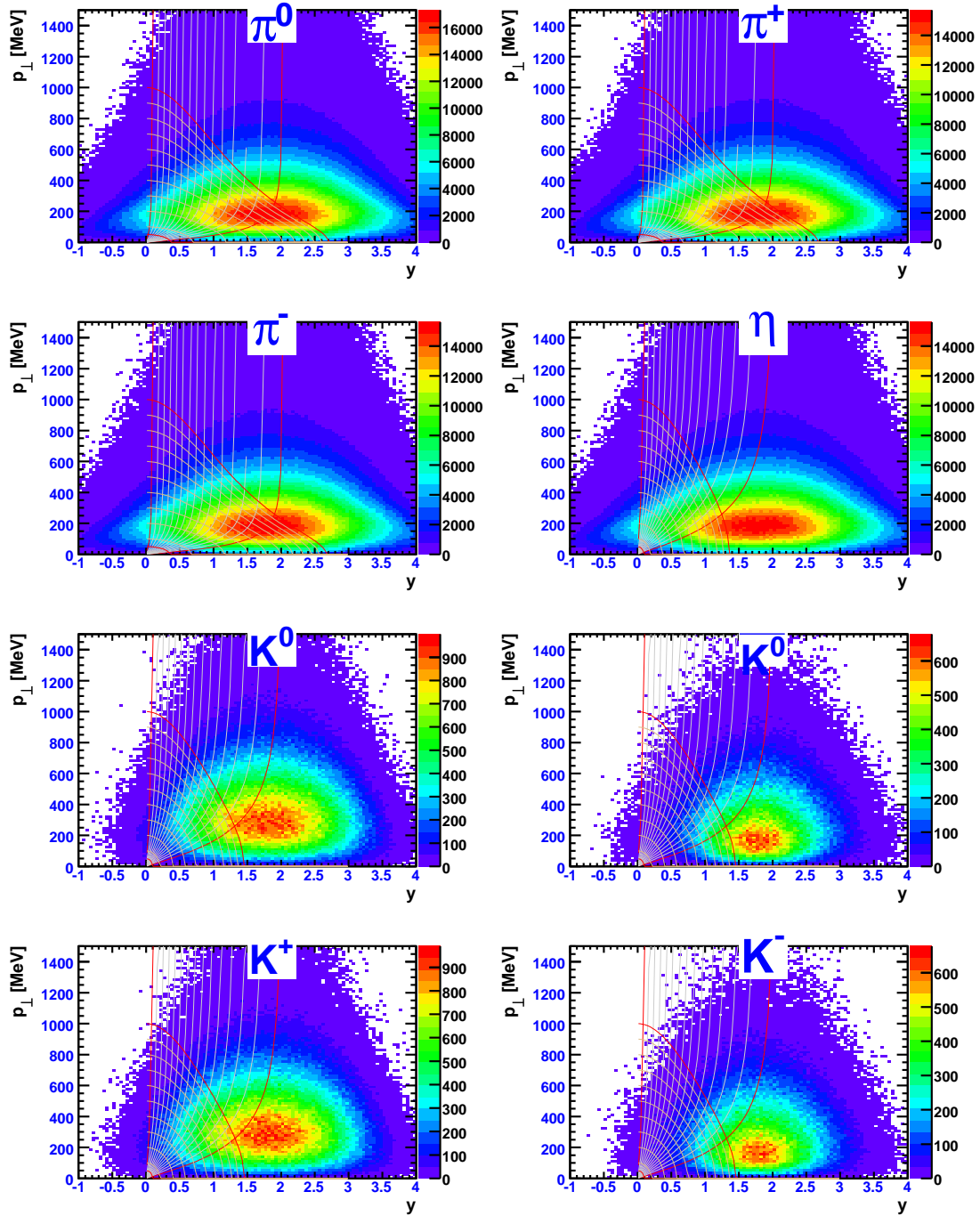


Figure B.3: Phase space distributions for various hadrons in CC collisions at $T = 15$ AGeV.

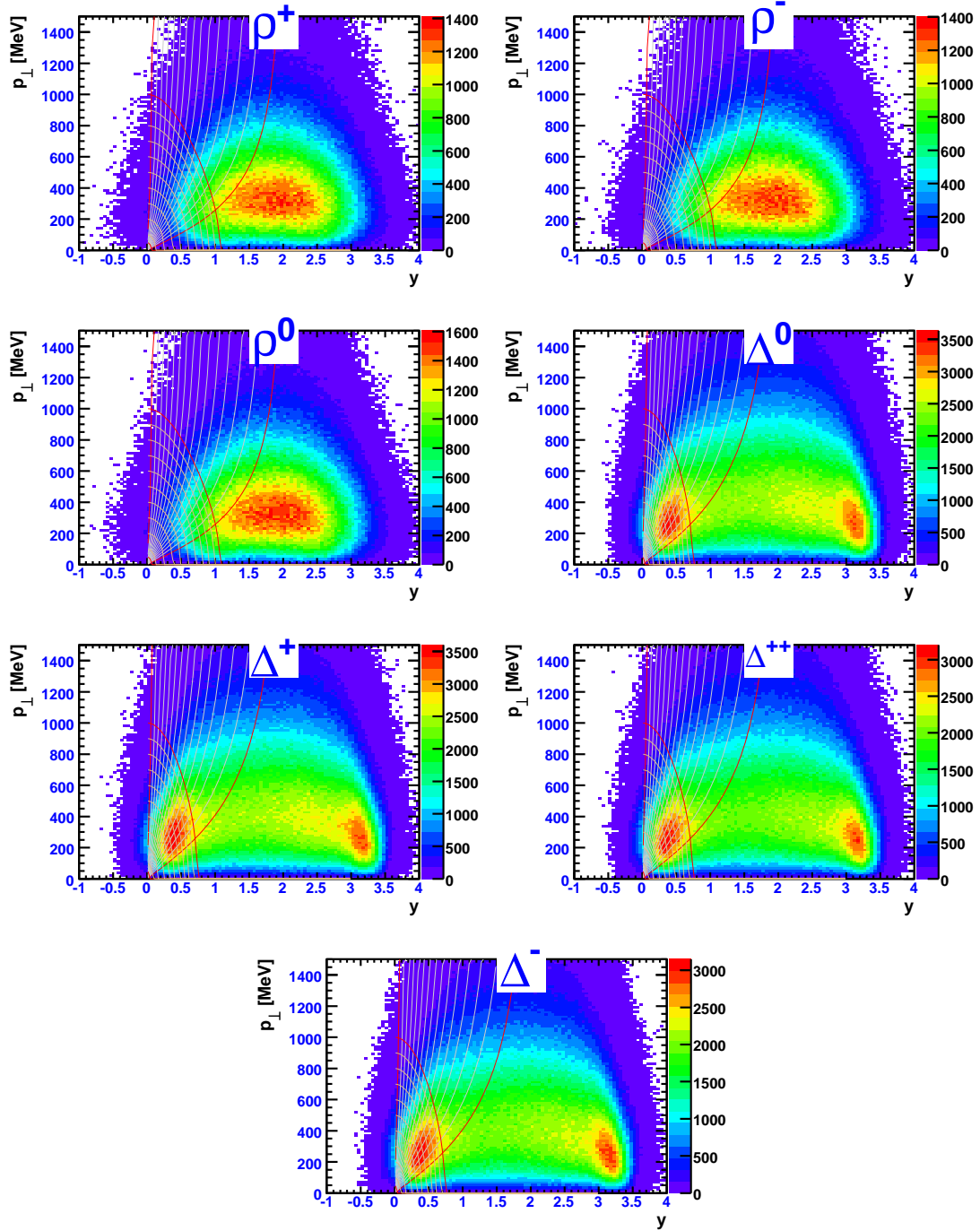


Figure B.3: Continued.

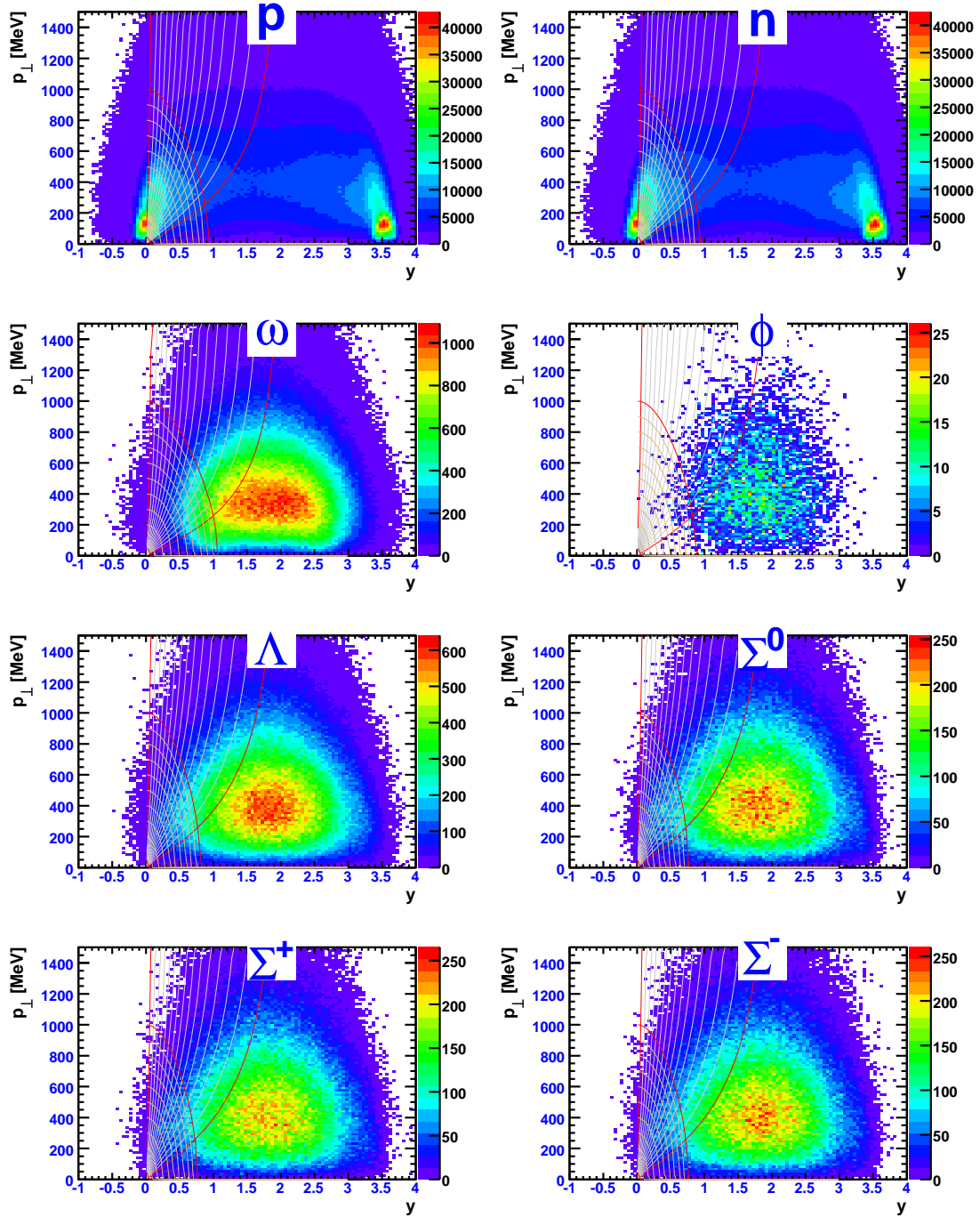


Figure B.3: Continued.

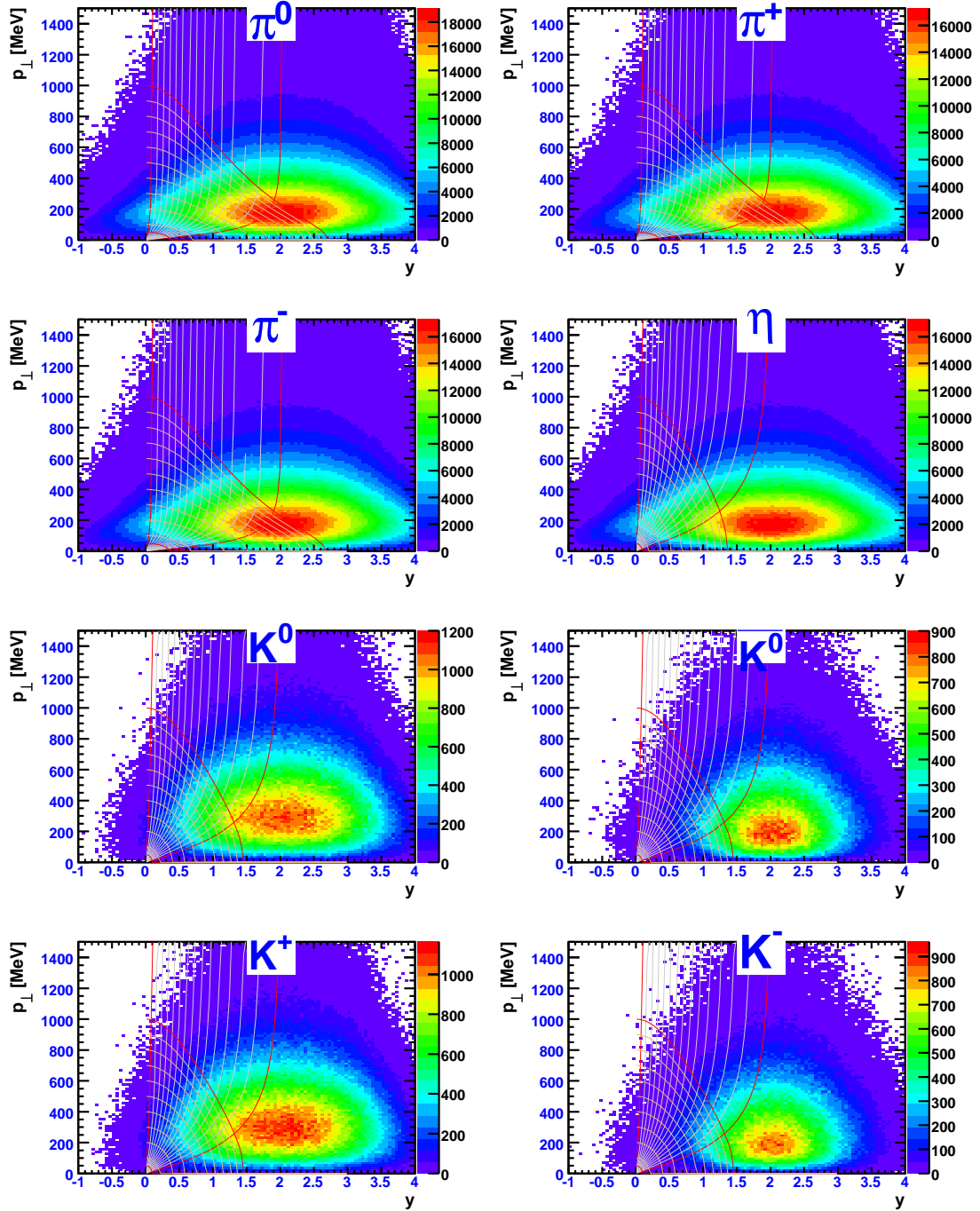


Figure B.4: Phase space distributions for various hadrons in CC collisions at $T = 25$ AGeV.

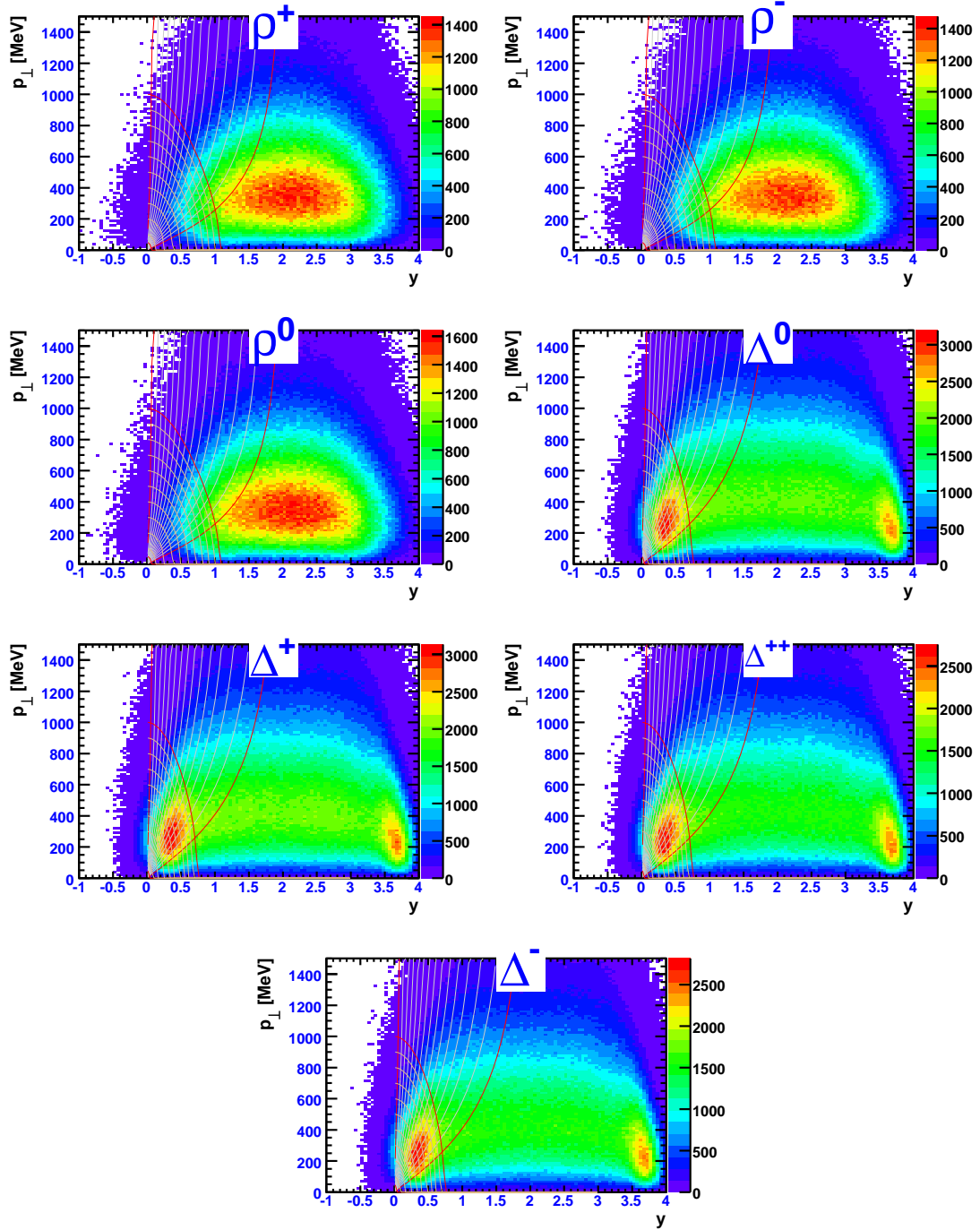


Figure B.4: Continued.

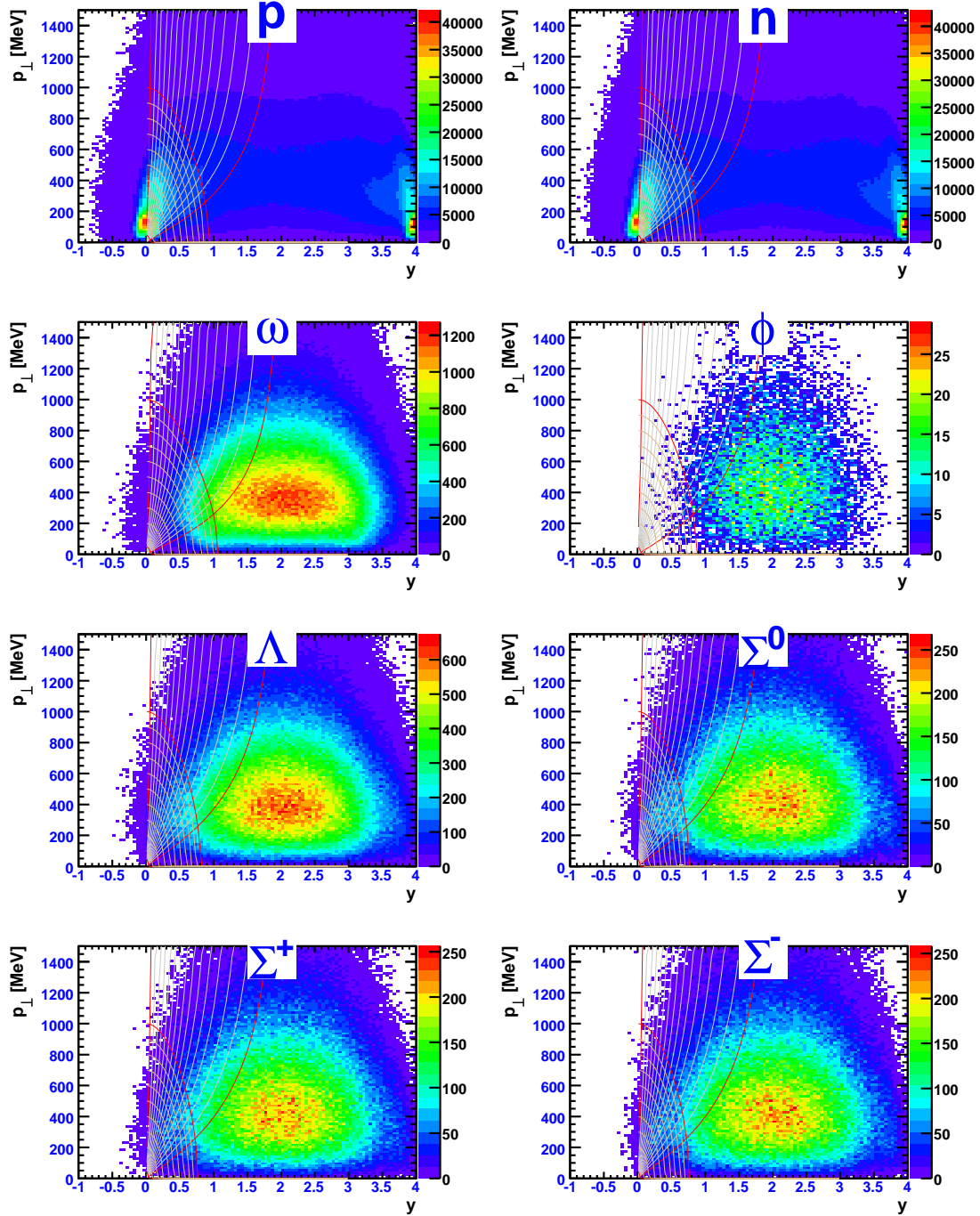


Figure B.4: Continued.

Appendix C Technical aspects of the Pluto event generator

In the following we briefly introduce some technical features of the C++ Pluto event generator library [36, 37].

Heavy-ion reactions may be modeled with fireballs implemented as the `PFireball` class. `PFireballs` can have two temperatures T_1 , T_2 with different weights. Radial expansion is modeled. Particle may be emitted with polar anisotropies; also flow parameters can be set. To model different particle species from a heavy-ion collision, one would overlay multiple `PFireball` objects with particular weights depend on the particle species' multiplicity.

In the Pluto code, particles are represented as `PParticle` objects. Particles properties as four-momenta, vertexes, particle species and parent particle specie are kept with the object.

Elementary decay channels are modeled with the `PChannel` class. Input for a channel is a possibly composite `PParticle` object, output the decay products as `PParticles`. Different channels are connected to a reaction chain. All desired reaction chains are added to the overall reaction (`PReaction`). To set up a simulation for e.g. a pp collision, one would define a composite `PParticle` object for the input channel consisting of two protons as `PParticles`. One would then add decay channels for all important final states and assign proper weights according to the channels' cross sections. Then decay channels for all particles occurring, with weights corresponding to the decays branching ratio, would be attached. If a decay leads to unstable particles, another decay channel for that particle would be appended to the channel.

Pluto provides a tool to simplify the task of connecting the many channels: the `PDecayManager` class. With the `PDecayManager` one sets up all desired decay channels for all particular particle species (e.g. $\eta \rightarrow \pi^0 2\gamma$ and $\pi^0 \rightarrow 2\gamma$). One then initializes the `PDecayManager` with a certain `PParticle` (e.g. an η). The `PDecayManager` will then set up subsequent channels (e.g. $\eta \rightarrow \pi^0 2\gamma \rightarrow 4\gamma$). Next `PDecayManager` can calculate all possible reaction, or choose one with respect to its weight. If many decay channels are used, complex reaction setups may be created.

Appendix D Proton–Proton collisions with Pluto

X	σ
$p\Delta^+$	2.298 mb
$pN^*(1440)^+$	0.6845 mb
$pp\pi^0$	2.81 mb
$pp\pi^+\pi^-\pi^0$	1.236 mb
$pN^*(1535)^+$	0.670 mb
$pp\omega$	0.119 mb
$pp\rho^0$	0.021 mb
σ_{tot}	42 mb

Table D.1: Primary channels $pp \rightarrow X$. The cross sections are determined from experimental data [46], cf. fig. D.1.

and in primary interactions, the cross section for resonance production has to be subtracted from the direct production cross section: $(\sigma_{prim}(pp \rightarrow pp\pi^0) = \sigma_{LB}(pp \rightarrow pp\pi^0) - \sigma_{sec}(pp \rightarrow p\Delta^+ \rightarrow pp\pi^0) = 2.8 \text{ mb} - 2.298 \text{ mb} \times 0.66 \approx 1.3 \text{ mb}$ for $BR(\Delta^+ \rightarrow p\pi^0) \approx 0.66$). Here, the σ_{prim} denotes the cross section for direct production, while σ_{sec} is for π^0 production via

As a first experience with Pluto and Pluto’s PDecayManager in particular, we examined dilepton production in proton–proton collisions at a beam energy $T = 3.5 \text{ GeV}$. We used the pp cocktail by Benjamin Sailer and Witek Przygoda [57] as a guideline. Since we were interested in primordial invariant pair mass spectra only (no simulation of the detector and the reconstruction), we used only channels which directly produce dileptons. η meson production is modeled via the decays $N(1535)^+ \rightarrow p\eta\pi^0$ and $N(1535)^+ \rightarrow n\eta\pi^+$

The cocktail was set-up with the primary channels listed in tab. D.1. The respective cross sections for the different channels were determined from experimental data [46], cf. fig. D.1. Since π^0 meson production is modeled both via resonance decays

particle	BR	channel
$N^*(1440)^+$	0.2	$p\pi^0$
$N^*(1535)^+$	0.3875	$p\eta$
		$p\eta\pi^0$
		$n\eta\pi^+$
		$p\eta\pi^+\pi^-$
Δ^+	0.04	$p\eta\pi^0\pi^0$
	0.66	$p\pi^0$
	4.01×10^{-5}	$p(e^+e^-)$

(a) Baryons.

particle	BR	channel
π^0	0.98798	$\gamma\gamma$
	0.01198	$\gamma(e^+e^-)$
η	0.226	$\pi^+\pi^-\pi^0$
	0.006	$\gamma(e^+e^-)$
ω	5.9×10^{-4}	$\pi^0(e^+e^-)$
	7.1×10^{-5}	e^+e^-
ρ^0	4.67×10^{-5}	e^+e^-

(b) Mesons.

Table D.2: Decay channels and branching ratios of unstable particles. Branching ratios are taken from ref. [1] or calculated from these. See the text for the procedure.

resonance decays.¹ For exclusive ρ^0 production we also cross-checked our fit to experimental data with theoretical models, see fig. D.2, and find them in good agreement.

The particle decay channels activated in the `PDecayManager` are shown in tab. D.2. The decay branching ratios for meson decays are taken directly from ref. [1]. For the baryon decays, in ref. [1] the different charged particles of an isospin multiplet are listed together (e.g. not $N(1440)^+ \rightarrow p\pi^0$, but $N(1440) \rightarrow N\pi^0$), so we had to extrapolate the values. Our rough estimates were e.g. $BR(N(1440)^+ \rightarrow p\pi^0) \approx \frac{1}{3}BR(N(1440)^+ \rightarrow p\pi)$, since there are three possible realizations of this reaction: $N(1440)^+ \rightarrow p\pi^0$, $N(1440)^+ \rightarrow n\pi^+$ and $N(1440)^0 \rightarrow n\pi^0$. Channels not listed were estimated from known values, e.g.

$$\begin{aligned} BR_{N(1535) \rightarrow p\eta\pi^0} &\approx BR_{N(1535) \rightarrow N\eta} \times BR_{N(1535) \rightarrow N\pi} \\ &\approx (30 - 50\%) \times (35 - 55\%) \approx 10 - 30\% \approx 20\%, \end{aligned}$$

which also allows to estimate, e.g.

$$\begin{aligned} BR_{N(1535) \rightarrow p\eta\pi^0\pi^0} &\approx BR_{N(1535) \rightarrow N\eta\pi^0} \times BR_{N(1535) \rightarrow N\pi} \\ &\approx (10 - 30\%) \times (35 - 55\%) \approx 5 - 11\% \\ &\text{(phase space, } \epsilon \approx 610 \text{ MeV)} \approx 4\%, \end{aligned}$$

where we reduced the decay branching ratio by 1% to roughly take suppression due to the available phase space into account.²

The decay $\pi^0 \rightarrow \gamma\gamma$ was kept in the cocktail, since π^0 s are frequently produced together with other dilepton source (e.g. $N^* \rightarrow p\eta\pi^0$). Forcing the π^0 to decay dileptonic only would lead to an overestimation of the dilepton yield.

The weight for a specific channel is determined by the possibility of the primary reaction $p = \sigma_X/\sigma_{tot}$ and the branching ratios of the decays included $b = \prod_i BR_i$. The total weight of a channel is $w = b \cdot p$. We calculated 10^5 events for every possible reaction.

In a final step we analyzed the events calculated with Pluto. Electron–positron pairs with leptons from the same mother particle were created and histograms for the invariant mass of the pair (cf. eq. (4.2)) were filled according to the weight of the particular pair. The resulting invariant pair mass spectra are shown in fig. D.3. No cuts are applied.

¹Since the production cross sections of other resonances ($N(1440)$, $N(1535)$) are comparatively small, they only contribute about 8% to the π^0 production cross section. The error in determining $\sigma(pp \rightarrow pp\pi^0)$ from experimental data [46] (cf. fig. D.1) is of the same order of magnitude.

² ϵ is the energy available to *all* particle after the reaction.

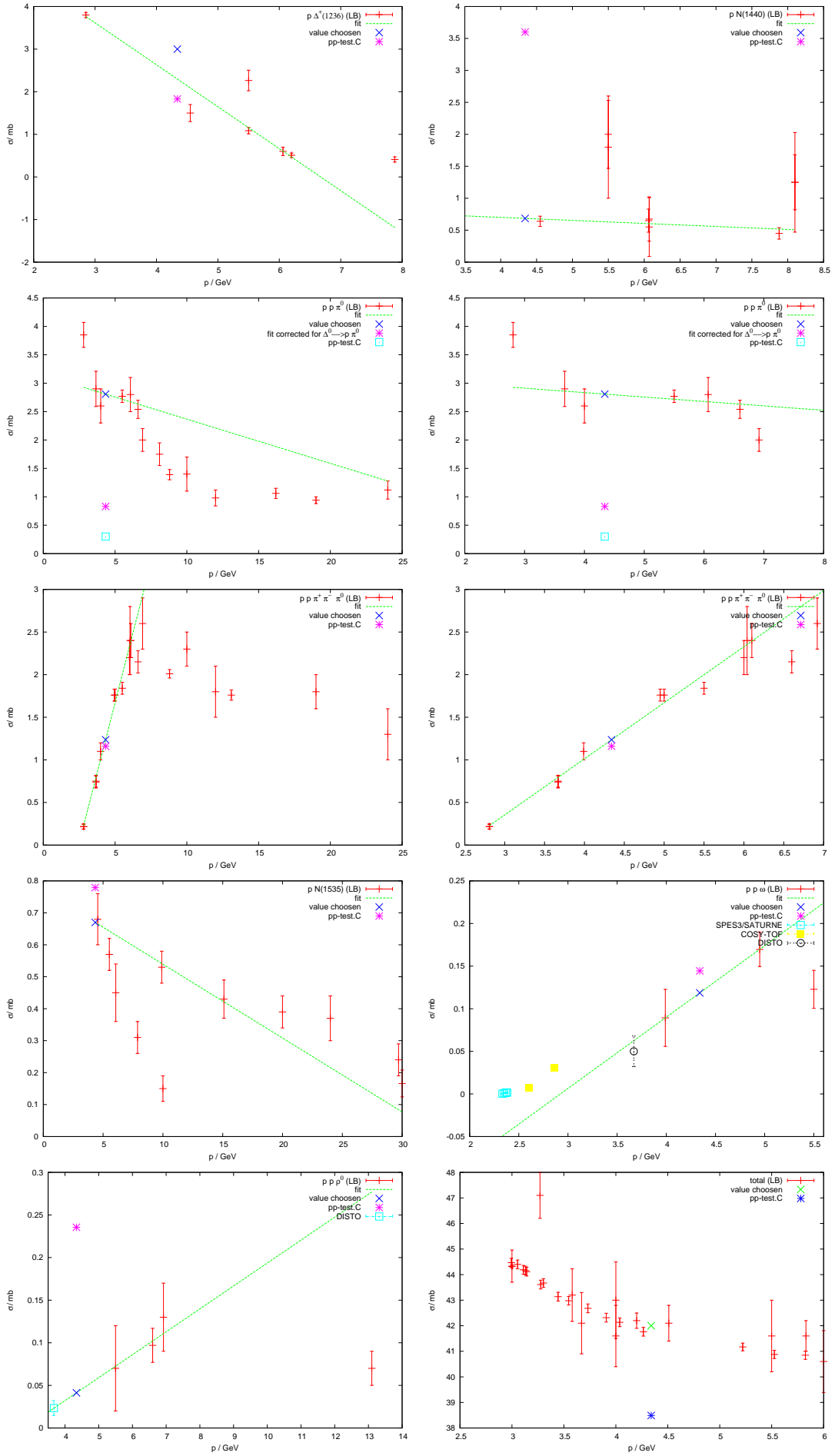


Figure D.1: Cross sections for pp collisions. The chosen value is denoted by a cross. Experimental data is from refs. [46, 58, 59, 60].

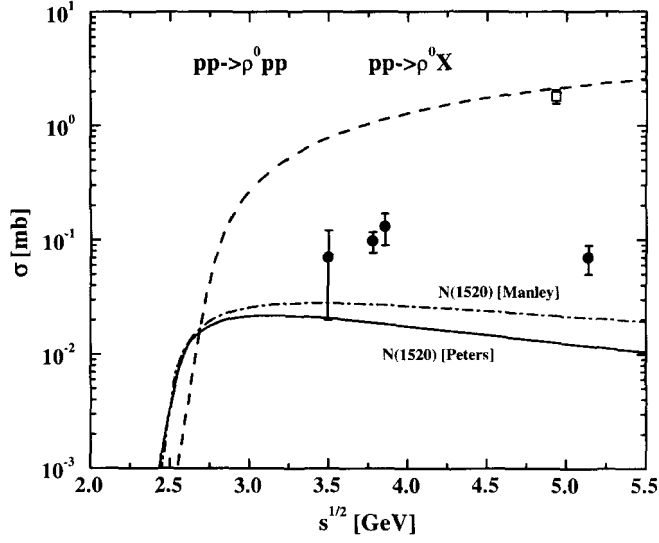


Figure D.2: ρ^0 production cross section in pp collisions [61]. For a beam energy $T = 3.5$ GeV the available energy in the center-of-mass system is $\sqrt{s} = 3.18$ GeV. The full and dot-dashed lines correspond to different model calculations of the exclusive cross section, while the dashed line is a parametrization of the inclusive cross section. The full circles and the open square are experimental data. See ref. [61] for the full references.

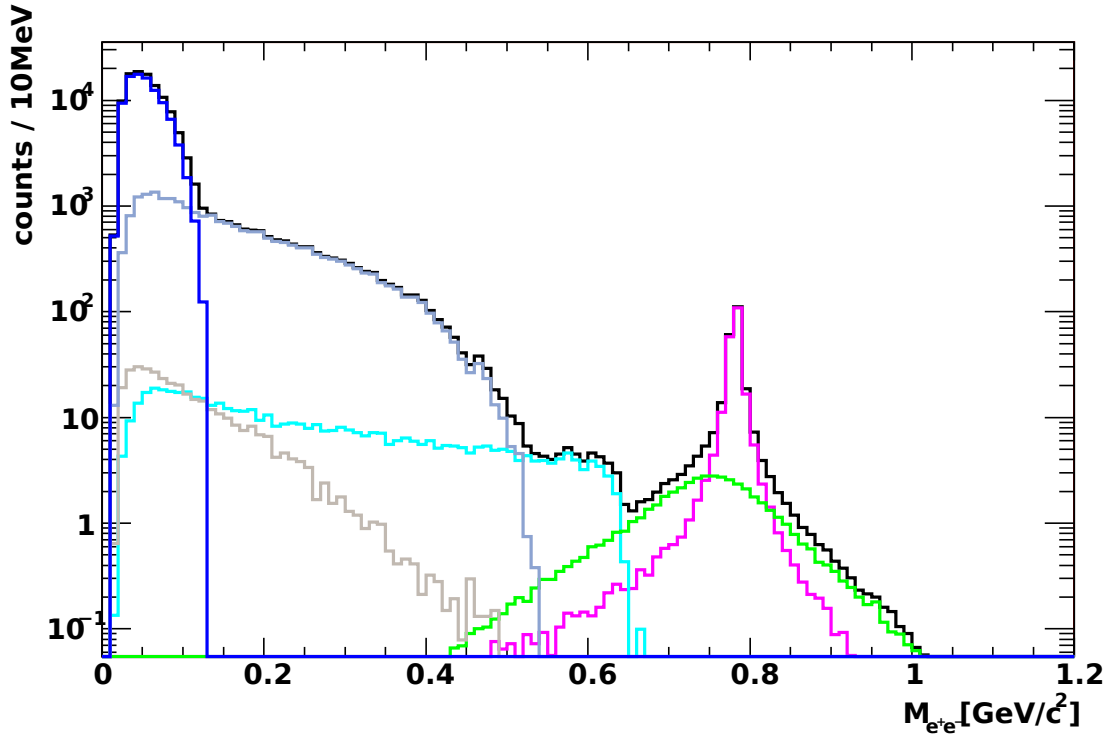


Figure D.3: Invariant dilepton mass spectrum in pp collisions at $T = 3.5$ GeV for different sources: $\pi^0 \rightarrow e^+e^-\gamma$ (dark blue), $\eta \rightarrow e^+e^-\gamma$ (blue), $\omega \rightarrow e^+e^-\gamma$ (cyan), $\Delta^+ \rightarrow pe^+e^-$ (grey), $\omega \rightarrow e^+e^-$ (purple) and $\rho^0 \rightarrow e^+e^-$ (green). The simulation is based on a Pluto cocktail.

Appendix E Abbreviations

AGS	Alternating Gradient Synchrotron
CBM	Compressed Baryonic Matter
CERN	Conseil Européen pour la Recherche Nucléaire
DLS	DiLepton Spectrometer
FAIR	FAcility for Ion Research
FZR	Forschungszentrum Rossendorf e.V.
GSI	Gesellschaft für SchwerIonenforschung
HADES	High Acceptance Di-Electron Spectrometer
HAFT	Hades Acceptance Filter for Theorists
HSD	Hadron String Dynamics
MDC	Multiwire Drift Chamber a.k.a. Mini Drift Chamber
META	Multiplicity Electron Trigger Array
QCD	Quantum-Chromo-Dynamics
RHIC	Relativistic Heavy Ion Collider
RICH	Ring Imaging CHerenkov detector
RICH-IPU	RICH Image Processing Unit
RPC	Resistive Plate Chamber
SIS	SchwerIonenSynchrotron
TAPS	Two Arms Photon Specrometer
TOF	Time-Of-Flight
UrQMD	Ultra-Relativistic Quantum Molecular Dynamics
VMD	Vector-Meson Dominance

Bibliography

- [1] S. Eidelman et al., Phys. Lett. **B592**, 1 (2004).
- [2] R. Hagedorn, Nuovo Cim. Suppl. **3**, 147 (1965).
- [3] P. Braun-Munzinger, J. Stachel, J. P. Wessels and N. Xu, Phys. Lett. **B344**, 43 (1995), [nucl-th/9410026](#).
- [4] P. Braun-Munzinger, J. Stachel, J. P. Wessels and N. Xu, Phys. Lett. **B365**, 1 (1996), [nucl-th/9508020](#).
- [5] J. Gosset et al., Phys. Rev. **C16**, 629 (1977).
- [6] J. Cleymans, H. Oeschler and K. Redlich, Phys. Rev. **C59**, 1663 (1999), [nucl-th/9809027](#).
- [7] F. Becattini and U. W. Heinz, Z. Phys. **C76**, 269 (1997), [hep-ph/9702274](#).
- [8] J. Schaffner-Bielich, D. Kharzeev, L. D. McLerran and R. Venugopalan, Nucl. Phys. **A705**, 494 (2002), [nucl-th/0108048](#).
- [9] T. Peitzmann, Eur. Phys. J. **C26**, 539 (2003), [nucl-th/0207012](#).
- [10] G. Baym and L. P. Kadanoff, Phys. Rev. **124**, 287 (1961).
- [11] L. P. Kadanoff and G. Baym, *Quantum statistical mechanics*, Advanced Book Classics (Addison–Wesley, 1994).
- [12] R. J. Porter et al. (DLS), Phys. Rev. Lett. **79**, 1229 (1997), [nucl-ex/9703001](#).
- [13] P. Senger and H. Ströbele, J. Phys. **G25**, R59 (1999), [nucl-ex/9810007](#).
- [14] R. Donangelo and R. S. Wedemann, Nucl. Phys. **A541**, 641 (1992).
- [15] J. Stachel and P. Braun-Munzinger, Phys. Lett. **B216**, 1 (1989).
- [16] E. L. Bratkovskaya et al., Nucl. Phys. **A675**, 661 (2000), [nucl-th/0001008](#).
- [17] W. F. Henning et al., eds., *Conceptual Design Report* (FAIR project, GSI Darmstadt, 2004).
- [18] W. F. Henning et al., eds., *The Facility*, p. 485f, in [17] (2004), DOC-2004-Mar-201-1.
- [19] W. F. Henning et al., eds., *Nucleus-Nucleus Collisions – Compressed Baryonic Matter*, pp. 265–344, in [17] (2004), DOC-2004-Mar-200-4.

-
- [20] R. Rapp, J. Phys. **G31**, S217 (2005), [nucl-th/0409054](#).
- [21] R. Rapp and J. Wambach, Adv. Nucl. Phys. **25**, 1 (2000), [hep-ph/9909229](#).
- [22] R. Thomas, S. Zschocke, and B. Kämpfer, Phys. Rev. Lett. **95**, 232301 (2005), [hep-ph/0510156](#).
- [23] T. Hatsuda and T. Kunihiro, Phys. Lett. **B198**, 126 (1987).
- [24] G. E. Brown and M. Rho, Phys. Rev. Lett. **66**, 2720 (1991).
- [25] S. Zschocke, O. P. Pavlenko, and B. Kämpfer, Eur. Phys. J. **A15**, 529 (2002), [nucl-th/0205057](#).
- [26] B. Kämpfer, private communication (2006).
- [27] J. Randrup and J. Cleymans (2006), [hep-ph/0607065](#).
- [28] H. Schön, Ph.D. thesis, GSI Darmstadt (1995), in German.
- [29] HADES collaboration, Experiment Proposal, GSI, <http://www.gsi.de/documents/DOC-2003-Jun-15-1.pdf> (2001).
- [30] HADES collaboration, Experiment Proposal, GSI, <http://www.gsi.de/documents/DOC-2003-Jul-1-1.pdf> (2003).
- [31] HADES collaboration, Experiment Proposal, GSI, <http://www.gsi.de/documents/DOC-2004-Sep-52-1.pdf> (2004).
- [32] L. Fabbietti, Ph.D. thesis, TU München (2003).
- [33] C. Müntz (HADES), Nucl. Phys. Proc. Suppl. **78**, 139 (1999).
- [34] J. Markert, Ph.D. thesis, Johann Wolfgang Goethe-Universität/Frankfurt am Main (2005), in German.
- [35] S. Spataro, Ph.D. thesis, Università Degli Studi Di Catania (2006).
- [36] M. A. Kargalis, *Pluto⁺⁺: A Monte Carlo simulation tool for hadronic physics*, GSI report 2000-03 (2000).
- [37] R. Holzmann, *The Pluto Event Generator*, Talk given at the CBM software Week (2004), GSI, unpublished.
- [38] A. Kugler, *Measuring dileptons with HADES at 8 AGeV*, Talk given at the CBM meeting, 11.02.2004, GSI Darmstadt (2004), cf. [49].
- [39] W. Cassing and E. L. Bratkovskaya, Phys. Rept. **308**, 65 (1999).
- [40] S. A. Bass et al., Prog. Part. Nucl. Phys. **41**, 225 (1998), [nucl-th/9803035](#).
- [41] M. Bleicher et al., J. Phys. **G25**, 1859 (1999), [hep-ph/9909407](#).

-
- [42] S. Soff, Ph.D. thesis, Johann Wolfgang Goethe-Universität Frankfurt (2000), in German.
- [43] P. Salabura, Tech. Rep., <http://hades-wiki.gsi.de/pub/SimAna/FastDielectronCocktailGeneration/plutosim.pdf> (2005), HADES experiment internal document.
- [44] R. Brun, F. Bruyant, M. Maire, A. C. McPherson and P. Zancarini, *Geant3*, CERN-DD/EE/84-1.
- [45] A. Galoyan, J. Ritman, and V. Uzhinsky (2006), `nucl-th/0605039`.
- [46] H. Schopper, ed., *Zahlenwerte und Funktionen aus Naturwissenschaft und Technik/Landolt-Börnstein*, vol. I/12b (Springer, Berlin, 1988).
- [47] V. Metag, Nucl. Phys. **A630**, 1c (1998).
- [48] R. Auerbeck et al. (TAPS), Z. Phys. **A359**, 65 (1997).
- [49] A. Kugler et al., *HADES at SIS100*, talk given at the XLIV. International Winter Meeting on Nuclear Physics, Bormio (2006).
- [50] T. Galatyuk and J. Stroth, *Strategies for electron pair reconstruction in CBM*, CBM-PHYS-note-2006-001, CBM experiment internal document, GSI Darmstadt (2006).
- [51] CBM collaboration, Tech. Rep., GSI (2005).
- [52] R. Holzmann, *The Hades Acceptance Filter for Theorists (HAFT)*, <http://hades-wiki.gsi.de/cgi-bin/view/SimAna/HadesAcceptanceFilter> (2006), HADES experiment internal document.
- [53] R. Schicker et al., Nucl. Instrum. Meth. **A380**, 586 (1996), `nucl-ex/9605004`.
- [54] R. Holzmann, private communication (2006).
- [55] I. König, Tech. Rep., GSI Darmstadt, http://hades-wiki.gsi.de/pub/SimAna/RungeKuttaTrackingStatus/report_runge_kutta_17032006.pdf (2006), HADES experiment internal document.
- [56] A. Schmah, Tech. Rep., GSI Darmstadt, <http://www.gsi.de/documents/DOC-2006-Mar-137-1.pdf> (2006), HADES experiment internal document.
- [57] W. Przygoda and B. Sailer, Tech. Rep., http://www-hades.gsi.de/~hadesdst/sep03_sim/gen1/simdstgen1.html, `pp_test.C` (2004), HADES experiment internal document.
- [58] S. Abdel-Samad (COSY-TOF), Phys. Lett. B **522**, 16 (2001).
- [59] F. Balestra et al. (DISTO), Phys. Rev. **C63**, 024004 (2001), `nucl-ex/0011009`.
- [60] F. Balestra et al. (DISTO), Phys. Rev. Lett. **89**, 092001 (2002), `hep-ex/0209004`.
- [61] E. L. Bratkovskaya, W. Cassing, M. Effenberger, and U. Mosel, Nucl. Phys. **A653**, 301 (1999), `nucl-th/9903009`.

Acknowledgment

I would like to thank all the people who made this work possible with their interest and support.

First of all I would like to thank Prof. Dr. E. Grosse for giving me the opportunity to work on the subject. Fruitful discussions with Prof. Dr. B. Kämpfer, especially on the theoretical aspects, gave an indispensable insight, without which this thesis would not have been possible. My colleagues at the Rossendorf institute I would like to thank for their willing attendance in upcoming questions. I would like to thank in particular Dr. F. Dohrmann for sharing his office with me, his being all ears to questions of any kind and proof-reading the manuscript, Dr. R. Kotte for his many ideas on experimental topics, A. Sadovsky and K. Kanaki for their help on analysis questions and their personal assurance as well as Dr. J. Wüstenfeld for helping me out of the pitfalls compilers offer and, not to forget, our administrator J. Steiner for not batting an eyelid on most crotchety requests.

I also would like to thank the many people of the HADES collaboration for their explaining words on the aspects of the experiment, especially Dr. S. Spataro who gave me a first insight into the analysis software and Dr. J. Markert for introducing me to the delicate business of tracking. Dr. A. Kugler and Dr. P. Tlustý of the Řež group were always ready to answer any of my questions on the subject. I would also like to thank Dr. R. Holzmann for sharing his rich knowledge on many aspects of both simulation and analysis techniques.

This work also did thrive and prosper due to the hospitality of J. Braun and L. Bittrich of TU Dresden in days of prolonged breakfast, but it would have been outright impossible without my family's support over all the years.